

AD-A127 529

AN ANALYSIS OF CONICAL INDENTATION OF AN
ELASTIC/PERFECTLY PLASTIC HALF-S. (U) PENNSYLVANIA
STATE UNIV UNIVERSITY PARK APPLIED RESEARCH LAB.

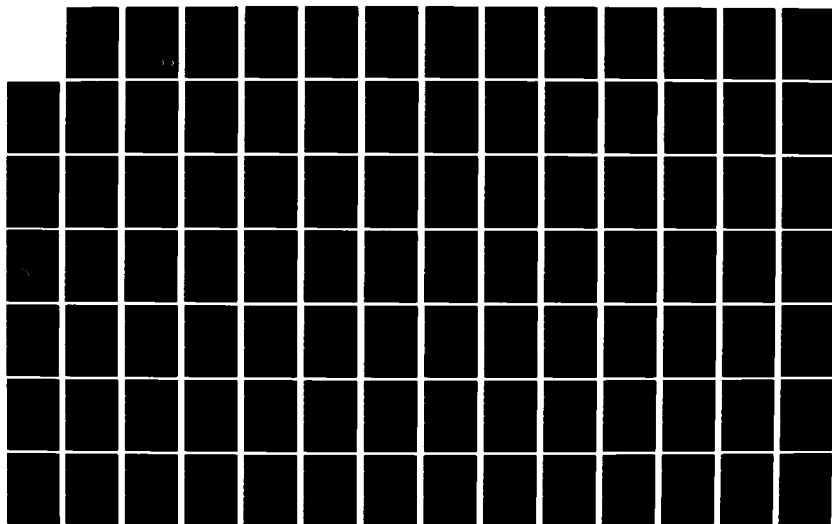
1/2

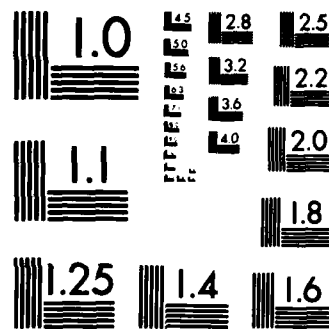
UNCLASSIFIED

T KATO 26 OCT 82 ARL/PSU/TM-82-238

F/G 28/11

NL





MICROCOPY RESOLUTION TEST CHART
NATIONAL BUREAU OF STANDARDS-1963-A

6

AD A127529

AN ANALYSIS OF CONICAL INDENTATION OF AN ELASTIC/
PERFECTLY PLASTIC HALF-SPACE BY NONLINEAR FINITE
ELEMENT TECHNIQUES

Takehiko Kato

Technical Memorandum
File No. TM 82-230
October 26, 1982
Contract No. N00024-79-C-6043

Copy No. 5

The Pennsylvania State University
Intercollege Research Programs and Facilities
APPLIED RESEARCH LABORATORY
Post Office Box 30
State College, Pa. 16801

APPROVED FOR PUBLIC RELEASE
DISTRIBUTION UNLIMITED

NAVY DEPARTMENT

NAVAL SEA SYSTEMS COMMAND

DTIC
ELECTE
MAY 03 1983
S D E

DTIC FILE COPY

88 05 02 076

UNCLASSIFIED

SECURITY CLASSIFICATION OF THIS PAGE (When Data Entered)

REPORT DOCUMENTATION PAGE		READ INSTRUCTIONS BEFORE COMPLETING FORM
1. REPORT NUMBER 82-230	2. GOVT ACCESSION NO. AD-A127529	3. RECIPIENT'S CATALOG NUMBER
4. TITLE (and Subtitle) AN ANALYSIS OF CONICAL INDENTATION OF AN ELASTIC/PERFECTLY PLASTIC HALF-SPACE BY NONLINEAR FINITE ELEMENT TECHNIQUES		5. TYPE OF REPORT & PERIOD COVERED M.S. Thesis, November 1982
7. AUTHOR(s) Takehiko Kato		6. PERFORMING ORG. REPORT NUMBER 82-230
9. PERFORMING ORGANIZATION NAME AND ADDRESS The Pennsylvania State University Applied Research Laboratory, P.O. Box 30 State College, PA 16801		8. CONTRACT OR GRANT NUMBER(s) N00024-79-C-6043
11. CONTROLLING OFFICE NAME AND ADDRESS Naval Sea Systems Command Department of the Navy Washington, DC 20362		10. PROGRAM ELEMENT, PROJECT, TASK AREA & WORK UNIT NUMBERS
14. MONITORING AGENCY NAME & ADDRESS (if different from Controlling Office)		12. REPORT DATE October 26, 1982
		13. NUMBER OF PAGES 119 pages
		15. SECURITY CLASS. (of this report) UNCLASSIFIED, UNLIMITED
		15a. DECLASSIFICATION/DOWNGRADING SCHEDULE
16. DISTRIBUTION STATEMENT (of this Report) Approved for public release, distribution unlimited, per NSSC (Naval Sea Systems Command), December 17, 1982		
17. DISTRIBUTION STATEMENT (of the abstract entered in Block 20, if different from Report)		
18. SUPPLEMENTARY NOTES		
19. KEY WORDS (Continue on reverse side if necessary and identify by block number) indentation, elastic, finite, element		
20. ABSTRACT (Continue on reverse side if necessary and identify by block number) A detailed analysis of the deformation and stress fields produced in an elastic/perfectly plastic half-space by a rigid conical indenter was performed using the elastic/plastic finite element code BOPACE-3D. The analysis considers: the elastic deformation and stress fields with finite element results being compared to the closed-form solutions obtained by Sneddon, the elastic/plastic deformation and stress fields, and the residual deformation and stress fields which have not been analyzed to date. A special loading technique was developed to find the residual solutions.		

UNCLASSIFIED

SECURITY CLASSIFICATION OF THIS PAGE(When Data Entered)

The included angle of the rigid conical indenter was set to $\alpha = 136^\circ$ to simulate a Vickers pyramidal indenter. Idealized soda-line glass was chosen as an elastic/perfectly plastic brittle material.

Stresses obtained during the loading-unloading cycle near the elastic/plastic boundary were transformed to the principal stresses and the residual principal stresses to allow analysis of median, radial and lateral crack initiation and propagation.

UNCLASSIFIED

SECURITY CLASSIFICATION OF THIS PAGE(When Data Entered)

ABSTRACT

A detailed analysis of the deformation and stress fields produced in an elastic/perfectly plastic half-space by a rigid conical indenter was performed using the elastic/plastic finite element code BOPACE-3D. The analysis considers: the elastic deformation and stress fields with finite element results being compared to the closed-form solutions obtained by Sneddon, the elastic/plastic deformation and stress fields, and the residual deformation and stress fields which have not been analyzed to date. A special loading technique was developed to find the residual solutions.

The included angle of the rigid conical indenter was set to $\alpha = 136^\circ$ to simulate a Vickers pyramidal indenter. Idealized soda-line glass was chosen as an elastic/perfectly plastic brittle material.

Stresses obtained during the loading-unloading cycle near the elastic/plastic boundary were transformed to the principal stresses and the residual principal stresses to allow analysis of median, radial and lateral crack initiation and propagation.

DTIC
COPY
INSPECTED

Accession For	
NTIS GRA&I	<input checked="" type="checkbox"/>
DTIC TAB	<input type="checkbox"/>
Unannounced	<input type="checkbox"/>
Justification	
By	
Distribution/	
Availability Codes	
Dist	Avail and/or Special
A	

TABLE OF CONTENTS

	<u>Page</u>
ABSTRACT	iii
LIST OF TABLES	vi
LIST OF FIGURES	vii
LIST OF SYMBOLS	x
ACKNOWLEDGEMENTS	xv
 Chapter	
I. INTRODUCTION	1
1.1 General Introduction.	1
1.2 Purpose of the Investigation.	2
1.3 Scope of the Investigation.	2
II. ELASTIC/PLASTIC FINITE ELEMENT METHOD.	4
2.1 General Concepts.	4
2.1.1 Stress-Strain Equations.	4
2.1.2 Incremental Stiffness Method	8
2.1.3 Other Stiffness Methods.	11
2.2 BOPACE - 3D	14
2.3 Verification of Nonlinear Finite Element Code.	15
2.3.1 Comparison to Yamada's Analysis.	15
2.3.2 Comparison to Marcal and King's Analysis	16
III. SOLUTION TECHNIQUES AND THE INDENTATION MODEL. . .	28
3.1 Method of Approach.	28
3.2 Finite Element Model and Grids.	29
3.3 Material Used in this Investigation	34
IV. ELASTIC AND ELASTIC/PLASTIC CONICAL INDENTATION. .	36
4.1 Introduction.	36
4.2 Method of Analysis.	37
4.3 Results and Discussion.	39
4.3.1 Elastic Conical Indentation.	44
4.3.2 Elastic/Plastic Conical Indentation. .	47
V. RESIDUAL SOLUTIONS FOR ELASTIC/PLASTIC CONICAL INDENTATION.	52
5.1 Introduction.	52
5.2 Method of Analysis.	52
5.3 Results and Discussion.	53

TABLE OF CONTENTS (Continued)

	<u>Page</u>
VI. ANALYSIS OF FRACTURE MECHANISMS INDUCED BY INDENTATION	62
6.1 Introduction	62
6.2 Failure Modes beneath the Indenter	62
6.2.1 Crack Systems near the Surface.	64
6.2.2 Subsurface Crack Systems.	64
6.3 Fracture Initiation and Propagation.	65
6.3.1 Identification of the Tensile Peak Stresses.	65
6.3.2 Critical Flaw Size.	66
6.3.3 Fracture Initiation and Propagation Zones	69
VII. CONCLUSIONS AND RECOMMENDATIONS	74
7.1 Conclusions.	74
7.2 Recommendations.	76
APPENDIX A: THE ELASTIC STRESS FIELDS FOR POINT, SPHERICAL AND CONICAL INDENTATION.	78
APPENDIX B: THE ANALYTICAL-EXPERIMENTAL EQUATIONS FOR ELASTIC/ PLASTIC INDENTATION.	97
BIBLIOGRAPHY	99

LIST OF TABLES

	<u>Page</u>
1. Tensile Peak Stresses and the Corresponding Crack System	67
2. Threshold Flaw Sizes for the Initiation of Each Crack System	70
3. Relationship between α , β , and b	95

LIST OF FIGURES

	<u>Page</u>
1. Stress-Strain Curve and Pertinent Material Properties for Yamada's Analysis.	17
2. Yamada's Finite Element Model for Aluminum Plate with Circular Penetration under Uniaxial Tension.	18
3. Finite Element Model Used in this Investigation	19
4. Nodal Forces F_y along the x-axis.	20
5. Nodal Forces F_x along the y-axis.	21
6. Nodal Displacement U_x along the x-axis.	22
7. Nodal Displacement U_y along the y-axis.	23
8. Improved Model Used in the Investigation of Plastic Regions	25
9. Character and Extent of Plastic Regions Obtained in this Investigation for Selected Load Factors.	26
10. Character and Extent of Plastic Regions Obtained in Marcal and King's Analysis for Selected Load Factors.	27
11. Axisymmetric Finite Element Model for Indentation Analysis.	30
12. Axisymmetric Finite Element Sub-Grids for Indentation Analysis (Insert A of Figure 11).	31
13. Axisymmetric Finite Element Sub-Grids for Indentation Analysis (Insert B of Figure 12).	32
14. Axisymmetric Finite Element Sub-Grids for Indentation Analysis (Insert C of Figure 13).	33
15. Stress-Strain Curve and Pertinent Material Properties of Idealized Soda-Lime Glass for Indentation Analysis.	35
16. Conical Indentation Geometry Beneath the Indenter	36

LIST OF FIGURES (Continued)

	<u>Page</u>
17. Non-dimensionalized Surface Stress $\sigma_{xx}/E\alpha\beta$ along the x-axis	40
18. Non-dimensionalized Surface Stress $\sigma_{zz}/E\alpha\beta$ along the x-axis	41
19. Non-dimensionalized Subsurface Stress $\sigma_{xx}/E\alpha\beta$ and $\sigma_{zz}/E\alpha\beta$ along the y-axis.	42
20. Non-dimensionalized Subsurface Stress $\sigma_{yy}/E\alpha\beta$ along the y-axis	43
21. Non-dimensionalized Pressure Distribution $\sigma_{yy}/E\alpha\beta$ on and adjacent to the Contact Zone	46
22. Elastic/Plastic Mesh Deformation	48
23. Plastic Zone and Elastic/Plastic Stress Trajectories	49
24. Comparison of Nodal Forces Resulting from Indentation and Equivalent Nodal Loads	54
25. Geometrical Comparison of Indentation Profile and Residual Crater.	55
26. Elastic/Plastic Residual Mesh Deformation.	57
27. Non-dimensionalized Residual Surface Stresses along the x-axis	58
28. Non-dimensionalized Residual Subsurface Stresses along the y-axis	59
29. Plastic Zone and Residual Stress Trajectories.	61
30. Schematic Diagram of Indentation Cracks.	63
31. Crack Initiation and Propagation Zones in the Loading Phase.	72
32. Crack Initiation and Propagation Zones during the Unloading Phase.	73
33. Point Indentation Geometry	79
34. Spherical Indentation Geometry beneath the Indenter.	81

LIST OF FIGURES (Continued)

	<u>Page</u>
35. Conical Indentation Geometry beneath the Indenter . . .	83
36. Comparison of Elastic Point, Spherical and Conical Stress Fields (I): Non-dimensionalized Stress σ_{xx} . . .	87
37. Comparison of Elastic Point, Spherical and Conical Indentation Stress Fields (II): Non-dimensionalized Stress, σ_{yy}	88
38. Comparison of Elastic Point, Spherical and Conical Indentation Stress Fields (III): Non-dimensionalized Stress, σ_{zz}	89
39. Comparison of Elastic Point, Spherical and Conical Indentation Stress Fields (IV): Non-dimensionalized Stress, σ_{xy}	90
40. Included Angle Effect of Conical Indentation (I): Non-dimensionalized Stress, σ_{xx}	91
41. Included Angle Effect of Conical Indentation (II): Non-dimensionalized Stress, σ_{yy}	92
42. Included Angle Effect of Conical Indentation (III): Non-dimensionalized Stress, σ_{zz}	93
43. Included Angle Effect of Conical Indentation (IV): Non-dimensionalized Stress, σ_{xy}	94

LIST OF SYMBOLS

D	diameter of spherical indenter
E	Young's Modulus
F	applied load
F_x, F_y	nodal forces
F_s	Sneddon's elastic applied load for conical indentation
F_f^e, F_f^p	load resultants generated from summation of the vertical nodal forces on the contact surface for the case of elastic and elastic/plastic finite element analysis
G	shear modulus
H	indentation hardness
H'	strain hardening rate
K_n^m	Sneddon's stress parameters for elastic conical indentation
Q	Sneddon's geometric parameter for elastic conical indentation
R	Hertzian geometric parameter ($= x^2 + z^2$)
S	plastic hardening parameter
U_x, U_y	nodal displacements
Y	yield strength
a	contact-surface radius for spherical indentation
b	contact-surface radius for conical indentation
c	plastic zone size
c_f	critical flaw size
d, e	Sneddon's geometric parameters for elastic conical indentation

LIST OF SYMBOLS (Continued)

f	maximum depth of Hertzian spherical indentation
h	Hertzian geometrical parameter for elastic spherical indentation
$P(\rho)$	surface pressure distribution for elastic conical indentation
P_o	mean pressure for spherical indentation
P_m	mean pressure for conical indentation
P'	mean pressure for point indentation
r	radial distance from origin $(= (x^2 + y^2 + z^2)^{\frac{1}{2}})$
t	Sneddon's geometric parameter for elastic conical indentation
u, v	horizontal and vertical displacements
v^R	residual vertical displacement
w	Hertzian geometric parameter for elastic spherical indentation
x, y, z	Cartesian coordinates
α	included angle of rigid conical indenter
β	excluded angle of rigid conical indenter $(= \frac{1}{2}(\pi - \alpha))$
γ_e	elastic geometric parameter for conical indentation
γ_H	geometric parameter of plastic hysteresis for conical indentation
Γ	crack surface energy
$\bar{\epsilon}$	effective (equivalent) strain
$d\epsilon_{ij}$	strain increments
$d\epsilon'_{ij}$	deviatoric strain increments

LIST OF SYMBOLS (Continued)

$d\epsilon_{ij}^p$	plastic strain increments
$\overline{d\epsilon^p}$	equivalent plastic strain increments
δ_{ij}	Kronecker's delta function
$\zeta, \rho, \bar{\phi}, \bar{\psi}$	Sneddon's geometric parameters
θ, ϕ	angles in spherical coordinate system
λ, μ	Lame's constants
$d\lambda$	Prandtl-Reuss scalar factor of proportionality
ν	Poisson's ratio
$\sigma_1, \sigma_2, \sigma_3$	principal stresses ($\sigma_1 \geq \sigma_2 \geq \sigma_3$)
$\sigma_{xx}, \sigma_{yy}, \sigma_{zz}, \tau_{xy}$	stresses for Cartesian coordinates
$\sigma_{rr}, \sigma_{\theta\theta}, \sigma_{\phi\phi}, \tau_{r\theta}$	stresses for spherical coordinates
σ^R	residual stress
$\bar{\sigma}$	equivalent stress
σ'_{ij}	deviatoric stress
$d\sigma_{ij}$	stress increments
$d\bar{\sigma}$	equivalent stress increments
$d\sigma'_{ij}$	deviatoric stress increments
[B]	displacement-strain matrix
[D]	stress-strain matrix
[D ^e]	elastic stress-strain matrix

LIST OF SYMBOLS (Continued)

$[D^P]$	plastic stress-strain matrix
$[D_T]$	material tangential modulus matrix
$\{\epsilon\}$	strain matrix
$\{\epsilon_0\}$	prestrain matrix
$\{\epsilon\}_n$	nodal strain matrix
$\{d\epsilon\}$	incremental strain matrix
$\{d\epsilon^P\}$	incremental plastic strain matrix
$[K]$	overall stiffness matrix
$[k]$	stiffness matrix
$[k^e]$	elastic stiffness matrix
$[k^P]$	plastic stiffness matrix
$[k_i]$	stiffness matrix after i^{th} increment
$[k_T]$	tangential stiffness matrix
$\{Q_i\}$	force matrix after i^{th} increment
$\{Q_0\}$	initial load matrix
$\{Q\}_{e,n,l}^{\epsilon_0}$	equivalent nodal load matrix corresponding to $\{\epsilon_0\}$
$\{Q\}_{e,n,l}^{\sigma_0}$	equivalent nodal load matrix corresponding to $\{\sigma_0\}$
$\{Q\}_n$	nodal force matrix
$\{dQ_i\}$	incremental force matrix after i^{th} increment
$\{dQ\}_n$	incremental nodal force matrix
$\{q_i\}$	displacement matrix after i^{th} increment

LIST OF SYMBOLS (Continued)

$\{q_o\}$	initial displacement matrix
$\{q\}_n$	nodal displacement matrix
$\{dq_i\}$	incremental displacement matrix after i^{th} increment
$\{dq\}_n$	incremental nodal displacement matrix
$\{\sigma\}$	stress matrix
$\{\sigma_o\}$	initial stress matrix
$\{d\sigma\}$	incremental stress matrix

ACKNOWLEDGMENTS

The author is indebted to Dr. Joseph C. Conway, Professor of Engineering Mechanics, and Dr. Robert N. Pangborn, Assistant Professor of Engineering Mechanics, for their assistance and encouragement in the research and preparation of this thesis. Appreciation is also extended toward Dr. R. G. Vos, Boeing Aerospace Company Missiles and Space Group, and Dr. Richard A. Queeney, Professor of Engineering Mechanics, for their helpful advice.

The author would also like to thank the people in the Applied Research Laboratory for their support of the research along with those who have critiqued this thesis under the contract with the Office of Naval Research, Research Initiation, Fund No. 7074.

CHAPTER I

INTRODUCTION

1.1 General Introduction

Elastic contact problems and elastic indentation problems involving the normal application of a load against an elastic half-space by a rigid body have been of considerable interest in various fields of applied mechanics. The point indentation problem was solved in closed-form by Boussinesq [1] and Michell [2]. The closed-form solution for spherical indentation was developed by Hertz [3] and Huber [4]. The conical indentation problem was solved in closed-form by Sneddon [5,6].

As the theory of plasticity has advanced, elastic/plastic contact-indentation problems have been approached analytically [7,8,9], experimentally [10,11] and numerically [12,13,14,15]. To the author's knowledge, the problem of normal loading of an elastic/perfectly plastic half-space by a rigid conical indenter has not been analyzed, despite the fact that aspects of this problem are of great interest in many fields, including indentation fracture mechanics. An analytical solution to this problem would be extremely difficult to develop but the use of the high-speed computer combined with the proper finite element code have made its solution possible. In this investigation a finite element code which incorporates the pure tangential stiffness incremental method was applied to obtain a solution to the problem of elastic/plastic conical indentation.

1.2 Purpose of the Investigation

The purpose of this investigation was to perform fundamental research on elastic/plastic conical indentation problems associated with the machining of brittle materials. It is anticipated that the design, fabrication and maintenance capabilities for brittle structures can be improved when the basic understanding of fundamental failure mechanisms associated with resultant generated elastic/plastic stress fields and residual stress fields is increased. The resultant axisymmetric elastic/plastic stress fields associated with both loading and unloading can then be related to median, radial and lateral cracking. In order to obtain this solution, it was necessary to apply axisymmetric elastic/plastic analysis and cyclic loading in the finite element program.

1.3 Scope of the Investigation

This investigation consists of four primary sections. The first section considers the development of a finite element model for the conical indentation problem and the verification of the model by comparing numerically generated results with the closed-form results for an elastic half-space derived by the well-known Sneddon solution. Secondly, an elastic/plastic conical indentation analysis is performed using the finite element model with plastic analysis capability to generate the elastic/plastic stress and strain fields and to determine the extent of plastic deformation near the indentation site. Thirdly, a loading-unloading cycle is simulated in order to obtain the residual

stress fields associated with elastic/plastic indentation. Finally, the results in terms of generated stress fields are related to the initiation and propagation of median, radial and lateral cracks beneath the indenter.

CHAPTER II

ELASTIC/PLASTIC FINITE ELEMENT METHOD

2.1 General Concepts

This section discusses the general concepts utilized in the solution of elastic/plastic problems by finite element techniques. This approach is based on a plastic stress-strain matrix derived from the Prandtl-Reuss equations, and on incremental or iterative stiffness methods.

2.1.1 Stress-Strain Equations

It has been well established that the plastic constitutive equation can be expressed in incremental form. In this investigation, the selected incremental plasticity relations conform to the Prandtl-Reuss flow rule, which is the usual flow rule associated with the well-known Huber-Mises yield surface criterion [7,16,17]. The Prandtl-Reuss flow rule uses the strain increment $d\epsilon_{ij}$, which is related to the stress increment $d\sigma_{ij}$. The incremental stress-strain relations with the differential form of the Huber-Mises yield surface criterion can be represented in matrix form as:

$$\{d\sigma\} = [D^P]\{d\epsilon\}, \quad (1)$$

where $\{d\sigma\}$ and $\{d\epsilon\}$ are defined as the column matrices of $d\sigma_{ij}$ and $d\epsilon_{ij}$, respectively; and $[D^P]$ is the plastic stress-strain matrix. Equation (1) can be expressed as:

$$d\sigma_i = \sum_{j=1}^6 \frac{\partial \sigma_i}{\partial \epsilon_j} d\epsilon_j \quad (i = 1, 2, 3, 4, 5, 6), \quad (2)$$

where the coefficients $\partial \sigma_i / \partial \epsilon_j$ are the partial stiffness components [28]. Hooke's law for isotropic elastic materials can be expressed in matrix form as:

$$\{\sigma\} = [D^e] \{\epsilon\}, \quad (3)$$

where the elastic stress-strain matrix $[D^e]$ is given as:

$$[D^e] = 2G \begin{pmatrix} \frac{1-\nu}{1-2\nu} & \frac{\nu}{1-2\nu} & \frac{\nu}{1-2\nu} & 0 & 0 & 0 \\ \frac{\nu}{1-2\nu} & \frac{1-\nu}{1-2\nu} & \frac{\nu}{1-2\nu} & 0 & 0 & 0 \\ \frac{\nu}{1-2\nu} & \frac{\nu}{1-2\nu} & \frac{1-\nu}{1-2\nu} & 0 & 0 & 0 \\ 0 & 0 & 0 & \frac{1}{2} & 0 & 0 \\ 0 & 0 & 0 & 0 & \frac{1}{2} & 0 \\ 0 & 0 & 0 & 0 & 0 & \frac{1}{2} \end{pmatrix} \quad (4)$$

For the elastic/plastic finite element method, the plastic stress-strain matrix $[D^p]$ for yielded elements takes the place of the elastic stress-strain matrix $[D^e]$.

The Prandtl-Reuss stress-strain relations for the deviatoric strain increment $d\epsilon'_{ij}$ during continued loading are:

$$d\epsilon'_{ij} = \sigma'_{ij} d\lambda + \frac{d\sigma'_{ij}}{2G}, \quad (5)$$

where

$$d\lambda = \frac{3}{2} \frac{d\bar{\epsilon}^P}{\bar{\sigma}} = \frac{3}{2} \frac{d\bar{\sigma}}{\bar{\sigma}H'} \quad (6)$$

$$\bar{\sigma} = \left(\frac{3}{2} \sigma'_{ij} \sigma'_{ij} \right)^{\frac{1}{2}}, \quad (7)$$

$$\bar{d\epsilon}^P = \left(\frac{3}{2} d\epsilon^P_{ij} d\epsilon^P_{ij} \right)^{\frac{1}{2}}, \quad (8)$$

and

$$H' = \frac{d\bar{\sigma}}{d\bar{\epsilon}^P} = \frac{\bar{\sigma}}{(\int d\bar{\epsilon}^P)}.$$

The Huber-Mises yield criterion and its differential form are:

$$\sigma'_{ij} \sigma'_{ij} = \frac{2}{3} \bar{\sigma}^2, \quad (10)$$

and

$$\sigma'_{ij} d\sigma'_{ij} = \frac{2}{3} \bar{\sigma} d\bar{\sigma} = \frac{4}{9} \bar{\sigma}^2 H' d\lambda. \quad (11)$$

From equations (5) and (11),

$$2G\sigma'_{ij} (d\epsilon'_{ij} - \sigma'_{ij} d\lambda) = \frac{4}{9} \bar{\sigma}^2 H' d\lambda.$$

Therefore,

$$d\lambda = \frac{\sigma'_{ij} d\epsilon'_{ij}}{S} = \frac{\sigma'_{ij} d\epsilon_{ij}}{S}, \quad (12)$$

where

$$S = \frac{2}{3} \bar{\sigma}^2 \left(1 + \frac{H'}{3G} \right). \quad (13)$$

From equations (6) and (12),

$$d\sigma'_{ij} = 2G \left(d\epsilon'_{ij} - \sigma'_{ij} \frac{\sigma'_{kl} d\epsilon_{kl}}{S} \right) = 2G \left(d\epsilon_{ij} - \delta_{ij} \frac{d\epsilon_{ii}}{3} - \sigma'_{ij} \frac{\sigma'_{kl} d\epsilon_{kl}}{S} \right). \quad (14)$$

The total stress increment $d\sigma_{ij}$ is:

$$\begin{aligned} d\sigma_{ij} &= d\sigma'_{ij} + \frac{E}{3(1-2\nu)} \delta_{ij} d\epsilon_{ii} \\ &= 2G \left(d\epsilon_{ij} + \frac{\nu}{1-2\nu} \delta_{ij} d\epsilon_{ii} - \sigma'_{ij} \frac{\sigma'_{kl} d\epsilon_{kl}}{S} \right). \end{aligned} \quad (15)$$

Equation (15) can be represented in matrix form as:

$$\{d\sigma\} = [D^P] \{d\epsilon\}, \quad (16)$$

where

$$[D^P] = 2G \cdot$$

$$\begin{bmatrix} \frac{1-\nu}{1-2\nu} - \frac{\sigma'^2_{xx}}{S} & \frac{1-\nu}{1-2\nu} - \frac{\sigma'^2_{yy}}{S} & & & \\ \frac{\nu}{1-2\nu} - \frac{\sigma'_{xx}\sigma'_{yy}}{S} & \frac{\nu}{1-2\nu} - \frac{\sigma'_{yy}\sigma'_{zz}}{S} & & & \\ \frac{\nu}{1-2\nu} - \frac{\sigma'_{xx}\sigma'_{zz}}{S} & -\frac{\sigma'_{yy}\tau'_{zz}}{S} & \frac{1-\nu}{1-2\nu} - \frac{\sigma'^2_{zz}}{S} & & \\ -\frac{\sigma'_{xx}}{S} \tau_{xy} & -\frac{\sigma'_{yy}}{S} \tau_{yz} & -\frac{\sigma'_{zz}\tau'_{xy}}{S} & \frac{1}{2} - \frac{\tau'^2_{xy}}{S} & \\ -\frac{\sigma'_{xx}}{S} \tau_{yz} & -\frac{\sigma'_{yy}}{S} \tau_{zx} & -\frac{\sigma'_{zz}}{S} \tau_{yz} & -\frac{\tau_{xy}\tau_{yz}}{S} & \frac{1}{2} - \frac{\tau'^2_{yz}}{S} \\ -\frac{\sigma'_{xx}}{S} \tau_{zx} & -\frac{\sigma'_{yy}}{S} \tau_{zx} & -\frac{\sigma'_{zz}}{S} \tau_{zx} & -\frac{\tau_{xy}\tau_{zx}}{S} & -\frac{\tau_{yz}\tau_{zx}}{S} & \frac{1}{2} - \frac{\tau'^2_{zx}}{S} \end{bmatrix} \quad \text{SYM.} \quad (17)$$

It is obvious that equation (16) is similar in form to equation (3) and that the necessary modification from elastic to elastic/plastic behavior

would be to replace $[D^e]$ by $[D^p]$ for yielded elements as successive yielding takes place. This procedure was developed by Marcal and King [18] and Yamada, Yoshimura and Sakurai [19,20].

2.1.2 Incremental Stiffness Method

In this investigation, the incremental pure tangential stiffness method was applied to construct the stiffness matrix. In this section, this incremental stiffness method is discussed. For elastic finite element analyses, the relationship between the nodal force and nodal displacement in each element n can be expressed in matrix form by:

$$\{Q\}_n = [k^e] \{q\}_n, \quad (18)$$

where

$$[k^e] = \iiint [B]^T [D^e] [B] dV, \quad (19)$$

and

$$\{\epsilon\}_n = [B] \{q\}_n, \quad (20)$$

$\{Q\}_n$ = equivalent nodal force matrix,

$\{q\}_n$ = equivalent nodal displacement matrix,

$[B]$ = displacement-strain matrix.

Integration of equation (19) is over the volume of the element. The matrix $[k^e]$ is called the stiffness matrix for the elastic elements. Similarly, for the plastic elements the stiffness matrix is expressed as:

$$[k^p] = \iiint [B]^T [D^p] [B] dV, \quad (21)$$

and

$$\{dQ\}_n = [k^p] \{dq\}_n . \quad (22)$$

The overall stiffness matrix $[k]$, which is an assemblage of the stiffness matrices $[k^e]$ and $[k^p]$, relates the nodal load increment $\{dQ\}$ to the nodal displacement increment $\{dq\}$ as:

$$\{dQ\} = [k] \{dq\} . \quad (23)$$

In order to solve the incremental equation (22) for an elastic-plastic problem, the load-deflection relation is first expressed by:

$$\begin{aligned} \{Q\}_n &= [k] \{q\}_n \\ &= \int_V [B]^T [D] [B] dV \{q\}_n \\ &= \int_V [B]^T \{\sigma\} dV . \end{aligned} \quad (24)$$

Using variational techniques,

$$\begin{aligned} \{dQ\}_n &= \int_V [B]^T \{d\sigma\} dV \\ &= \int_V [B]^T [D_T] \{d\epsilon\} dV \\ &= \int_V [B]^T [D_T] [B] dV \{dq\} \\ &= [k_T] \{dq\}_n , \end{aligned} \quad (25)$$

where $[D_T]$ and $[k_T]$ are called the material tangential modulus matrix, and the structural tangent stiffness matrix, respectively. It is

obvious that

$$\begin{aligned} [D^e] &= [D_T] , \\ [k^e] &= [k_T] \end{aligned}$$

for the elastic element and

$$\begin{aligned} [D^p] &= [D_T] , \\ [k^p] &= [k_T] \end{aligned}$$

for the plastic element.

The matrix $[D^p]$ is updated for each increment of load with computation of the plastic strain increment $\{d\epsilon^p\}$ at the yielded elements. The tangent stiffness matrix $[k_T]$ is computed at the end of each increment and used for each succeeding increment according to the following equations:

$$\{Q_i\} = \{Q_0\} + \sum_{j=1}^i \{dQ_j\} , \quad (26)$$

$$\{q_i\} = \{q_0\} + \sum_{j=1}^i \{dq_j\} , \quad (27)$$

and

$$[k_{i-1}] \{dq_i\} = \{dQ_i\} , \quad (28)$$

after the i^{th} increment where $\{Q_0\}$ and $\{q_0\}$ are the initial loads and displacements, usually null vectors. The above procedure is called the "incremental tangent stiffness method."

2.1.3 Other Stiffness Methods

For elastic/plastic finite element analyses, there are three major stiffness methods in addition to the incremental stiffness method, the iterative method, the initial strain method and the initial stress method. The iterative method [21,22] is used for elastic/plastic behavior when the deformation theory of plasticity is employed. Suppose the nonlinear nodal force and nodal displacement relation is expressed as:

$$\{Q\}_n = [k(q,Q)]\{q\}_n, \quad (29)$$

where the force $\{Q\}_n$ is entirely known and the displacement $\{q\}_n$ is entirely unknown. Such an iterative procedure involves an initial guess for the displacement $\{q\}_n^{(0)}$. An increasingly accurate series of vectors

$$\{q\}_n^{(1)}, \{q\}_n^{(2)}, \dots, \{q\}_n^{(N)} \quad (30)$$

is then generated with the objective being convergence to the exact vector $\{q\}$. The first iteration is obtained from:

$$[k(\{q\}_n^{(0)}, \{Q\}_n)] \{q\}_n^{(1)} = \{Q\}_n, \quad (31)$$

which has a formal solution:

$$\{q\}_n^{(1)} = [k^{(0)}]^{-1} \{Q\}_n. \quad (32)$$

The general procedure is to solve the equation:

$$[k(\{q\}_n^{(i-1)}, \{Q\}_n)] \{q\}_n^{(i)} = \{Q\}. \quad (33)$$

In order to find the current step, the displacements from the preceding step are used.

The major problems arising from the use of this method are:

- 1) there is no guarantee of convergence,
- 2) a new secant stiffness must be generated at each step, and
- 3) a new stiffness matrix must be inverted at each step.

The preceding two methods, incremental method and iterative method, are variable stiffness methods with stiffness matrices generated for each step. In addition to these variable stiffness methods, there are constant stiffness methods: the initial strain method and the initial stress method. These have been developed to reduce the computation time by utilizing the same stiffness throughout.

In the case of the initial strain method [22], use is made in the first iteration of the elastic stress-strain $[D^e]$ given by equation (4) to define $[k^e]$ of equation (19) and solve the equation:

$$[k^e] \{q\}^{(1)} = \{Q\}, \quad (34)$$

where $\{q\}^{(1)}$ defines the displacement vector for the first iteration and $\{Q\}$ is the total prescribed load vector. This yields an approximate displacement vector $\{q\}^{(1)}$. A corresponding approximate strain is found from:

$$\{\epsilon\}^{(1)} = [B] \{q\}^{(1)}. \quad (35)$$

Hence the exact stress corresponding to the approximate strain is:

$$\{\sigma\}^{(1)} = [D^e] \left\{ \{\epsilon\}^{(1)} - \{\epsilon_0\}^{(1)} \right\}, \quad (36)$$

where $\{\varepsilon_o\}^{(1)}$ is an artificially imposed prestrain. An artificial equivalent nodal load corresponding to $\{\varepsilon_o\}^{(1)}$ is:

$$\{Q\}_{e,n,\lambda}^{(1)} = \int_V [B]^T [D^e] \{\varepsilon_o\}^{(1)} dV . \quad (37)$$

The second iteration becomes:

$$[k^e] \{q\}^{(2)} = \{Q\} + \{Q\}_{e,n,\lambda}^{(1)} , \quad (38)$$

in which the second displacement vector $\{q\}^{(2)}$ is sought. The recurrent equation then becomes:

$$[k^e] \{q\}^{(i)} = \{Q\} + \{Q\}_{e,n,\lambda}^{(i-1)} . \quad (39)$$

For the initial stress method [22,23,24], equation (36) can be described as:

$$\{\sigma\}^{(1)} = [D^e] \{\varepsilon\}^{(1)} + \{\sigma_o\} , \quad (40)$$

where $\{\sigma_o\}^{(1)}$ is an artificially introduced prestress. Corresponding to $\{\sigma_o\}$ we have

$$\{Q\}_{e,n,\lambda}^{(1)} = - \int_V [B]^T \{\sigma_o\}^{(1)} dV . \quad (41)$$

The second iteration involves solution $\{q\}^{(2)}$ as:

$$[k^e] \{q\}^{(2)} = \{Q\} + \{Q\}_{e,n,\lambda}^{(1)} . \quad (42)$$

The recurrent equation is

$$[k^e] \{q\}^{(i)} = \{Q\} + \{Q\}_{e,n,l}^{(i-1)} \sigma_0 \quad (43)$$

2.2 BOPACE - 3D

Selection of the proper finite element program that has plastic analysis capability is an important aspect of solving the elastic/plastic indentation problem. Here, a finite element code BOPACE (THE BOEING PLASTIC ANALYSIS CAPABILITY FOR ENGINES) -3D Version 6.2, which was developed for analysis of the Space-Shuttle Main Engine (SSME), was chosen.

The program employs the Huber-Mises yield surface criterion, the Prandtl-Reuss flow rule, and an isotropic-kinematic hardening theory [7,25,26,27] as the basic concepts of the elastic/plastic theory. It also employs three types of stiffness methods [28],

- 1) the pure "tangent stiffness incremental" method,
- 2) the "constant-stiffness, initial stress" method, and
- 3) the "combined" method

for solution of elastic/plastic problems, and a modified Gauss wave-front solution procedure [22] for linear equation solution.

Development of the program has been strongly influenced by the following requirements:

- 1) the analysis of very high temperature, large plastic-creep effects and geometric nonlinearities,
- 2) treatment of cyclic thermal and mechanical loads,

- 3) improved material constitutive theory which closely follows actual behavior under variable temperature conditions, and
- 4) a stable numerical solution approach which avoids cumulative errors.

The above characteristics make it one of the most sophisticated finite element codes currently available for many types of general nonlinear problems.

2.3 Verification of Nonlinear Finite Element Code

Before applying the solution technique adopted in this investigation to the indentation problem, the technique was first verified by comparing generated elastic/plastic results for two variations of a selected plane-stress problem with those independently obtained from the literature. The plane-stress problem selected was a plate with a circular penetration subjected to uniaxial tension.

2.3.1 Comparison to Yamada's Analysis

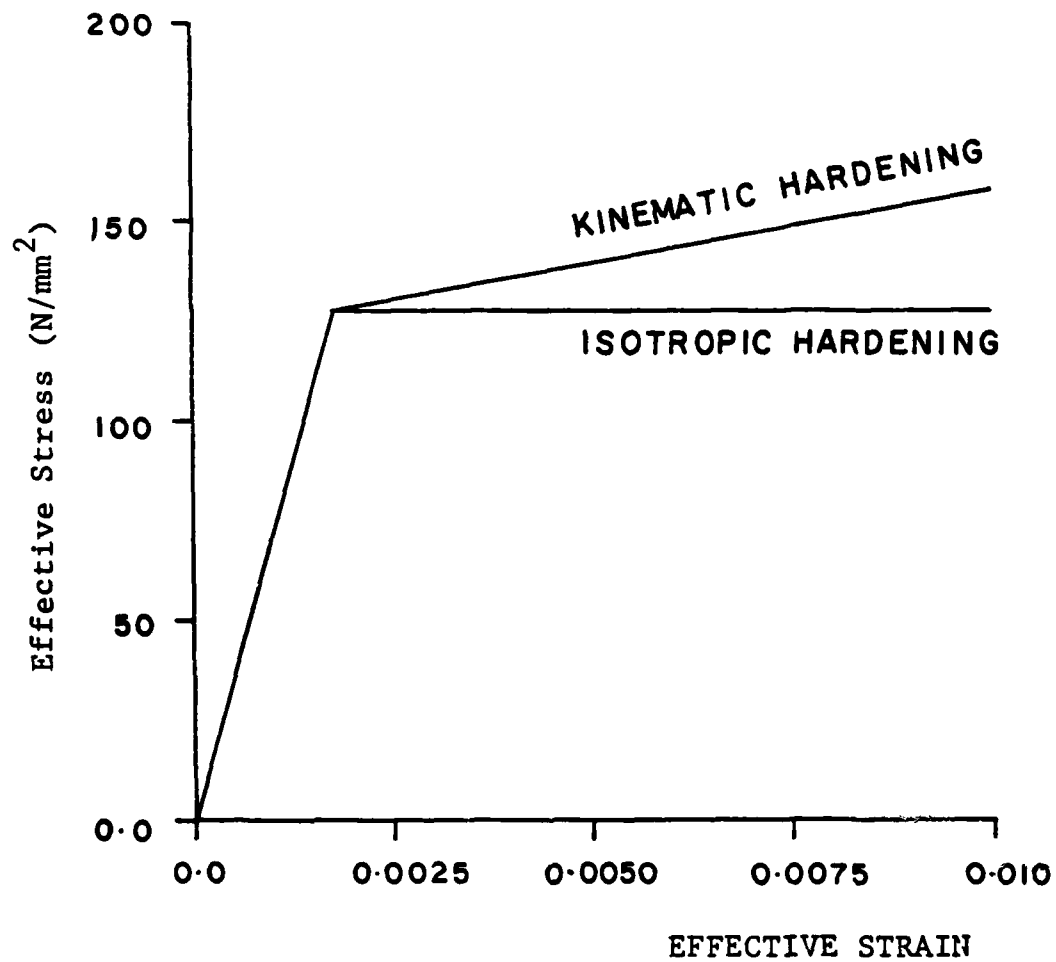
Here, the results obtained from the elastic/plastic finite element code used in this investigation are compared to those obtained by Yamada [Personal Note] for an aluminum plate with a circular penetration subjected to uniaxial tension. The comparison is made in terms of forces and displacements along the vertical and horizontal symmetry axes of the plate for the same nodal coordinates. The Yamada solution employs an incremental theory upon which many current nonlinear finite element codes are based [NASTRAN, NONSAP, etc.]

The stress-strain curve and pertinent material properties for the aluminum plate material are shown in Figure 1 for both isotropic and kinematic hardening. Figures 2 and 3 show the finite element meshes adopted by Yamada and in this investigation, respectively. Both meshes employ the same nodal point coordinates for easy comparison of solutions but different element shapes since Yamada's program considers only triangular elements and the finite element code adopted in this investigation utilizes quadrilateral elements. This resulted in an apparent distortion of quadrilateral elements (Figure 3). Due to symmetry, only the first quadrant of the plate was discretized. A uniform tensile stress of 39.2 N/mm^2 , which was selected in the Yamada solution, was applied in the y-direction along the upper edge of the plate.

Comparisons of the nodal forces and displacements along the horizontal and vertical axes of symmetry are shown in Figures 4 through 7. Results obtained from the two finite element codes are within 10 percent, with the differences caused primarily by the dissimilarity of element shapes. Theoretically, the accuracy could be improved for a given number of nodes by using quadrilateral elements, since the increased degrees-of-freedom would permit a closer approximation to the displacements within an element [22,23].

2.3.2 Comparison to Marcal and King's Analysis

In the previous section, a coarse grid model was used to compare two different solution techniques. In order to determine the extent and character of the plastic region as a function of applied tensile

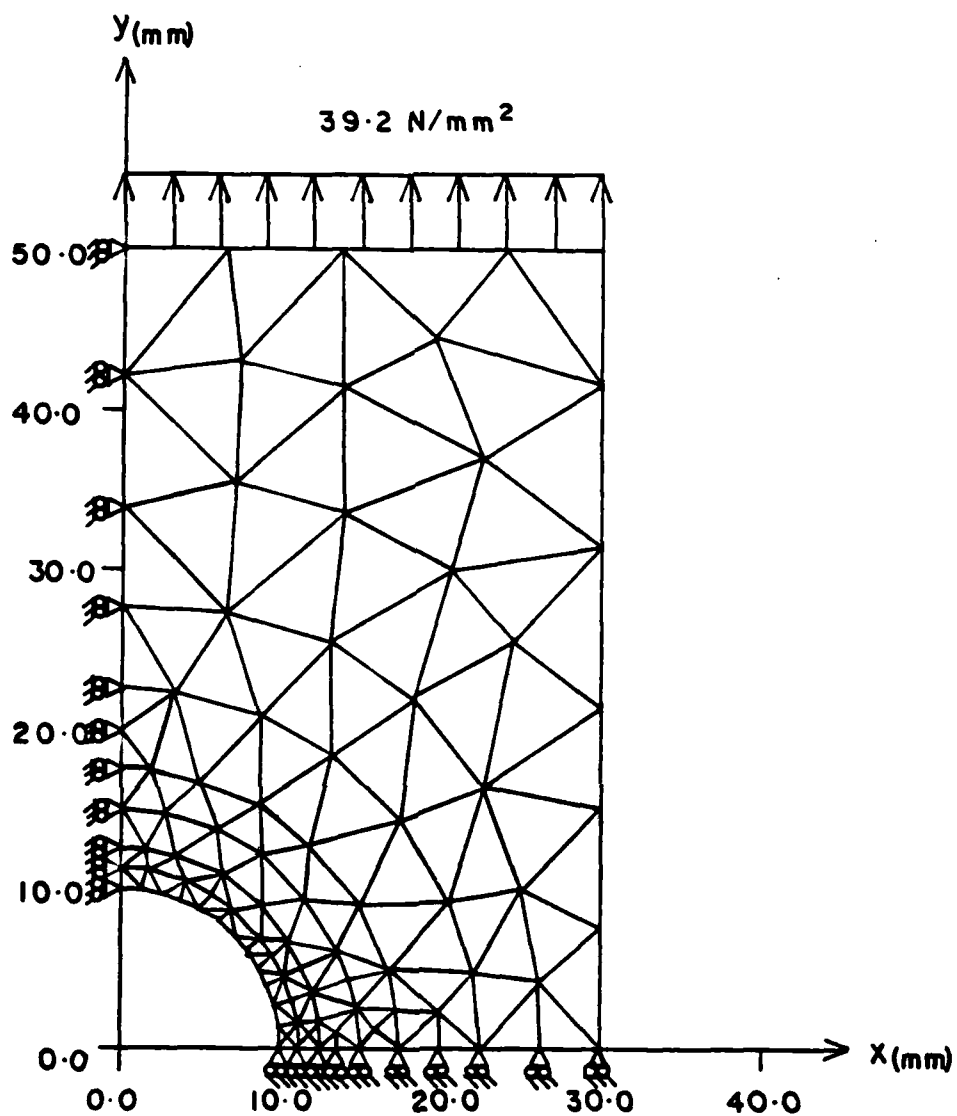


Young's Modulus = 73550 (N/mm²)

Poisson's Ratio = 0.32

Yield Strength = 127.5 (N/mm²)

Figure 1. Stress-Strain Curve and Pertinent Material Properties for Yamada's Analysis.

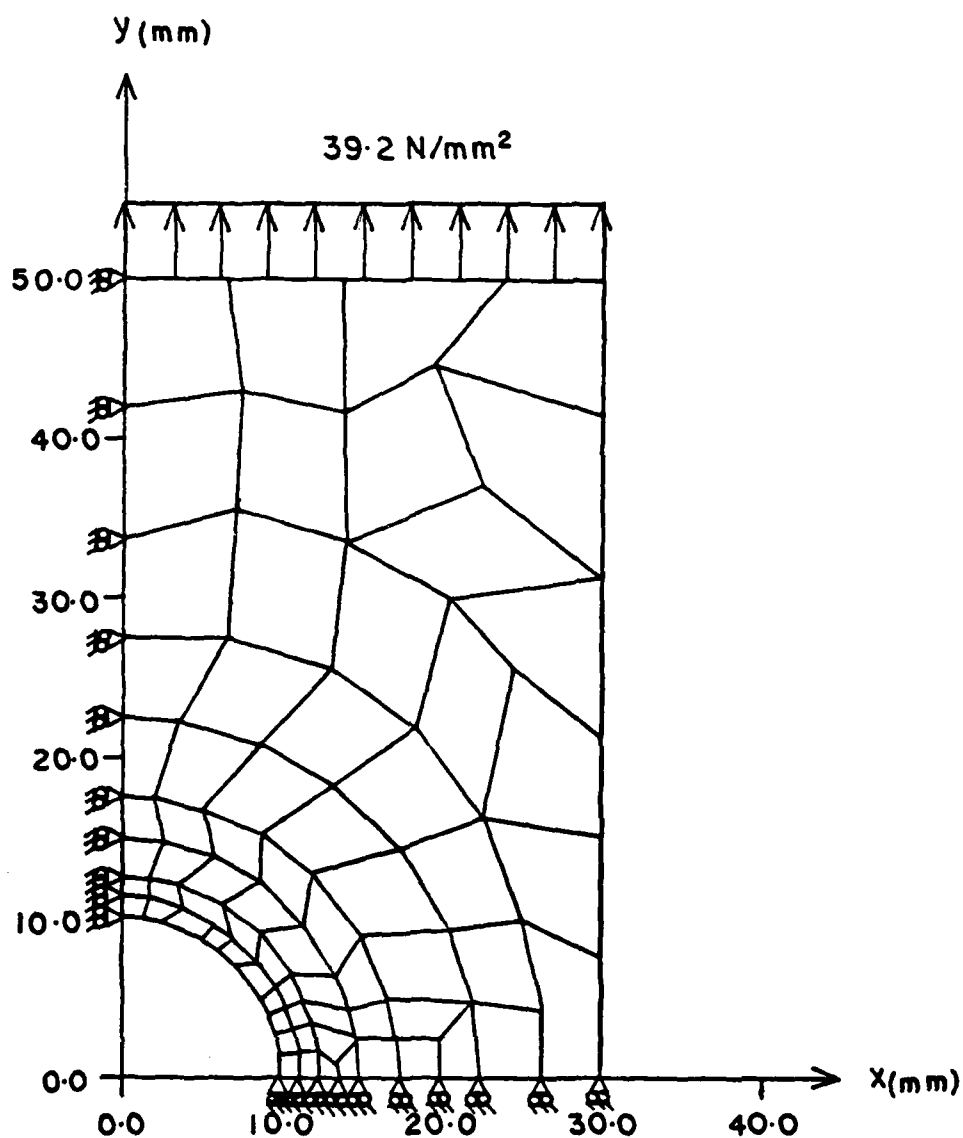


Thickness = 3.0 mm

Number of Nodes = 97

Number of Elements = 151

Figure 2. Yamada's Finite Element Model for Aluminum Plate with Circular Penetration under Uniaxial Tension.

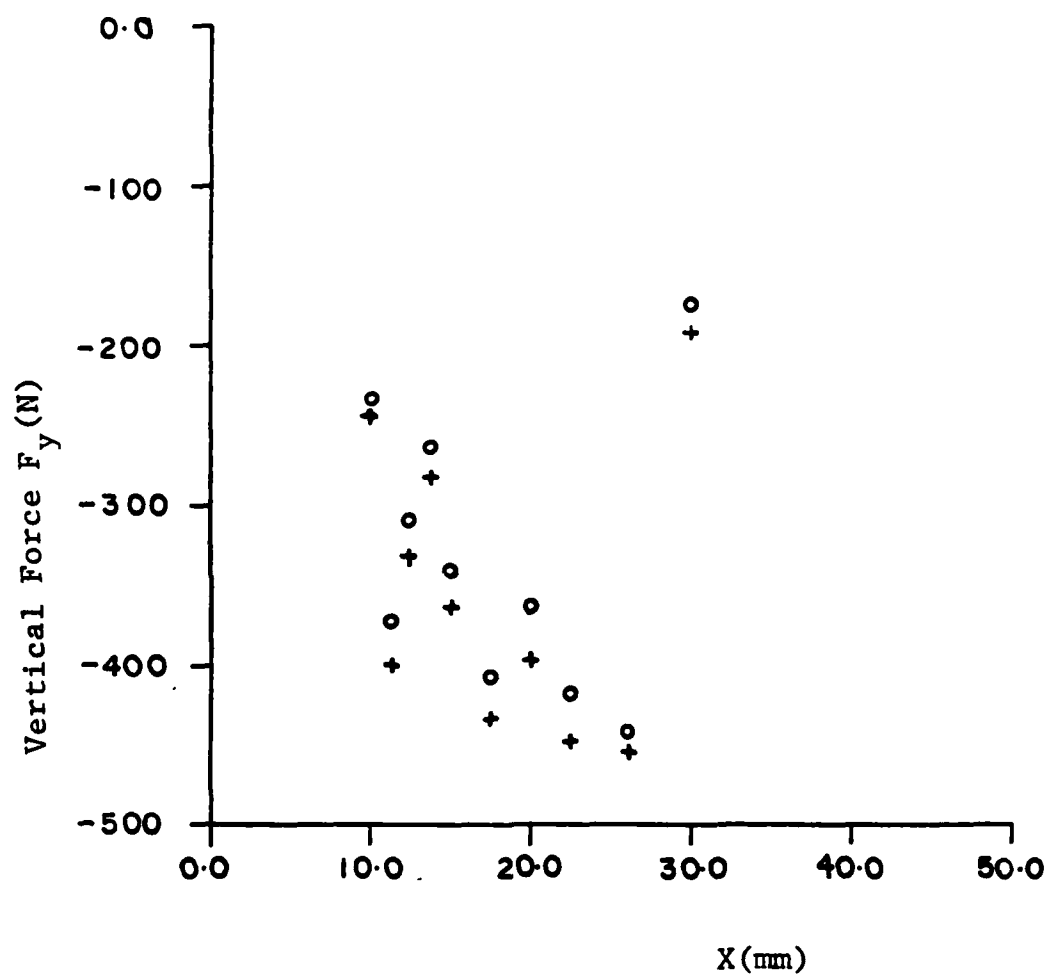


Thickness = 3.0 mm

Number of Nodes = 94

Number of Elements = 70

Figure 3. Finite Element Model Used in This Investigation.



o = Yamada's Analysis

+ = BOPACE

Figure 4. Nodal Forces F_y along the x-axis

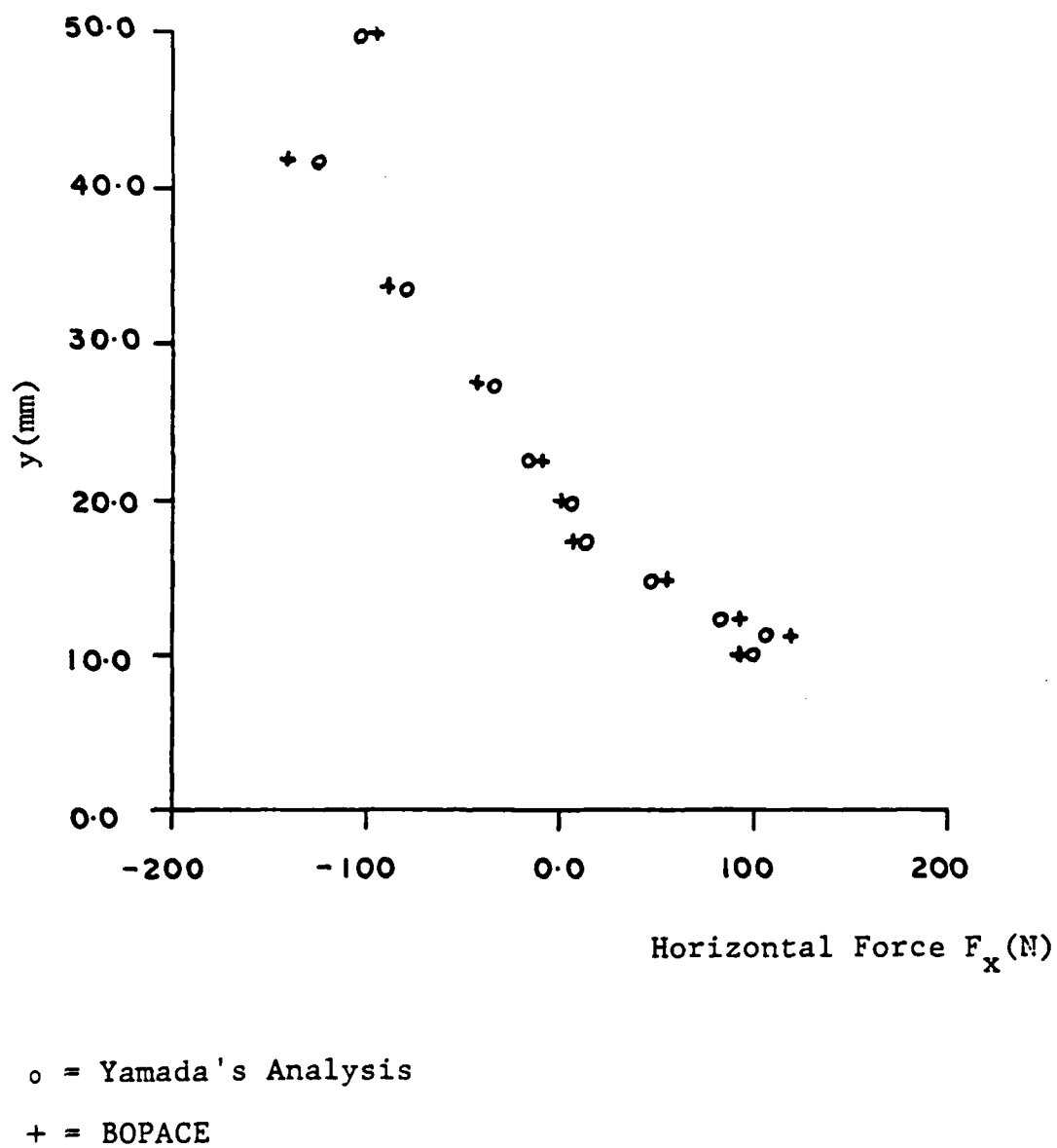
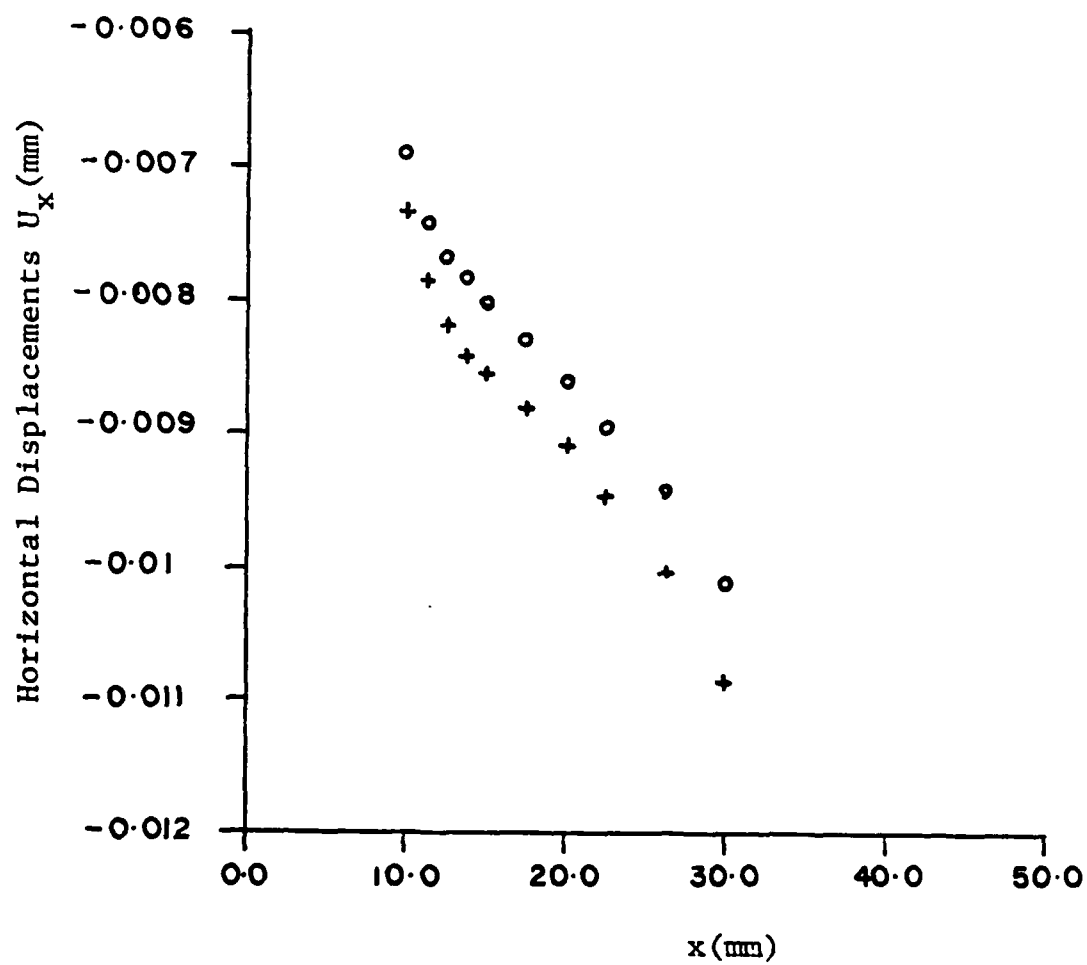


Figure 5. Nodal Forces F_x along the y-axis.



o = Yamada's Analysis

+ = BOPACE

Figure 6. Nodal Displacement U_x along the x -axis.

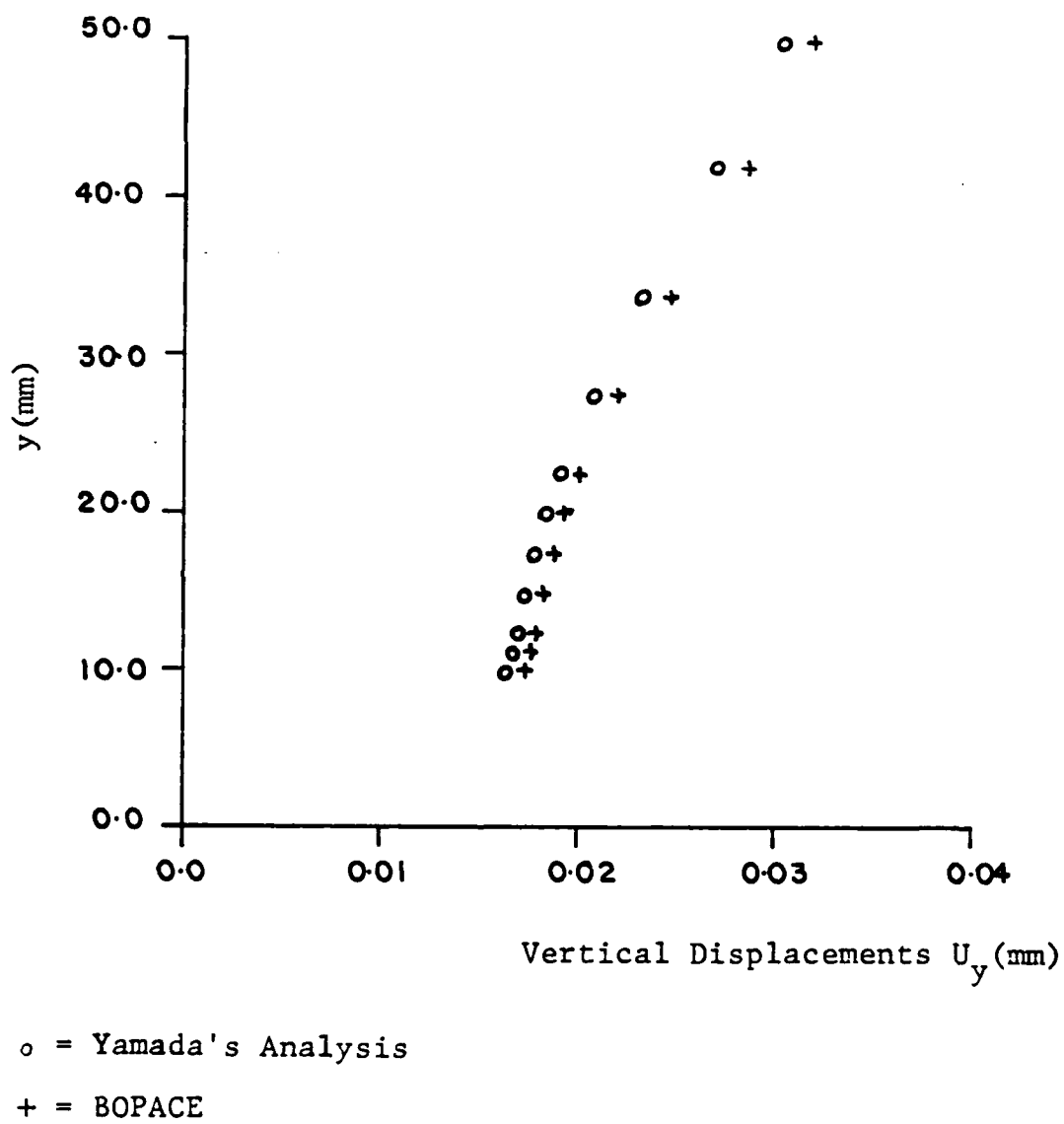
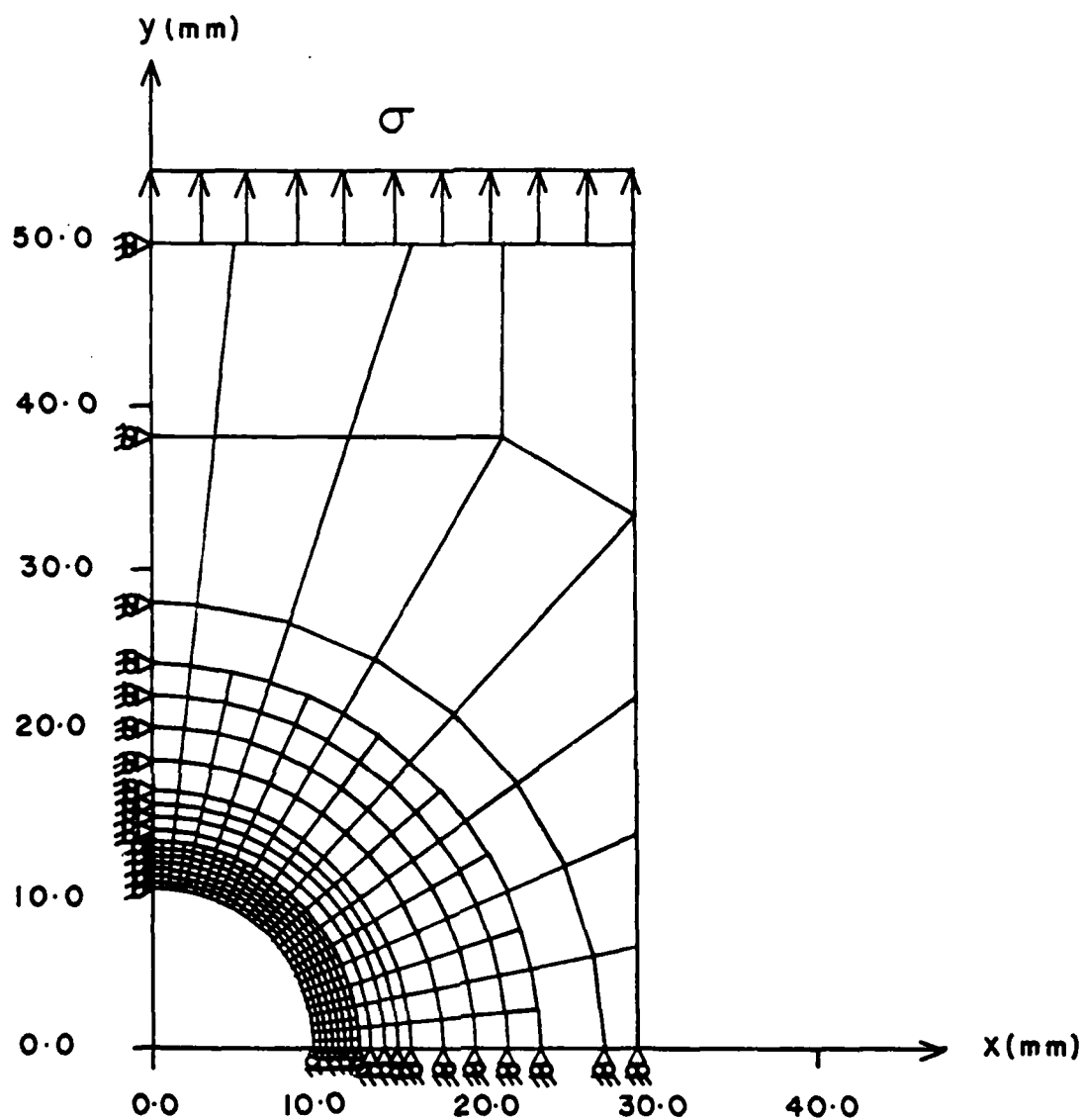


Figure 7. Nodal Displacements U_y along the y-axis.

stress, the model was reconstructed so that nodal density near the stress concentration would be increased. Through this remeshing, the number of nodes and elements and the maximum wavefronts were increased to 399, 350 and 33 from 94, 70 and 15, respectively. This improved model is shown in Figure 8. The material used for this investigation was linear strain-hardening aluminum, with the following mechanical properties; Young's modulus 7000 kg/mm^2 , Poisson's ratio 0.2, Yield stress 24.3 kg/mm^2 , strain hardening rate 225 kg/mm^2 . These values were obtained from Zienkiewicz's [21] and Marcal and King's [18] finite element analysis of a linear strain-hardening aluminum perforated strip, whose diameter-width-height ratio was 1:2:3.6 instead of 1:3:5 of this investigation.

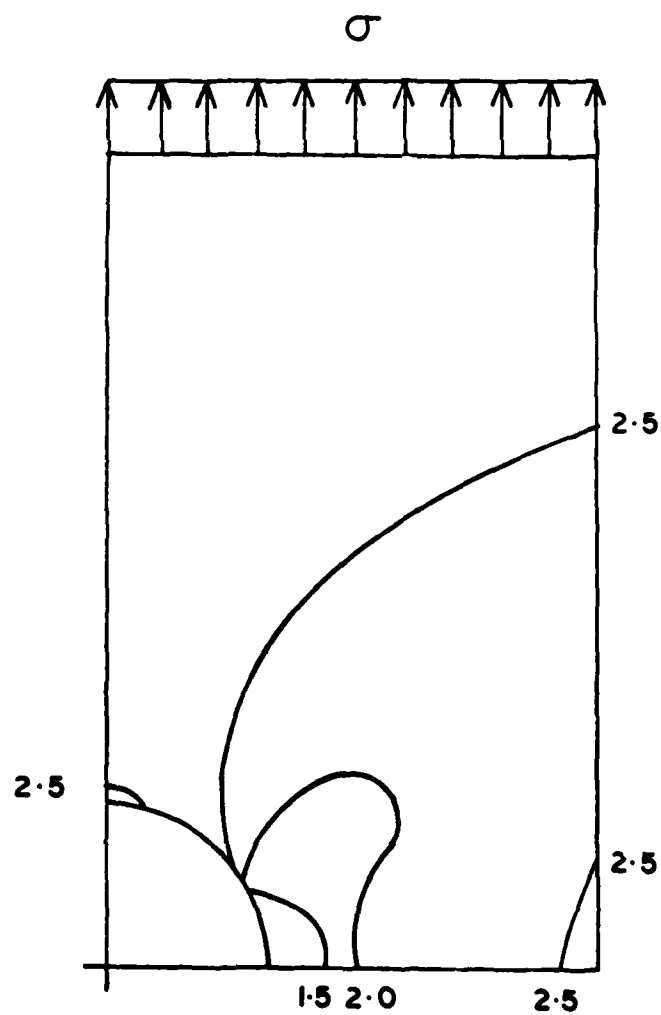
The plastic regions for load factors of 1.5, 2.0 and 2.5 are shown in Figure 9. A load factor of 1.0 represents the load required to cause incipience of yielding in the plate. Load factors of 1.5, 2.0 and 2.5 resulted in progressive yielding of the plate near the circular penetration. Figure 10 shows the plastic regions obtained by Marcal and King. Comparison of Figure 9 and 10 indicates that the character and extent of the plastic regions are nearly identical for both analyses in spite of the shape difference of the specimens.



Number of Nodes = 399

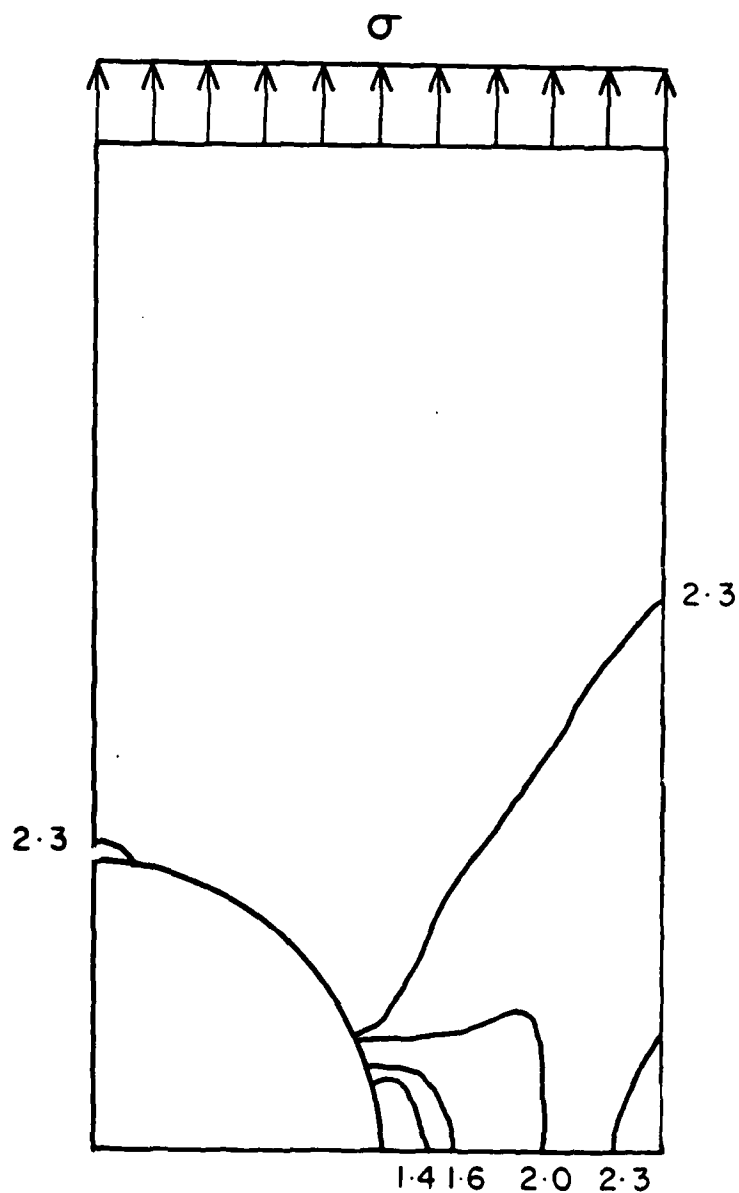
Number of Elements = 350

Figure 3. Improved Model used in the Investigation of Plastic Regions.



Diameter:Width:Height = 1:3:5

Figure 9. Character and Extent of Plastic Regions Obtained in this Investigation for Selected Load Factors.



Diameter:Width:Height = 1:2:3.6

Figure 10. Character and Extent of Plastic Regions Obtained in Marcal and King's Analysis for Selected Load Factors.

CHAPTER III

SOLUTION TECHNIQUES AND THE INDENTATION MODEL

3.1 Method of Approach

Since an analytical solution to the elastic/plastic problem is not available at this time, the investigation of elastic/plastic conical indentation was accomplished entirely by finite element techniques. The objective was to develop and demonstrate numerical techniques which can be applied to elastic/plastic problems involving flow, fracture and residual stress effects beneath a conical indenter. These techniques will be explained in greater detail in subsequent chapters.

In the loading procedure, three separate stages were required to simulate elastic/plastic loading and unloading of a half-space by a rigid conical indenter. In the first stage, initial loading was applied through nodal displacements selected to simulate conical indentation at the contact-surface. Displacement loading was used since there is no analytical method currently available for predicting the load distribution for elastic/plastic conical indentation. The second stage was designed to obtain the equivalent surface nodal loads which would result in the same stress and displacement fields as those obtained by the displacement loading of the first stage. This was accomplished by using the numerical results obtained following the displacement loading of the first stage. In the third stage, the equivalent surface nodal loads were reduced to zero in order

to simulate unloading of the specimen. During this stage, the residual displacement beneath the indenter and the residual stress fields were generated.

The error norm for each stage in the analysis was limited to within 5 percent.

3.2 Finite Element Model and Grids

The axisymmetric finite element idealization for the indentation analysis of the half-space is shown in Figures 11 through 14. Figure 11 shows the overall outline of the model and Figures 12, 13, and 14 are sub-grids which must be inserted into the appropriate central sectors of Figures 11, 12, and 13, respectively, to construct the entire model. There are 470 nodes and 427 elements, and the maximum wavefront that governs CPU-time [22] is 15. Loading is applied in the vertical direction along the y-axis, as shown in the figures. The finite element mesh was designed to meet the following objectives:

- 1) to reduce the maximum wavefront in order to minimize CPU-time and core storage requirements,
- 2) to reduce the occurrence of singularities for elements in regions of primary interest by considering the shapes of elements,
- 3) to reduce the number of elements in regions that are of less interest by using curved boundary elements which include intermediate nodes at the edge of the elements,
- 4) to limit the maximum output to 30,000 printed lines, which is the maximum number of printed lines for JOB-category 5

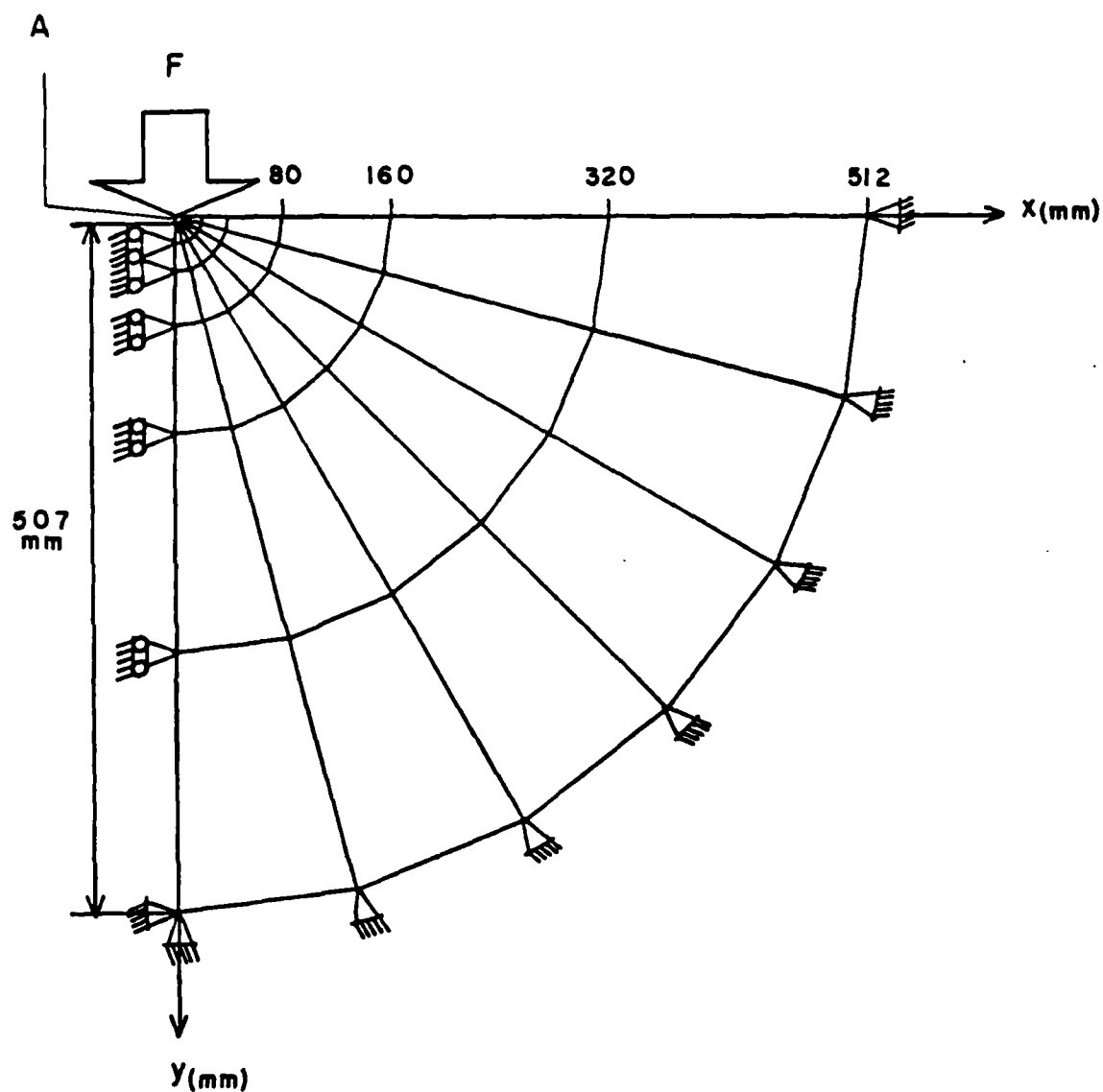


Figure 11. Axisymmetric Finite Element Model for Indentation Analysis.

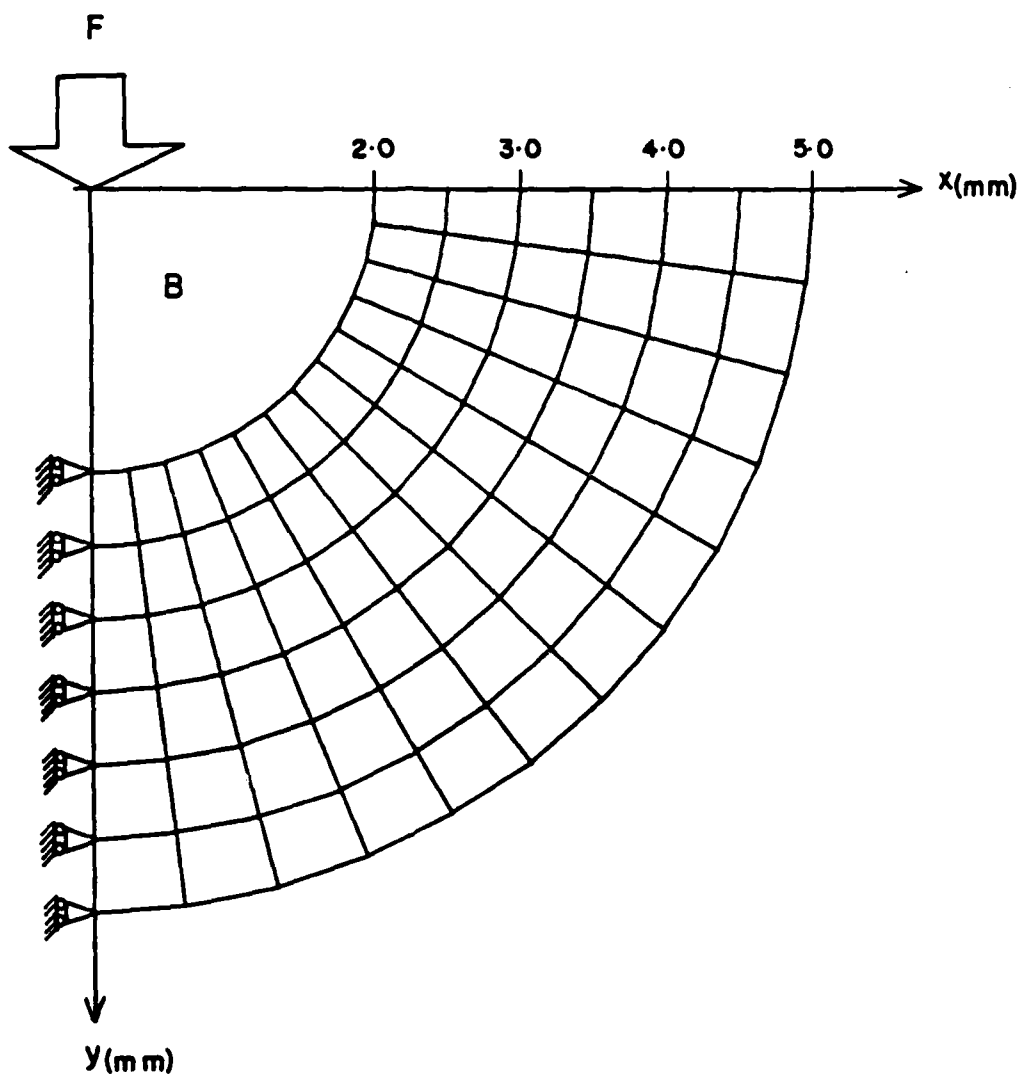


Figure 12. Axisymmetric Finite Element Sub-Grids for Indentation Analysis (Insert A of Figure 11).

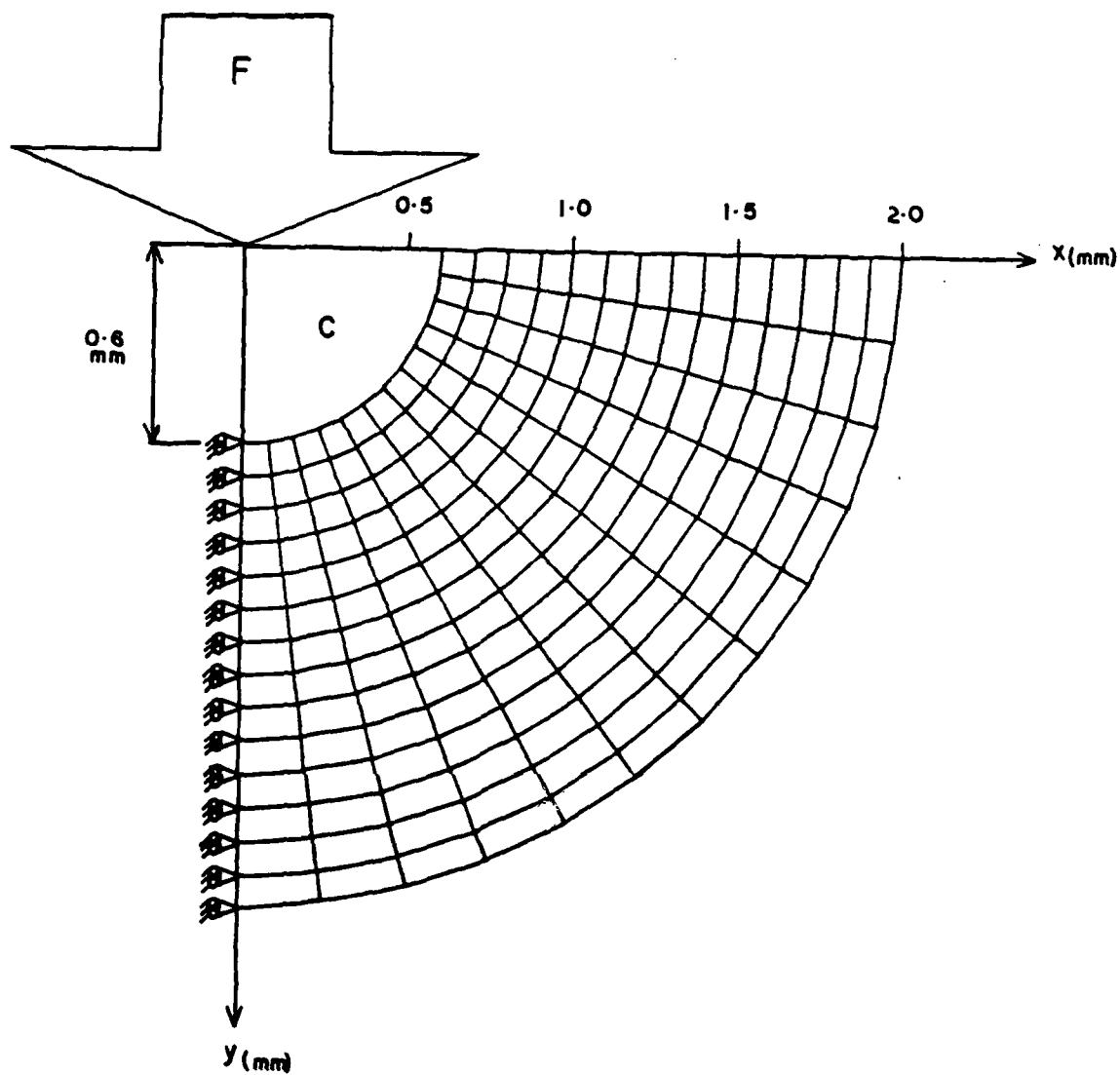


Figure 13. Axisymmetric Finite Element Sub-Grids for Indentation Analysis (Insert B of Figure 12).

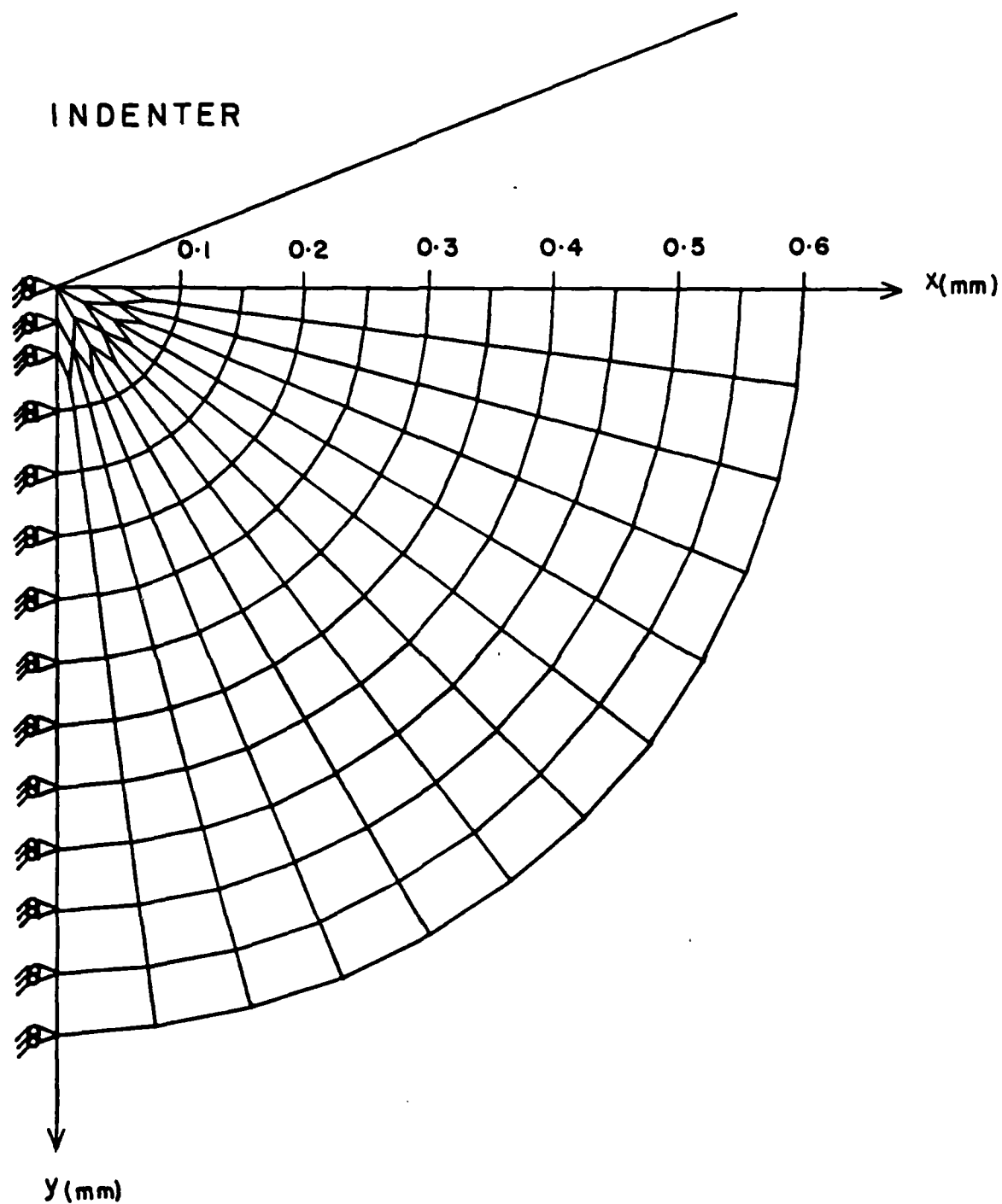


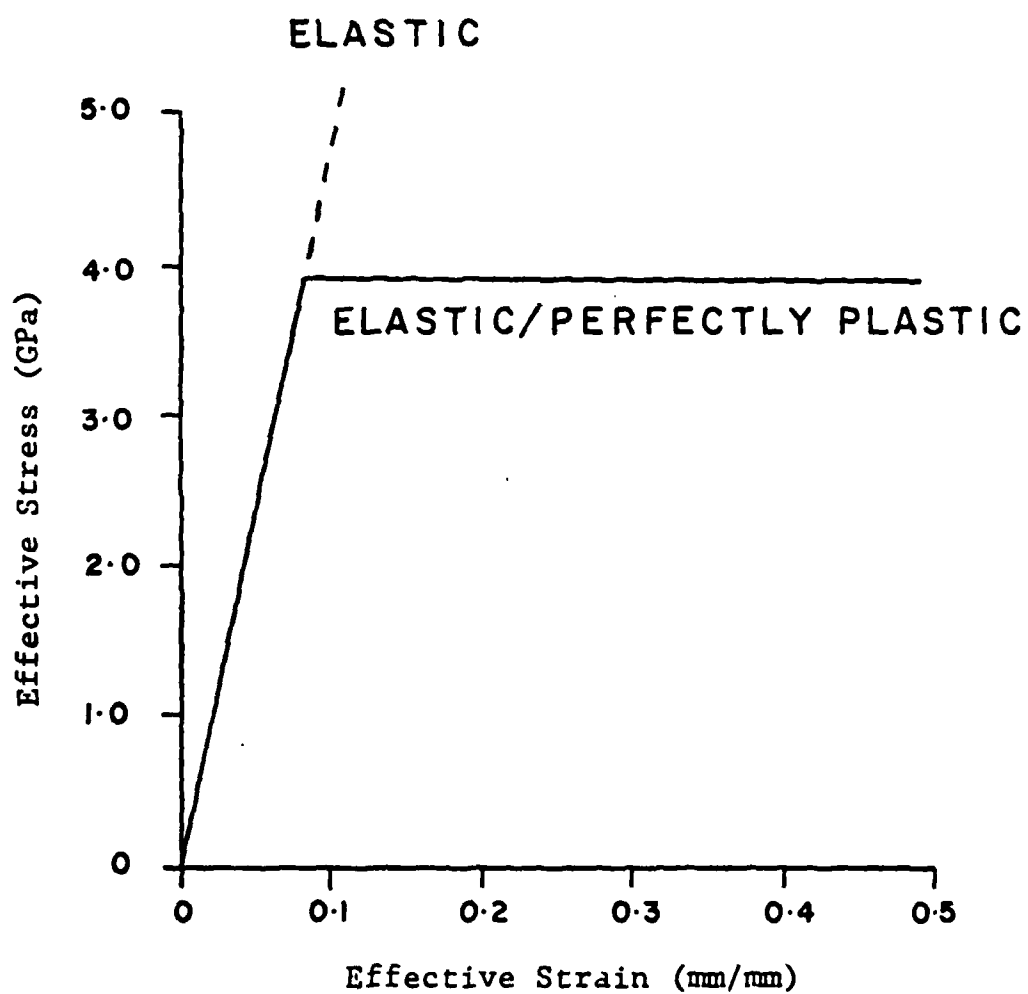
Figure 14. Axisymmetric Finite Element Sub-Grids for Indentation Analysis (Insert C of Figure 13).

of PSU-IBM 370, by controlling the total number of elements,

- 5) to generate or preprocess the input data easily.

3.3 Material Used in this Investigation

The material selected for this analysis was idealized soda-lime glass. Soda-lime glass is a brittle material used in many fracture mechanics experiments and its behavior is well established for Vickers pyramidal indentation and spherical indentation. It is known that soda-lime glass exhibits elastic/perfectly plastic behavior when subjected to indentation loading. It was thus an appropriate material for the nonlinear finite element model. The stress-strain curve for this elastic/perfectly plastic soda-lime glass is shown in Figure 15 together with its pertinent material properties.



Young's Modulus = 49.0 (GPa)

Poisson's Ratio = 0.22

Yield Strength = 3.92 (GPa)

Figure 15. Stress-Strain Curve and Pertinent Material Properties of Idealized Soda-Lime Glass for Indentation Analysis.

CHAPTER IV

ELASTIC AND ELASTIC/PLASTIC CONICAL INDENTATION

4.1 Introduction

The finite element model for conical indentation of a half-space was formulated so that it could be applied to both elastic and elastic/plastic indentations. This required the method of loading to be carefully considered. For the case of elastic indentation, the pressure distribution, resultant forces and displacements directly beneath the indenter can be obtained from a closed-form solution by Sneddon, as shown in Appendix A. Each of these parameters can be used as load input to the finite element program at appropriate nodes beneath the indenter to model elastic conical indentation. As the material begins to yield, the pressure distribution, and resultant forces beneath the indenter are completely unknown, while the displacement field is partially specified. In the case of the displacement field, nodal points on the contact surface must conform to the profile of the indenter. For regions adjacent to the contact surface, the displacement of surface nodes would be automatically generated as output of the finite element code.

In order to generate a model which can apply to both elastic and elastic/plastic conical indentations, it was decided to input load through the displacements of surface nodes along the contact surface. This would allow direct comparison of the finite element results with those obtained from the closed-form solution for

elastic indentation, and also afford partial specification of the displacement field beneath the indenter for elastic/plastic indentation.

4.2 Method of Analysis

The coordinate system adopted in the analysis, the geometrical characteristics associated with the indenter geometry, and the displacement loading are shown in Figure 16. In order to simulate Vickers indentation, the included angle of the indenter was set to $\alpha = 136$ degrees.

An elastic finite element analysis was performed initially to verify the finite element model. Here, the contact surface radius was selected as $b = 0.30$ mm, resulting in a depth of indentation $v_{\max} = (d+e) = 0.19$ mm that was computed from the Sneddon solution. The Sneddon solution also allowed specification of both vertical and horizontal displacements of surface nodes within and adjacent to the contact surface. In the finite element analysis, however, only the vertical displacement of the nodes on the contact surface was specified. Horizontal displacement was computed as output in order to allow a greater degree of freedom on and adjacent to the contact surface.

Following the elastic finite element analysis, the elastic/plastic finite element analysis was conducted. As described earlier, the displacement field beneath the indenter is only partially described in this case. A trial elastic/plastic run was made, in which the initial vertical displacements of nodes within the contact surface

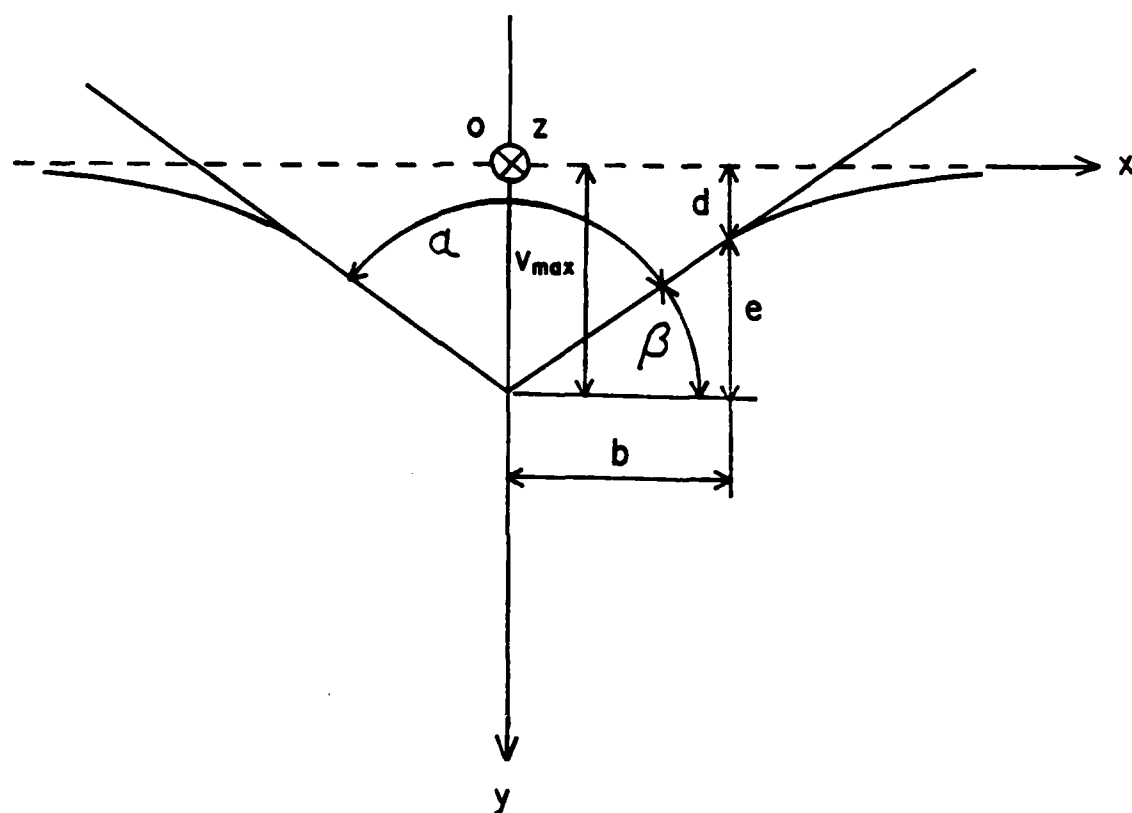
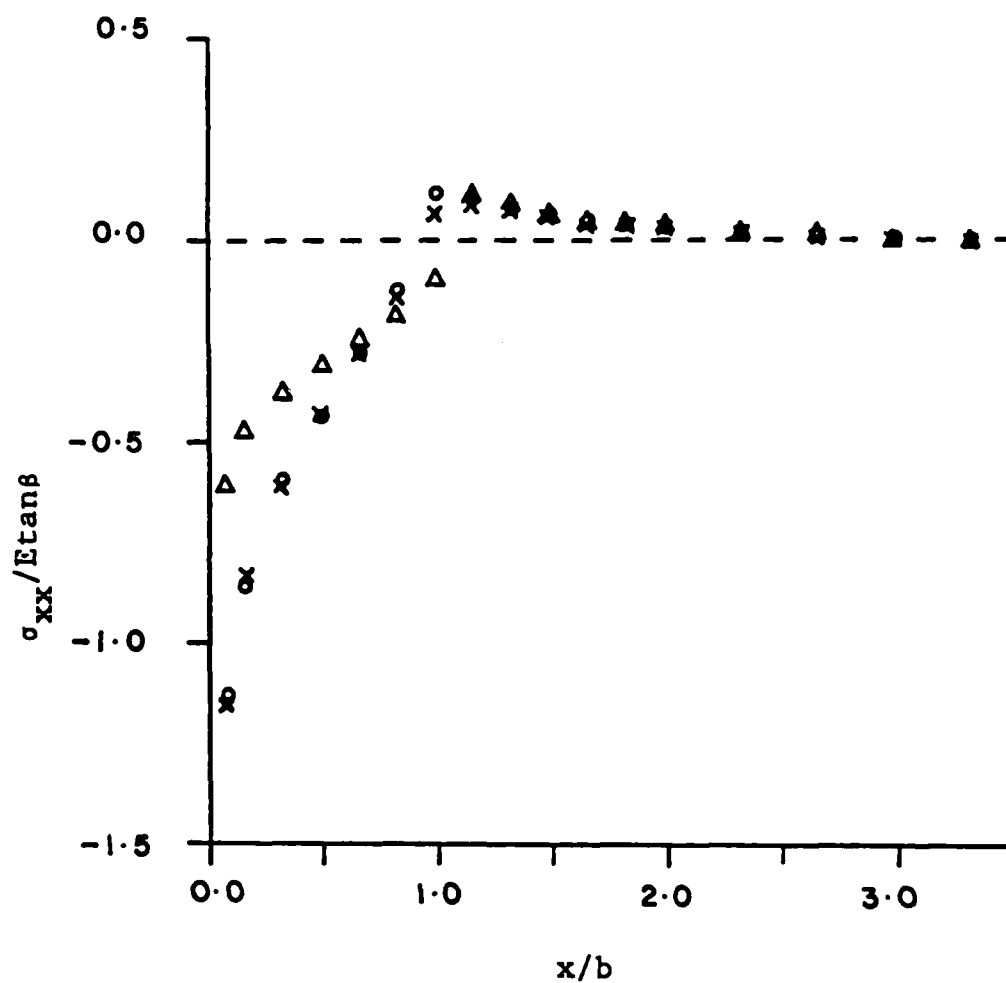


Figure 16. Conical Indentation Geometry Beneath the Indenter.

were obtained from the Sneddon solution for assumed elastic/perfectly plastic behavior of soda-lime glass. Following this step, nodal force resultants were checked for the nodes adjacent to the contact surface to determine whether any vertical tensile tractions existed. This condition, when encountered, indicated a divergence of elastic/plastic surface deformations from the elastic Sneddon displacements, resulting in "overlap" of vertical surface displacements with the indenter profile. This was alleviated through trial reductions of the indentation depth that were repeated until the vertical tensile tractions were reduced to zero or assumed small compressive values. For soda-lime glass, it was found that closed-form computation of vertical displacements on the contact surface resulted in no tensile tractions for the selected contact surface radius and therefore applied for elastic/plastic indentation.

4.3 Results and Discussions

The elastic and elastic/plastic results expressed in terms of surface stresses and stresses directly beneath the conical indenter are shown in Figures 17 to 20. In these figures, elastic results obtained from the closed-form Sneddon solution and the elastic finite element analysis are compared to those obtained in the elastic/plastic finite element analysis. In each case stresses are non-dimensionalized with respect to the factor $E\alpha\beta = (eE/b)$, while distances along the free surface of the half-space and beneath the indenter are nondimensionalized with respect to the contact surface radius, b .

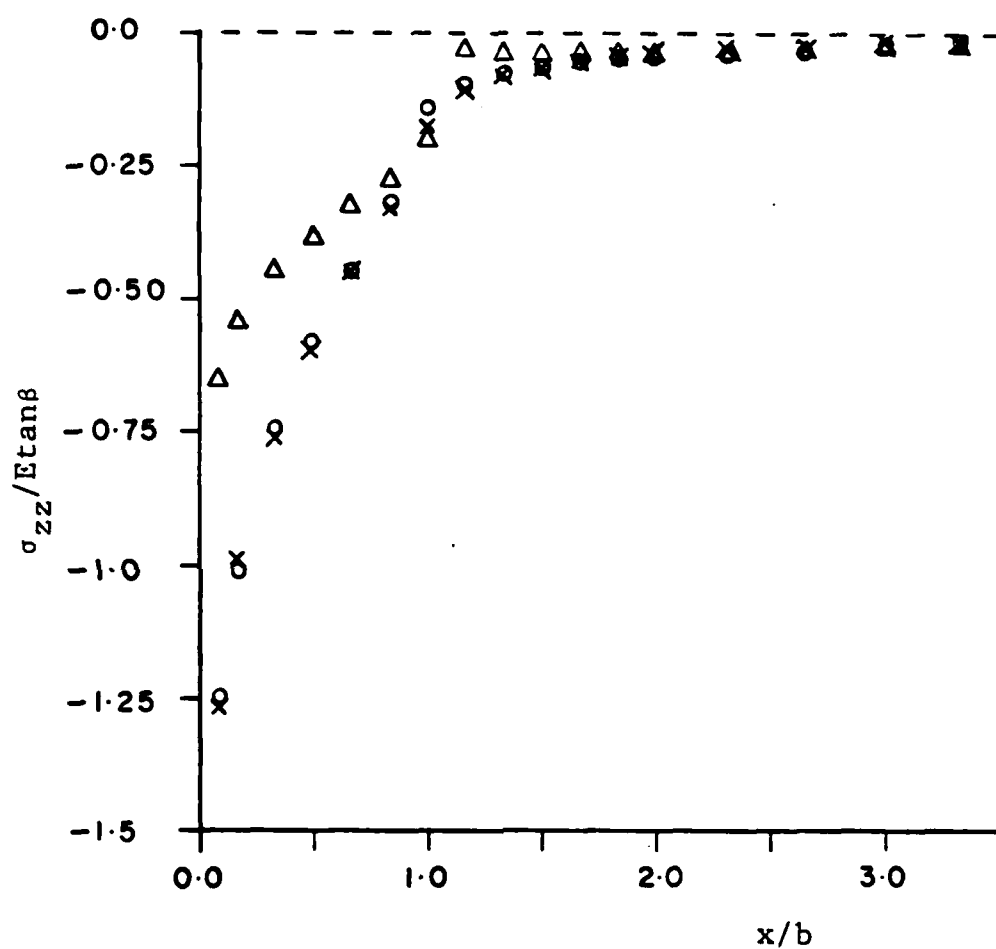


o = Sneddon Analysis

x = Elastic Finite Element Analysis

Δ = Elastic/Plastic Finite Element Analysis

Figure 17. Non-dimensionalized Surface Stress $\sigma_{xx}/E\epsilon\alpha\delta$ along the x-axis.

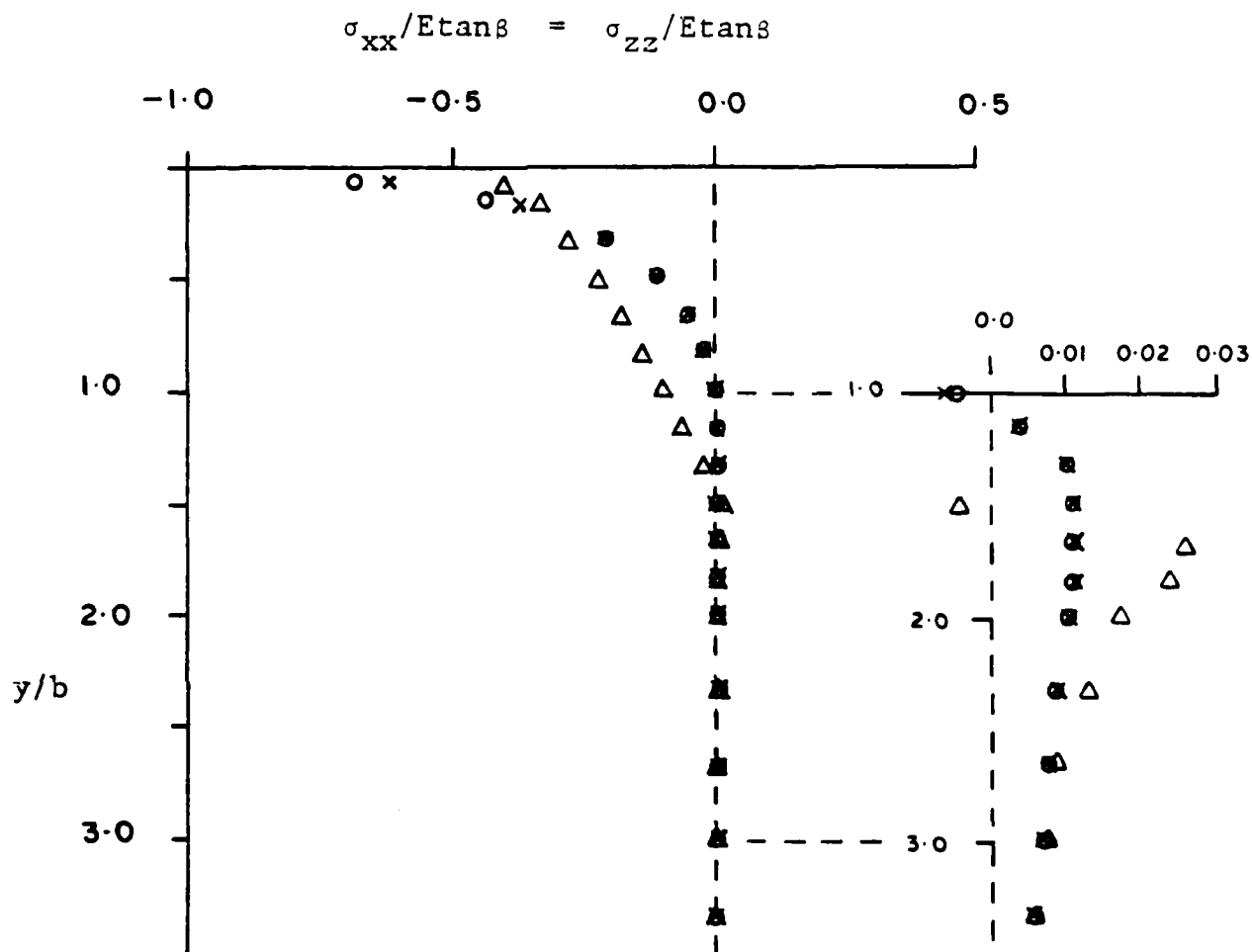


o = Sneddon Analysis

x = Elastic Finite Element Analysis

Δ = Elastic/Plastic Finite Element Analysis

Figure 18. Non-dimensionalized Surface Stress $\sigma_{zz}/E \tan \delta$ along the x-axis.

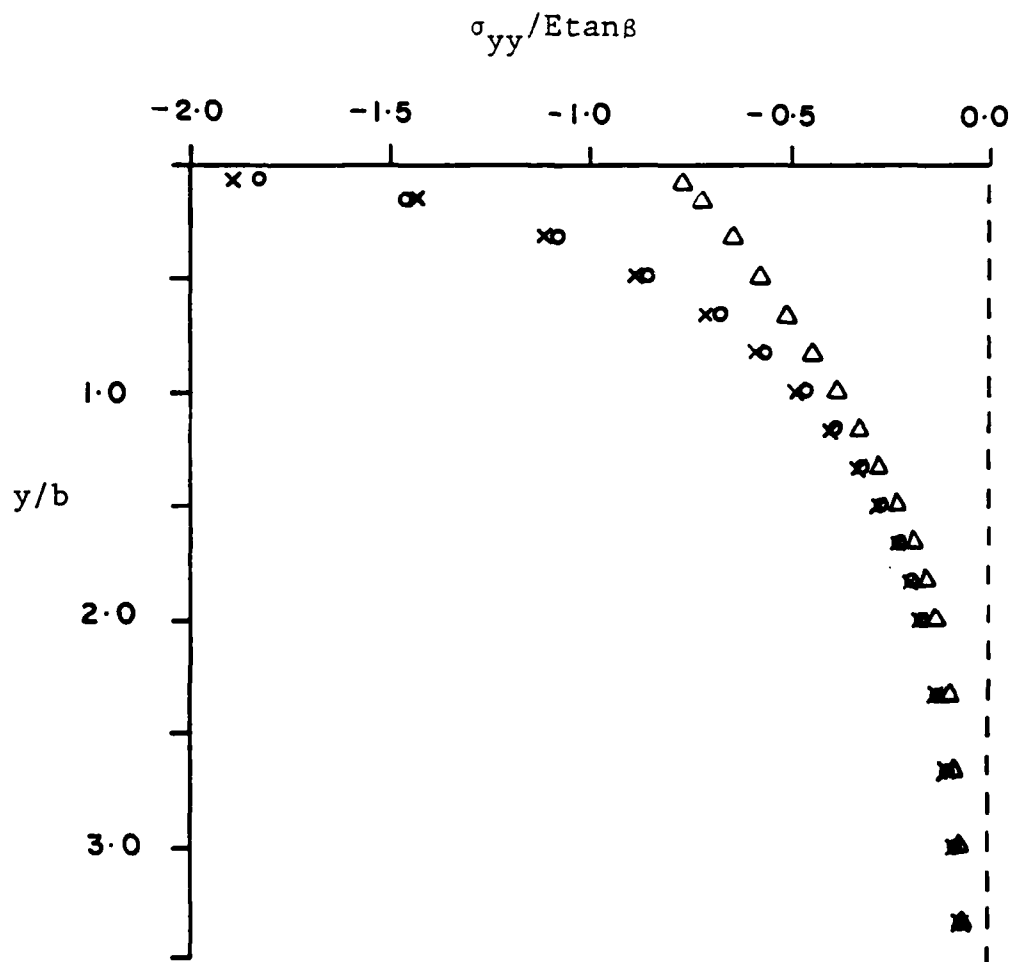


o = Sneddon Analysis

x = Elastic Finite Element Analysis

Δ = Elastic/Plastic Finite Element Analysis

Figure 19. Non-dimensionalized Subsurface Stress $\sigma_{xx}/E\alpha n\beta$ and $\sigma_{zz}/E\alpha n\beta$ along the y-axis.



o = Sneddon Analysis

x = Elastic Finite Element Analysis

Δ = Elastic/Plastic Finite Element Analysis

Figure 20. Non-dimensionalized Subsurface Stress $\sigma_{yy}/E\alpha n\beta$ along the y-axis.

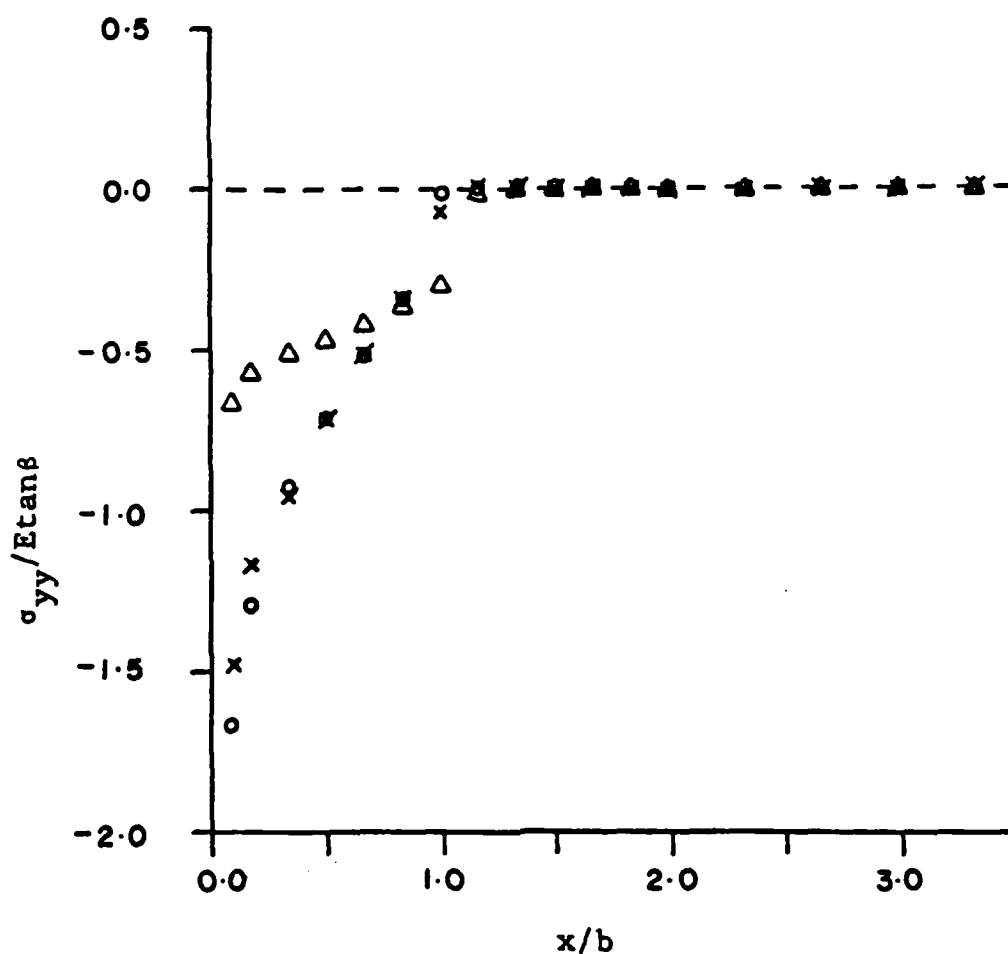
4.3.1 Elastic Conical Indentation

Considering initially the elastic conical indentation, it is obvious that excellent agreement is obtained between elastic stresses generated by the closed-form Sneddon solution and the elastic finite element analysis both on the surface of the half-space and directly beneath the conical indenter. Minor differences are found at the edge of contact ($x/b = 1.00$). These differences are caused by the inability of the finite element grid to actually express the high stress gradient in this region. Along the surface at the edge of contact, both the Sneddon solution and the elastic finite element analysis show a tensile peak in what will be termed the horizontal stress component, σ_{xx} , Figure 17. This peak, also found in spherical indentation, is usually associated with ring cracking and subsequent Hertzian cone cracking. This will be discussed further in a subsequent section. Within the contact zone, this stress becomes compressive, reaching a compressive maximum directly beneath the indenter. Outside the contact area, this stress decreases from the tensile peak to zero as distance increases from the contact surface. The out-of-plane hoop stress, σ_{zz} , along the surface is everywhere compressive, with the peak compressive value being found directly beneath the indenter, Figure 18. This stress also gradually decreases to zero as distance from the origin increases.

Directly beneath the indenter, the horizontal stress, σ_{xx} , Figure 19, changes from high compressive values at the surface to small tensile values at approximately one contact radius from the

surface. The highest tensile value is found at the point of $y/b = 1.60$. Beyond this point, this stress gradually decreases to zero. Tensile values of this stress result in median cracking, found beneath pyramidal and conical indenters. The subject of median cracking will be discussed in a subsequent section. The out-of-plane hoop stress, σ_{zz} , is of course equal to the horizontal stress, σ_{xx} , along this axis of symmetry. The subsurface vertical stress component, σ_{yy} , shown in Figure 20, is everywhere compressive; reaching a peak magnitude directly beneath the indenter and rapidly decreasing to zero at increased distance from the origin.

Figure 21 shows the pressure distribution, σ_{yy} , within and adjacent to the contact zone. Within the contact zone ($x/b \leq 1.00$) the classical pressure distribution expected beneath a conical indenter is obtained from the elastic finite element analysis for the prescribed displacement loading. As can be seen from the figure, this corresponds very well to that obtained from the closed-form Sneddon solution for elastic conical indentation. This verifies the displacement loading condition assumed in this investigation, where only vertical displacements of surface nodal points are specified. In addition, the load resultant predicted from the Sneddon solution (Appendix A), $F_s = 3004\text{N}$, compares well with that determined independently by summation of the vertical nodal forces on the contact surface of $0 \leq x/b \leq 1.00$, $F_f^e = 2943\text{N}$. This factor further substantiates the displacement method of load application.



Δ = Sneddon Analysis

\times = Elastic Finite Element Analysis

\circ = Elastic/Plastic Finite Element Analysis

Figure 21. Non-dimensionalized Pressure Distribution $\sigma_{yy}/E\epsilon\alpha\delta$ on and adjacent to the Contact Zone.

4.3.2 Elastic/Plastic Conical Indentation

In generating elastic/plastic stress states beneath the conical indenter, the model was allowed to yield according to the Huber-Mises yield criterion at nodal points beneath the indenter with subsequent flow being governed by the Prandtl-Reuss flow rule. The elastic/perfectly plastic stress-strain curve was assumed for soda-lime glass. During each iteration loop, both the elastic and elastic/plastic portions of the stiffness matrix were updated. As stated earlier, the vertical nodal point displacement along the contact surface was used as load input for an assumed contact radius of 0.30 mm. The elastic Sneddon solution was used to predict vertical displacements, thus raising an obvious question regarding the use of an elastic solution for the prediction of elastic/plastic displacements beneath the conical indenter.

The applicability of the elastic Sneddon solution for the prediction of vertical displacements on the contact surface was judged by observation of mesh deformation for the elastic/plastic case, and the extent and character of the plastic region. The mesh deformation for the elastic/plastic conical indentation is shown in Figure 22. The corresponding extent and character of the plastically deformed region and the stress trajectories beneath the indenter can be seen in Figure 23. These figures indicate a continuity of surface deformation both within and adjacent to the contact surface, and also plastic region characteristics similar to those measured experimentally and predicted analytically. The shape of the plastic zone obtained by

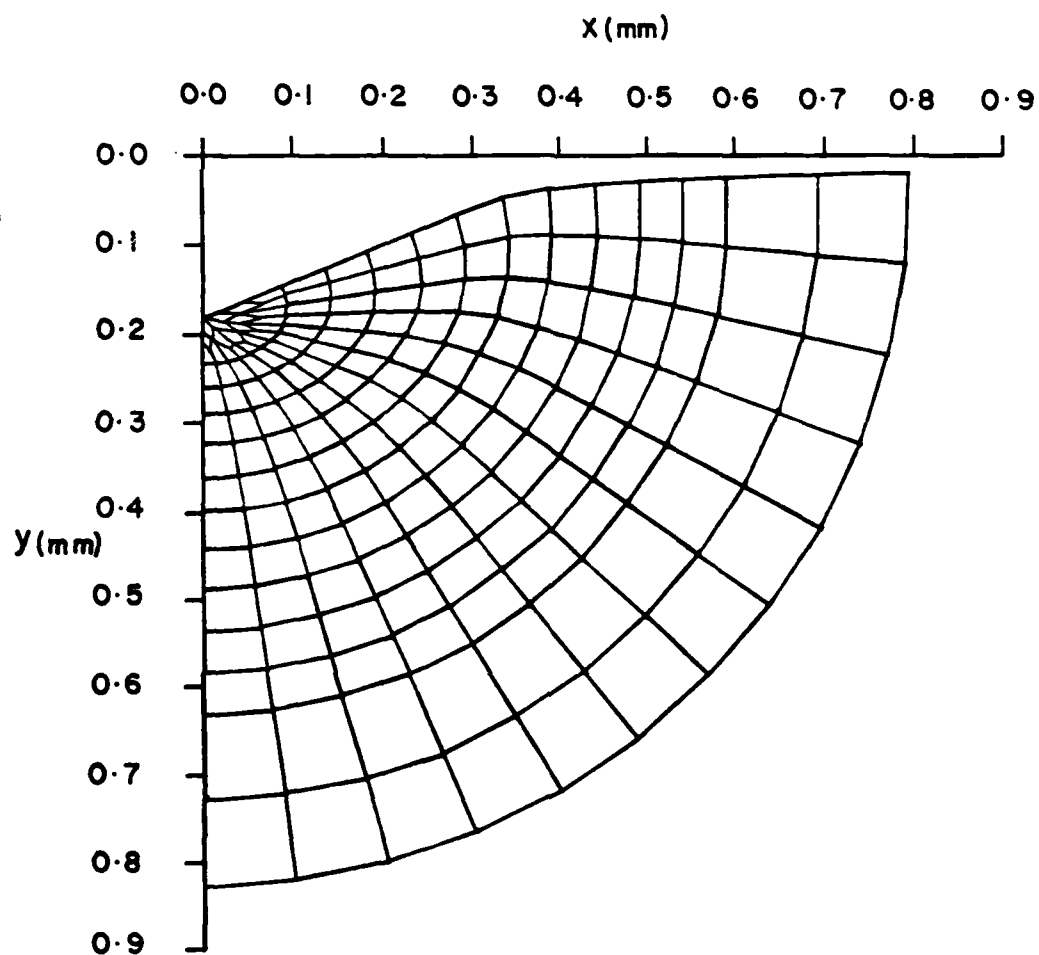


Figure 22. Elastic/Plastic Mesh Deformation.

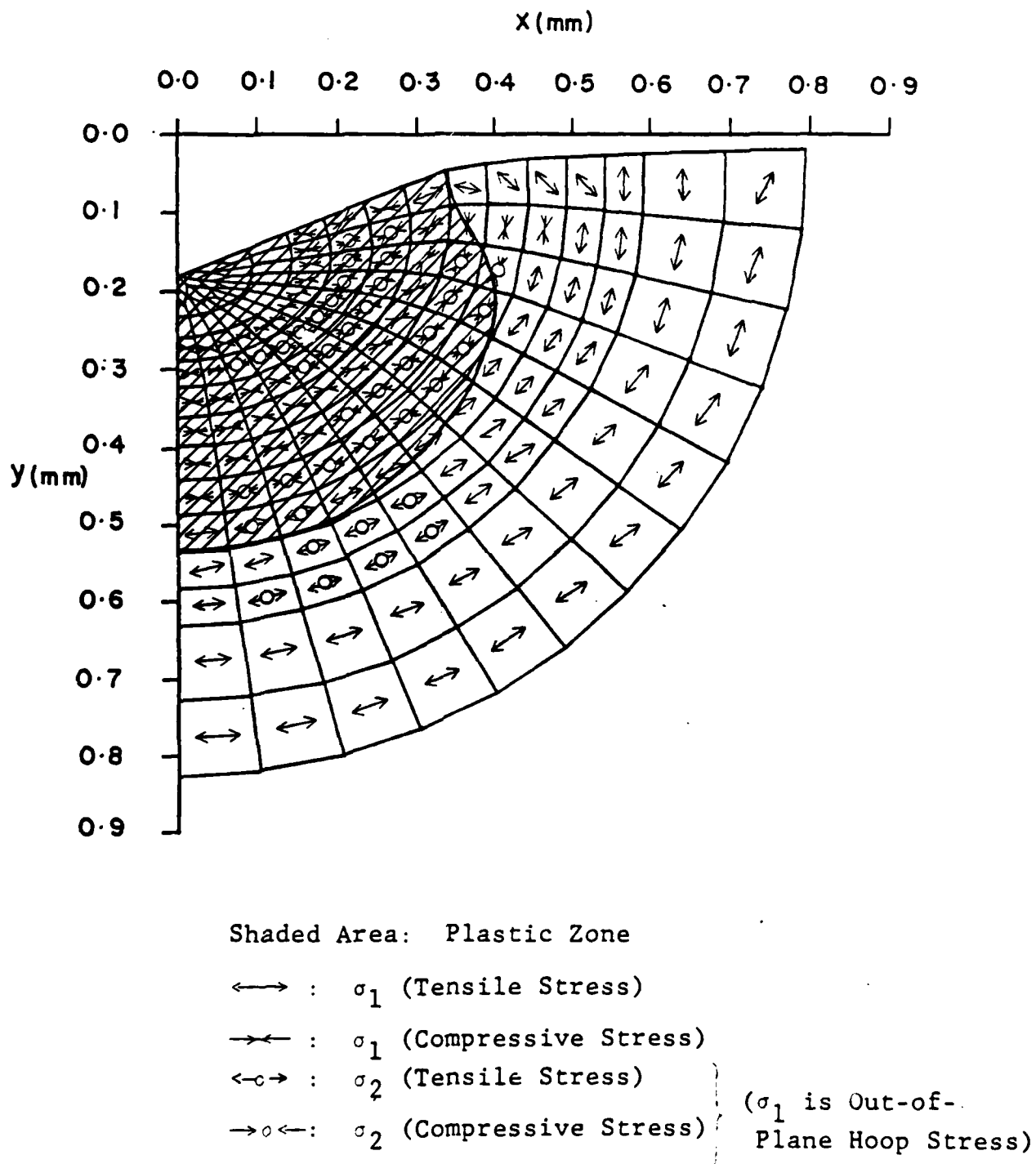


Figure 23. Plastic Zone and Elastic/Plastic Stress Trajectories.

the elastic/plastic finite element analysis is nearly hemispherical and is centered directly beneath the indenter. Its radius c is approximately 0.35 mm, resulting in a ratio of c/b equal to 1.16. This c/b ratio compares favorably with a value of 1.159 explicitly obtained by Johnson [11] (APPENDIX B) as a function of material properties, with the center of the plastic region at the undeformed origin. These factors were therefore considered as substantiation of the assumed displacement loading as obtained from the Sneddon solution. Observation of Figure 23 illustrates the difference in the principal stress trajectories of the elastic and plastic regions. In the elastic region, the in-plane hoop stress is the maximum principal stress, σ_1 , whereas in the plastic region, the out-of-plane hoop stress is mainly the maximum principal stress, σ_1 .

In figures 17 to 20, the elastic/plastic stress fields along the surface of the half-space are compared with the elastic solutions obtained from the finite element analysis and the Sneddon solution. The horizontal stress, σ_{xx} , along the surface shows the characteristic tensile peak at the elastic/plastic boundary as indicated in Figure 17. Within the contact zone, this stress is again compressive, reaching a compressive peak directly beneath the indenter. Outside the region of contact, this stress rapidly approaches the value obtained in the elastic analysis at the elastic/plastic boundary. This tensile peak is usually associated with ring cracking, as suggested in the previous section. The out-of-plane hoop stress, σ_{zz} , along the surface again is everywhere compressive, with the peak compression being found directly beneath the indenter, as indicated in Figure 18.

This stress does not rapidly approach elastic results with increasing distance from the contact region as was seen in the case of the horizontal stress, σ_{xx} .

Directly beneath the indenter, the horizontal stress, σ_{xx} , changes from high compressive values near the surface to small tensile values at the elastic/plastic boundary, as indicated in Figure 19. This stress rapidly approaches levels obtained in the elastic analysis near the elastic/plastic boundary. Tensile values of this stress result in median cracking as suggested in the previous section. The subsurface vertical stress component, σ_{yy} , is again everywhere compressive; reaching a peak magnitude directly beneath the indenter. It decreases to zero with increasing distance from the surface more rapidly than the corresponding stress in the elastic analysis. This is indicated in Figure 20.

In Figure 21, the elastic/plastic pressure distribution, σ_{yy} , within and adjacent to the contact zone is compared with the elastic solutions obtained from the finite element analysis and Sneddon solution. It is obvious that high pressure exists within the region of contact and that this pressure is, of course, suddenly reduced beyond the contact surface. The elastic/plastic load resultant generated from summation of the vertical nodal forces on the contact surface of $0 \leq x \leq b$ is obtained as $F_F^P = 2498\text{N}$. This is 15 to 17 percent lower than the elastic load resultants obtained from the Sneddon solution and the elastic finite element analysis. This lower load resultant value was expected, since less pressure was needed to deform the yielded region.

CHAPTER V

RESIDUAL SOLUTIONS FOR ELASTIC/PLASTIC CONICAL INDENTATION

5.1 Introduction

In this chapter, residual stress, displacement and strain fields resulting from the elastic/plastic conical indentation are generated. Development of the residual solution required that a load-unload cycle consisting of two separate loading stages (stage II and III) be formulated. During the loading stage of the cycle (stage II), equivalent nodal forces were applied as load input to surface nodes within the contact area. These equivalent nodal loads were obtained from the nodal force output obtained in stage I displacement loading and produce the surface deformation and resultant stress, displacement and strain distribution beneath the indenter. A procedure developed to convert the nodal force output obtained in stage I to the equivalent nodal load is discussed in greater detail in the following sections of this chapter. In the unloading stage of the cycle (stage III), the equivalent nodal loads were reduced to zero, resulting in the required residual solutions.

5.2 Method of Analysis

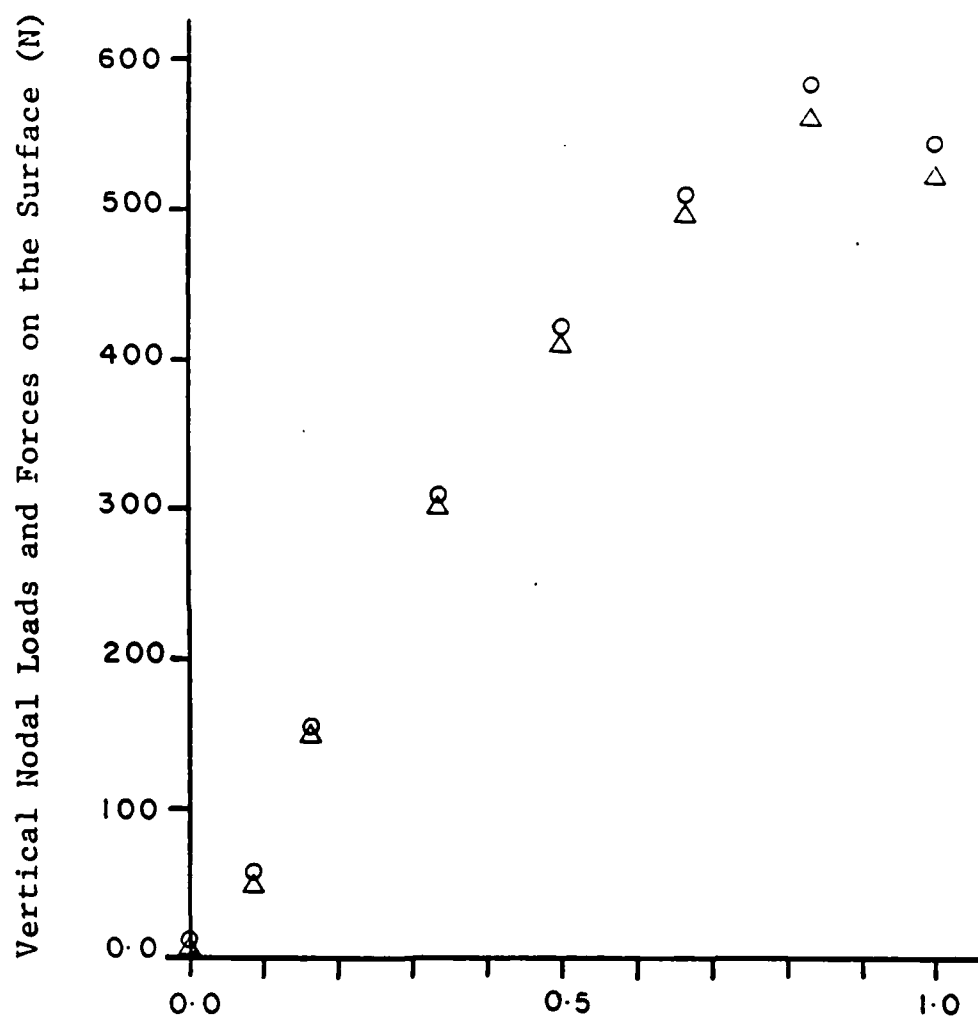
The procedure used to obtain the equivalent nodal loads in the contact area from the nodal force output obtained in stage I is discussed in this section. These equivalent nodal loads are, as mentioned previously, used during the loading stage of the cycle (stage II).

In order to improve stress and displacement fields beneath the indenter for stage II loading, an iterative scheme was developed through which the output nodal forces from stage I loading were continually improved by incrementing each nodal load magnitude until the error in resultant displacement and stress fields and nodal force resultants beneath the indenter was less than 3 percent. With the error reduced to less than 3 percent, the nodal force loading was considered to be equivalent to the nodal displacement loading. Figure 24 compares the nodal forces resulting from the displacement loading to the equivalent nodal loads obtained through the iterative scheme.

Following the equivalent nodal force loading in the loading phase of the cycle, the equivalent nodal loads were reduced to zero yielding residual displacements, strains and stresses on the contact surface and beneath the indentation.

5.3 Results and Discussion

A geometric comparison of the indentation profile obtained in the loading phase of the cycle and the residual surface crater remaining after unloading is shown in Figure 25. From Figure 25, the ratio of residual crater depth to maximum indentation depth, v_{\max}^R/v_{\max} , is easily obtained as 0.41. This ratio can be compared to that analytically predicted from the equation developed by Lawn and Howes [46] (APPENDIX B, equation (B-8)). The analytical ratio obtained is $v_{\max}^R/v_{\max} = 0.70$ for a hardness of soda-lime glass of 5.6 GPa and the assumption $\gamma_E \approx \gamma_H$, where γ_E and γ_H are elastic and plastic hysteresis geometrical parameters, respectively (APPENDIX B, equation (B-9)). The disagreement



Δ = Nodal Forces resulted by Indentation (Output of Stages I)

o = Equivalent Nodal Loads (Input for Stage II)

Figure 24. Comparison of Nodal Forces Resulting from Indentation and Equivalent Nodal Loads.

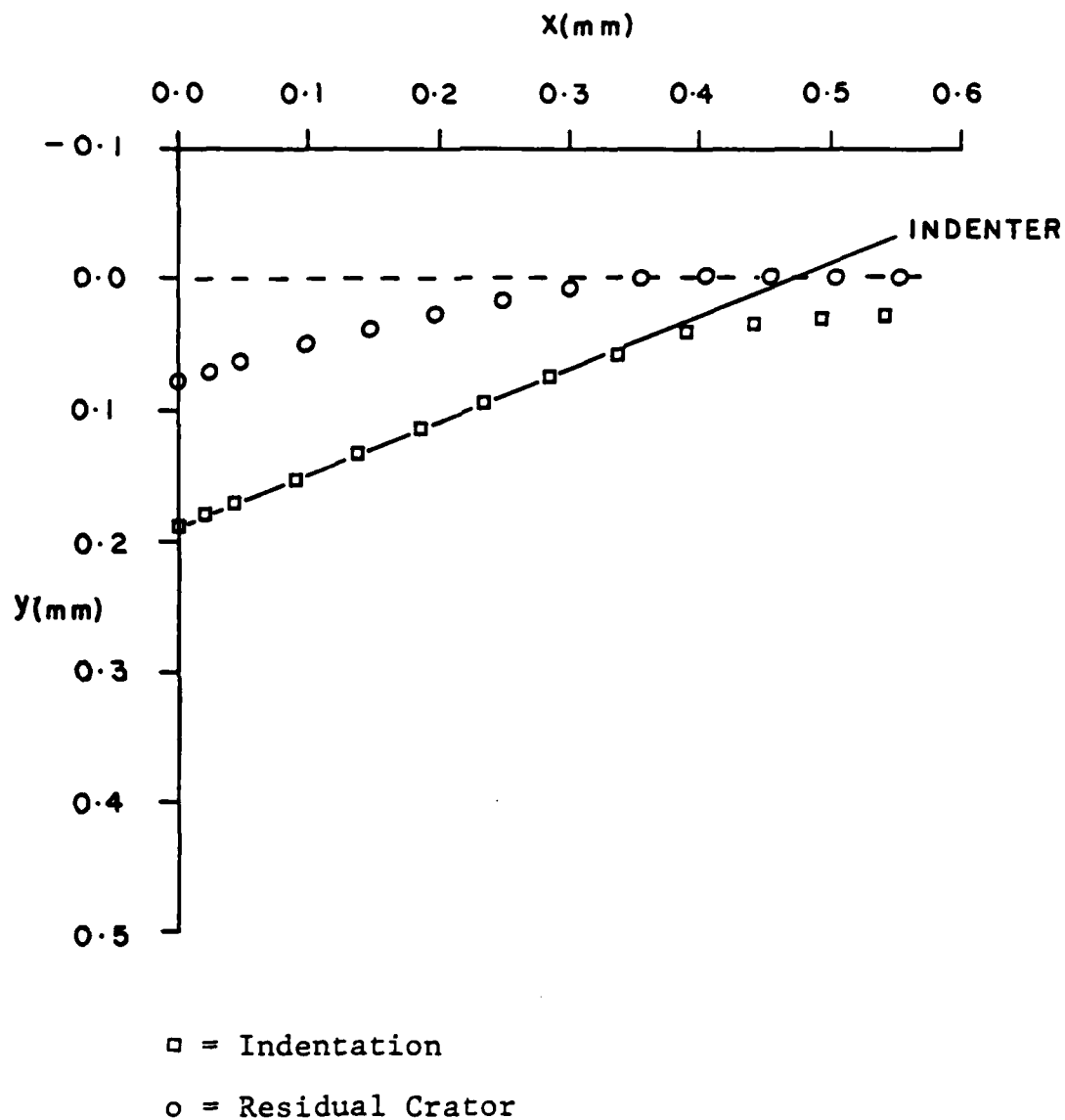


Figure 25. Geometrical Comparison of Indentation Profile and Residual Crater.

between the finite element and analytical results may be caused by the assumption $\gamma_E \approx \gamma_H$. By using the value of $v_{\max}^R / v_{\max} = 0.41$ predicted by the finite element solution and equation (B-8), a geometrical parameter ratio γ_E / γ_H of 1.26 is obtained resulting in a geometrical parameter for plastic hysteresis γ_H of 1.25. This result is based on an assumed elastic geometrical parameter $\gamma_E = \pi/2$ defined by Sneddon [5,6].

It should be noted that there is a pile-up on the free surface adjacent to the contact radius, as shown in Figure 25, and this pile-up is the result of elastic recovery of the surface elements adjacent to the contact area, Figure 26.

Non-dimensionalized horizontal and out-of-plane hoop residual stresses along the indentation surface are shown in Figure 27. Stresses are shown as a function of non-dimensionalized distance from the center of indentation. Both the horizontal and out-of-plane hoop stresses, σ_{xx}^R and σ_{zz}^R , are tensile for the regions $0.5 \leq x/b \leq 1.5$ and $x/b \geq 0.6$, respectively, with tensile peaks occurring at the elastic/plastic boundary $x/b \approx 1.3$. These tensile residual stresses may be responsible for the propagation of radial cracking during the unloading phase of the cycle, a topic of discussion in a subsequent chapter.

Non-dimensionalized residual stresses directly beneath the indenter are shown in Figure 28. The horizontal and out-of-plane hoop stress, σ_{xx}^R and σ_{zz}^R , as well as the vertical stress component, σ_{yy}^R , are tensile for $y/b \geq 1.5$. Tensile values of the out-of-plane hoop residual stress could result in median crack extension during the unloading phase. The vertical residual tensile stresses could promote lateral

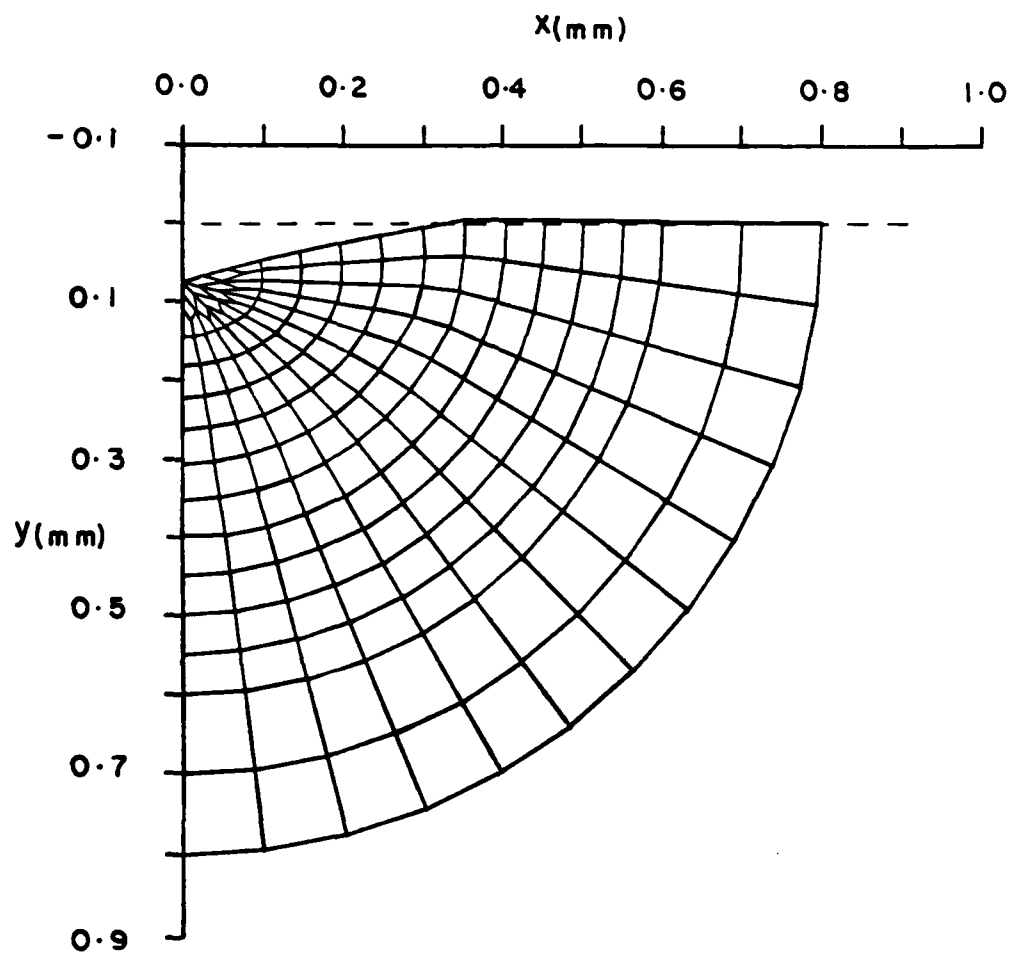
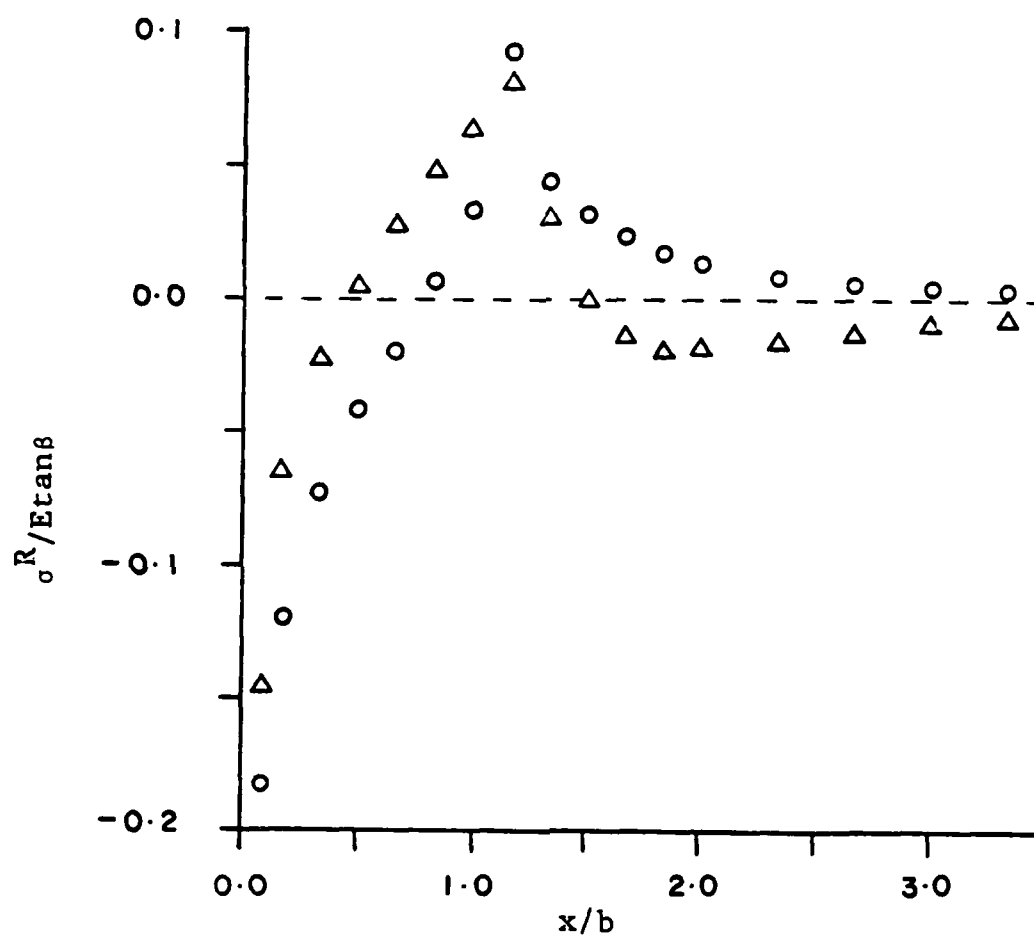


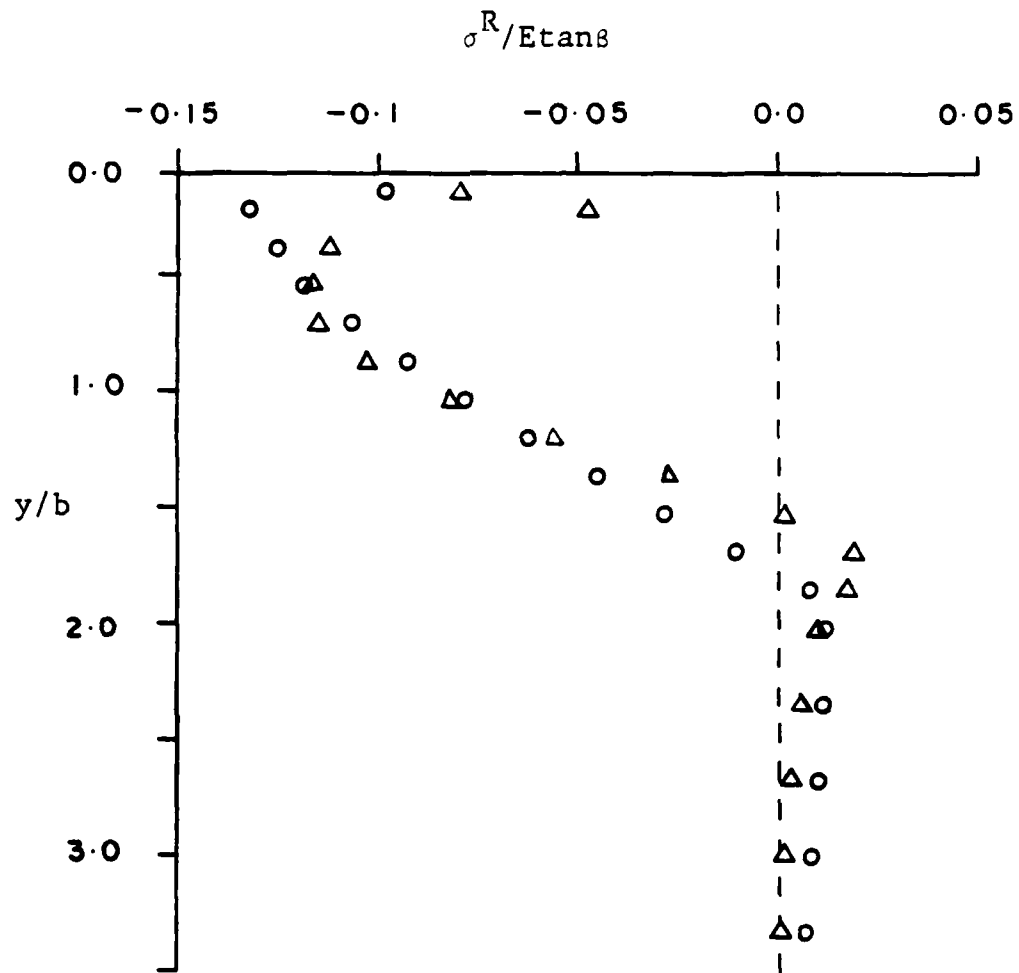
Figure 26. Elastic/Plastic Residual Mesh Deformation.



$$\Delta = \sigma_{xx}^R/E \tan \beta$$

$$\circ = \sigma_{zz}^R/E \tan \beta$$

Figure 27. Non-dimensionalized Residual Surface Stresses along the x-axis.



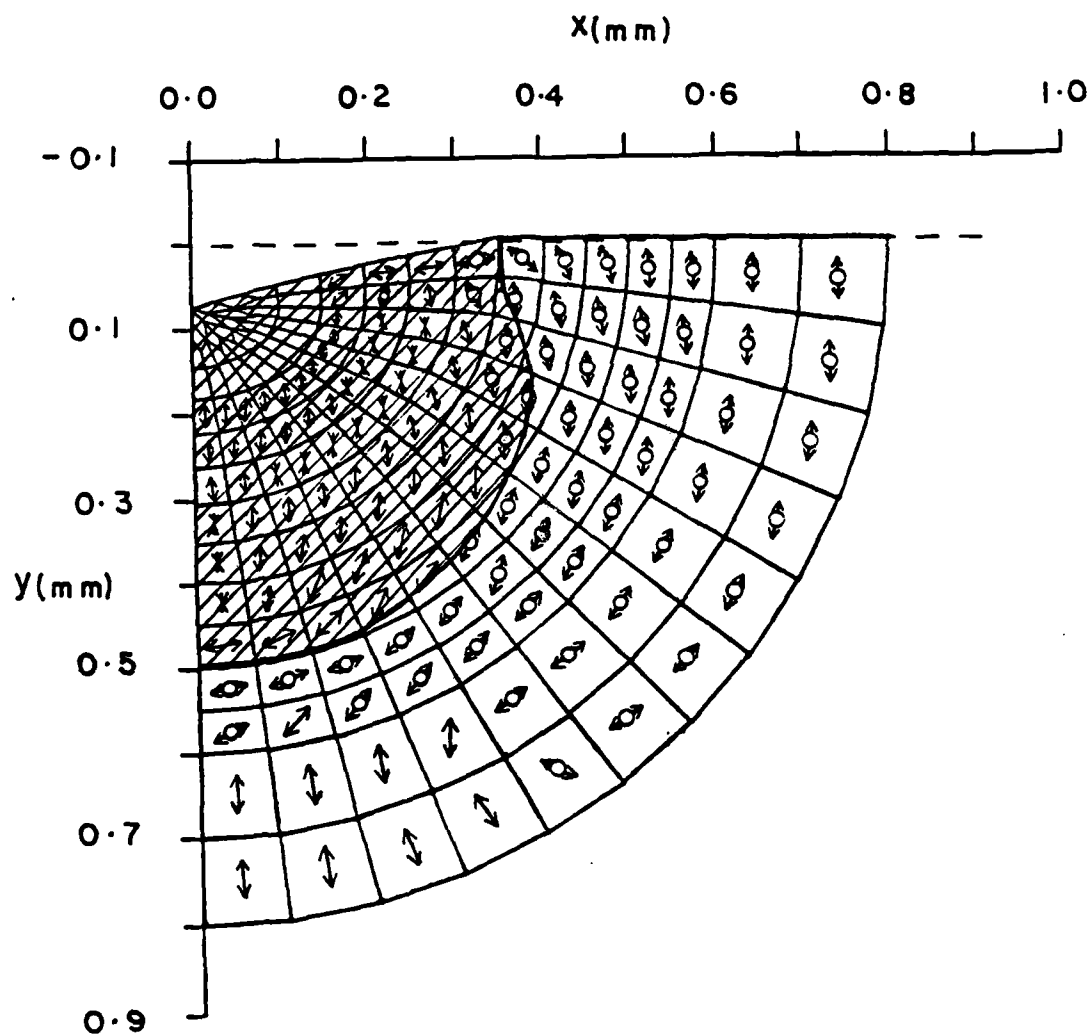
$$\Delta = \sigma_{xx}^R/E\epsilon\alpha\delta = \sigma_{zz}^R/E\epsilon\alpha\delta$$

$$\circ = \sigma_{yy}^R/E\epsilon\alpha\delta$$

Figure 28. Non-dimensionalized Residual Subsurface Stresses along the y-axis.

crack propagation upon unloading. Both of these possibilities will be explored in the following chapter.

The residual plastic zone and stress trajectories are shown in Figure 29. Comparison with Figure 23 reveals that the size of the plastic zone has increased approximately 20 percent during the unloading phase due to elastic recovery in the plastic region. Of major interest are the stress trajectories in the elastic region where fracture can be extended during the unloading phase. In this region the stress trajectories indicate the possible propagation of the lateral cracking driven by the in-plane hoop stress, σ_2^R , from points near the elastic/plastic boundary. Near the surface, the trajectories indicate that the out-of-plane hoop residual stress, $\sigma_{zz}^R = \sigma_1^R$, would result in the radial crack extension. For subsurface regions, the trajectories indicate the possibility of the median crack propagation by the out-of-plane hoop residual stress, σ_{zz}^R .



Shaded Area: Plastic Zone

\longleftrightarrow : σ_1^R (Tensile Stress) \longleftrightarrow : σ_2^R (Tensile Stress) (σ_1^R is Out-of-Plane Stress)
 $\longrightarrow \circ \longleftarrow$: σ_1^R (Compressive Stress) $\longrightarrow \circ \longleftarrow$: σ_2^R (Compressive Stress)

Figure 29. Plastic Zone and Residual Stress Trajectories.

CHAPTER VI

ANALYSIS OF FRACTURE MECHANISMS INDUCED BY INDENTATION

6.1 Introduction

Analytical and experimental investigations considering the mechanics of crack initiation and propagation beneath spherical, conical, Vickers pyramidal, and point indentations in a variety of materials have been the topic of many recent investigations [29-48]. In this chapter, fracture mechanisms beneath conical indentation in soda-lime glass are further described by applying the numerical results obtained in the preceding chapters to approximate fracture mechanics theories. Conical indentation was chosen for analysis as it closely simulates loading conditions found in a large variety of machining processes.

6.2 Failure Modes beneath the Indenter

There are four major crack systems introduced as indentation fracture mechanisms. These crack systems can be classified by the cracks initiated and propagated near the surface and at subsurface locations. It has also been experimentally and analytically shown that these crack systems are initiated on or near the elastic/plastic boundary with subsequent extension into the elastic region. The schematic diagram of these crack systems is shown in Figure 30.

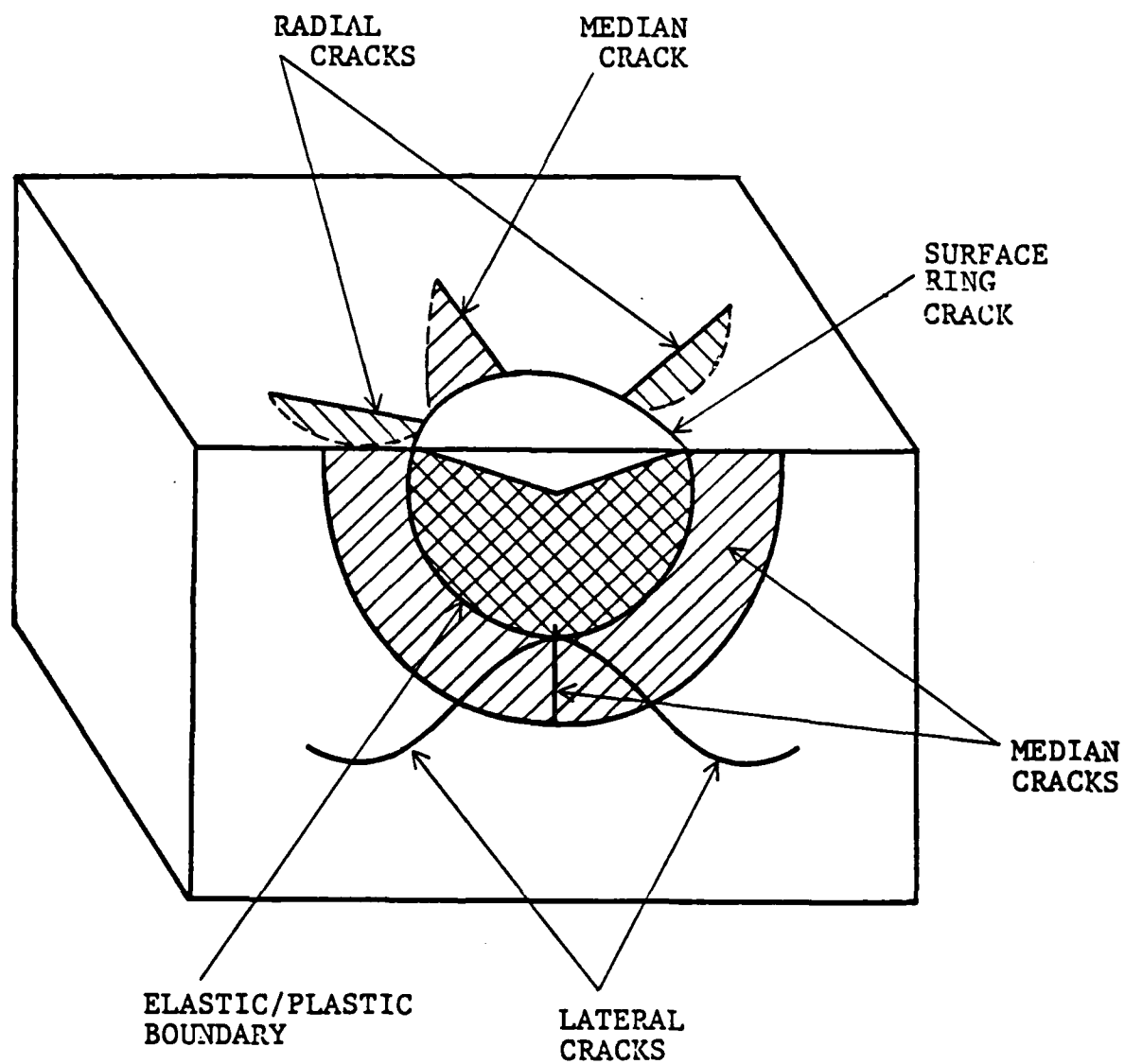


Figure 30. Schematic Diagram of Indentation Cracks.

6.2.1 Crack Systems near the Surface

Near the surface, two major crack systems are usually found in axisymmetric indentation. They are surface ring crack system which is initiated in the loading phase of the cycle [35,36], and radial crack system which is usually initiated and propagated during the unloading phase of the cycle [33,35,36]. It is known that surface ring crack system is often propagated as a Hertzian cone crack [31,35,37,40] in the case of spherical indentation. In the case of Vickers pyramidal indentation, radial crack system is often initiated in the loading phase and propagated during the unloading phase of the cycle, since the edges of pyramidal indenter create highly singular regions in the specimen [33,36,41,42].

6.2.2 Subsurface Crack System

Two major subsurface crack systems are also found. They are median crack system, which is initiated and propagated during the loading phase and further propagated during the unloading phase of the cycle [33,35,36,38], and lateral crack system, which is usually initiated and propagated during the unloading phase of the cycle. It is known that the shape of the median cracking is penny-like or half-penny-like [33,34,36,38,39,43] beneath the indentation. Lateral crack system is often initiated with the surface ring crack and propagated as a Hertzian cone crack in the case of spherical indentation [31,35,37,40] as described in the last section. In the case of Vickers pyramidal indentation, lateral crack system is initiated on the elastic/plastic boundary and propagated to the surface [33,35,37,38,41].

6.3 Fracture Initiation and Propagation

In the discussion of fracture initiation and propagation during elastic/plastic conical indentation, only the opening mode (K_I -mode) was considered. To correlate the stresses numerically obtained by the finite element method with opening mode fracture, the tensile peak stresses at the surface and at subsurface locations must be considered, especially near the elastic/plastic boundary.

6.3.1 Identification of the Tensile Peak Stresses

The necessary tensile stress fields and tensile stress trajectories for loading and unloading of a conical indenter were numerically determined in the preceding chapters. By observation of Figures 17 and 27, the maximum surface tensile stresses are found at the elastic/plastic boundary. In the loading phase, the maximum value of the horizontal surface stress, σ_{xx} , corresponding to surface ring cracking, is obtained as 2.2 GPa. During the unloading phase, the maximum values of the horizontal surface residual stress, σ_{xx}^R , corresponding to the surface ring cracking, and the surface out-of-plane residual hoop stress, σ_{zz}^R , corresponding to radial cracking, are obtained as 1.6 GPa and 1.8 GPa, respectively. By observation of Figures 19 and 28, the maximum subsurface tensile stresses along the y-axis are also found at the elastic/plastic boundary. In the loading phase, the maximum value of the subsurface horizontal stress, σ_{xx} , which is equal to the subsurface out-of-plane hoop stress, σ_{zz} , corresponding to the median cracking, is obtained as 0.48 GPa. During the unloading phase of the cycle, the maximum values of the subsurface

horizontal residual stress, $\sigma_{xx}^R = \sigma_{zz}^R$, corresponding to the median cracking, and the subsurface vertical residual stress, σ_{yy}^R , corresponding to the lateral cracking, are obtained as 0.42 GPa and 0.24 GPa, respectively. Those tensile peak stresses are shown in Table 1 with the corresponding crack systems which they initiate.

6.3.2 Critical Flaw Size

The peak tensile stresses obtained in the previous section can be combined with an appropriate fracture mechanics theory to predict fracture initiation and propagation beneath the indenter. Crack initiation is here predicted by the Griffith flaw hypothesis [29,30]:

$$\sigma \geq (2E\Gamma/\pi c_f)^{\frac{1}{2}}, \quad (6.1)$$

where σ is the critical stress causing stable fracture, E is Young's modulus, Γ is the crack surface energy and c_f is the flaw size. By solving equation (6.1) for c_f , the following expression is obtained for the critical flaw size corresponding to the tensile peak stress:

$$c_f \geq (2E\Gamma/\pi\sigma^2). \quad (6.2)$$

On the surface, the critical flaw sizes corresponding to the horizontal tensile peak stress, 2.2 GPa, and the horizontal residual peak stress, 1.6 GPa, are obtained from equation (6.2) as 0.025 μm and 0.048 μm , respectively. These critical flaw sizes will result in initiation and propagation of the surface ring cracking. Also on the surface, the critical flaw size corresponding to the out-of-plane hoop residual tensile peak stress, 1.8 GPa, can be calculated as 0.039 μm which will result in initiation and propagation of the median cracking.

Table 1. Tensile Peak Stresses and the Corresponding Crack Systems

Loading Phase			Unloading Phase		
	Tensile Peak Stress (GPa)	Crack System	Tensile Peak Stress (GPa)	Crack System	
Surface	σ_{xx}	2.2 (σ_1)	1.6 (σ_2)	Ring Crack	Ring Crack
	σ_{yy}	--	--	--	--
	σ_{zz}	--	1.8 (σ_1)	Radial Crack	Radial Crack
Sub-Surface	σ_{xx}	0.48 (σ_1)	0.42 (σ_1)	Median Crack	Median Crack
	σ_{yy}	--	0.24 (σ_3)	--	Lateral Crack
	σ_{zz}	0.48 (σ_1)	0.42 (σ_1)	Median Crack	Median Crack

At subsurface locations along the y-axis, the critical flaw sizes corresponding to the horizontal or out-of-plane hoop tensile peak stress, 0.48 GPa, and the horizontal or out-of-plane hoop residual tensile peak stress, 0.42 GPa, are obtained from equation (6.2) as 0.54 μm and 0.7 μm , respectively. These critical flaw sizes will result in initiation and propagation of median crack system. Also at subsurface locations along the y-axis, the critical flaw size corresponding to the vertical residual tensile peak stress, 0.24 GPa, can be obtained as 2.17 μm , which will result in initiation and propagation of lateral crack system.

The critical flaw sizes have been discussed in recent papers. Lawn and Evans [36] have given the critical condition for the initiation of subsurface flaws as:

$$c_f = 44.2 (K_{IC}/H)^2 \quad (6.3)$$

Hagan [43,44] has developed a similar expression for the largest flaw size which could be nucleated by the intersecting flow lines beneath the indenter:

$$c_f = 2.95 (K_{IC}/H)^2 \quad (6.4)$$

In these equations, K_{IC} and H are the critical stress intensity factor and hardness, respectively. For values of $K_{IC} = 0.7 \text{ MNm}^{-3/2}$ and $H = 5.6 \text{ GPa}$ for soda-lime glass, equations (6.3) and (6.4) predicted critical flaw sizes of 0.7 μm and 0.46 μm , respectively. The void size for soda-lime glass has been experimentally measured by Hagan [44] as 0.6 μm . These flaw sizes were correlated to the median cracking. Swain and Hagan [35] and Chiang, Marshall and Evans [47] correlated

the crack systems and the threshold flaw sizes. The threshold flaw sizes for median and radial crack systems were estimated as 1.0 μm and that for lateral crack system was estimated as 3.0 μm . All of those critical flaw sizes are compared in Table 2. The critical flaw size obtained by the finite element analysis with the Griffith energy hypothesis agrees very well with experimental and analytical values for median crack system. However the critical flaw sizes obtained by Swain et al. and Chiang et al. are clearly overestimated as compared with other analytical, experimental and numerical values for crack initiation.

6.3.3 Fracture Initiation and Propagation Zones

As described previously, the critical flaw sizes required for the initiation and propagation of the various crack systems are obtained from the Griffith energy hypothesis with the stresses generated by the finite element method. It was, then, found that the critical flaw sizes predicted by Swain et al. and Chian et al. were overestimated when compared with the critical flaw sizes obtained in this investigation.

However, by use of these overestimated flaw sizes, the critical stresses can be generated by equation (6.1) to predict probable crack initiation and propagation zones. The values of the critical stress corresponding to initiation and propagation of the median and radial crack systems is obtained as 0.35 GPa from equation (6.1) with the value of $c_f = 1.0 \mu\text{m}$. Also the value of the critical stress corresponding to lateral crack system can be obtained as 0.2 GPa from

Table 2. Threshold Flaw Sizes for the Initiation of Each Crack System

	FEM (Loading)	FEM (Unloading)	Lawn and Evans	Hagan	Swain and Chiang
Surface Ring Crack	0.025 (μm)	0.048 (μm)	--	--	--
Radial Crack	--	0.039 (μm)	--	--	1.0 (μm)
Median Crack	0.54 (μm)	0.70 (μm)	0.70 (μm)	0.46 (μm) 0.60	1.0 (μm)
Lateral Crack	--	2.17 (μm)	--	--	3.0 (μm)

equation (6.1) with the value of $c_f = 3.0 \mu\text{m}$. These two critical stress values can be compared with the stresses generated by the finite element analysis. In Figure 31, the assumed crack initiation and propagation zones corresponding to $\sigma \geq 0.35 \text{ GPa}$ in the loading phase are plotted. Those can be thought of as the assumed surface ring crack zone and the assumed median crack zone. In Figure 32, the assumed crack initiation and propagation zones corresponding to $\sigma \geq 0.35 \text{ GPa}$ and $\sigma_1 \geq 0.2 \text{ GPa}$ during the unloading phase of the cycle are plotted. Those can be thought of as the potential median crack, radial crack and lateral crack zones.

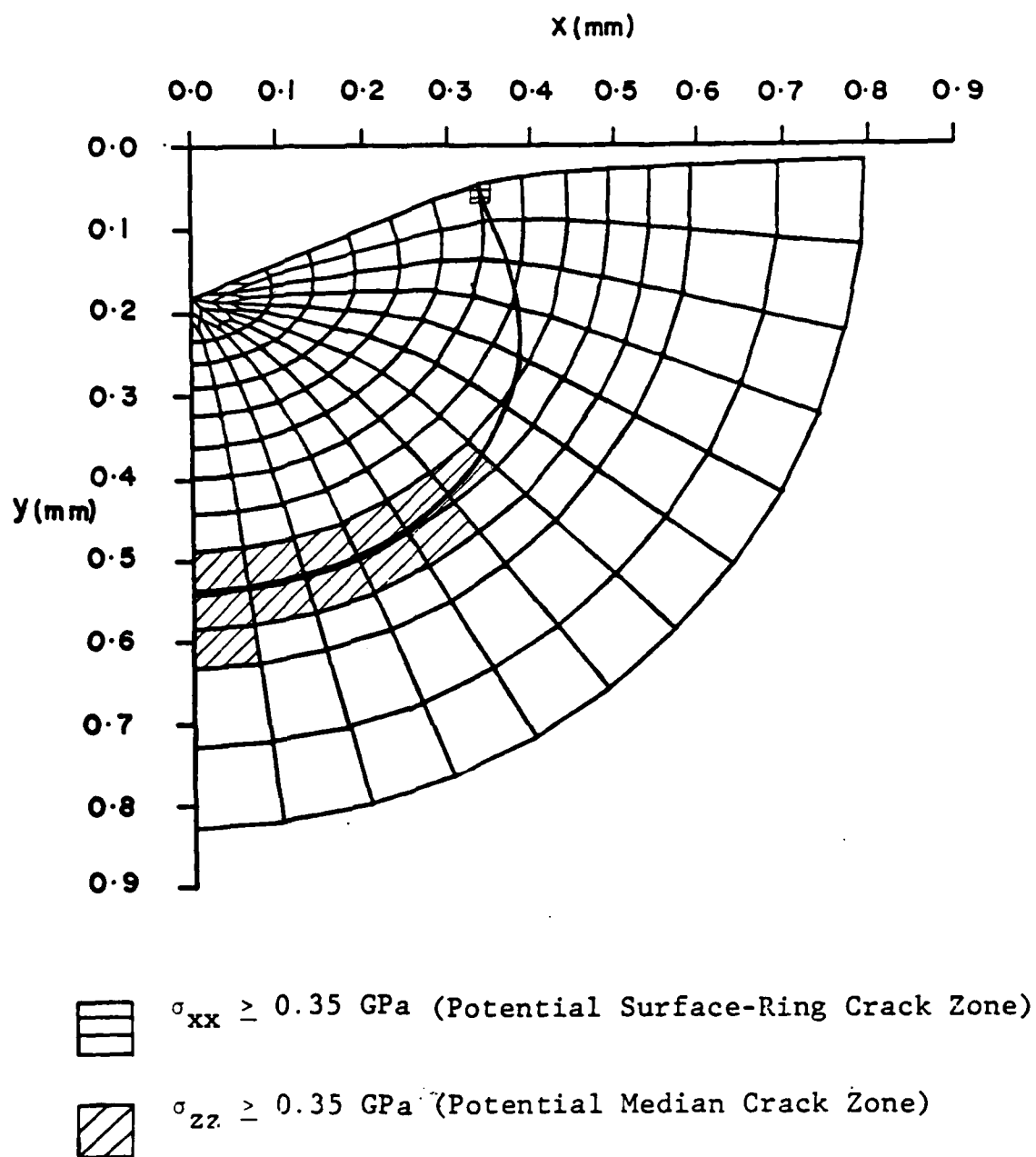


Figure 31. Crack Initiation and Propagation Zones in the Loading Phase

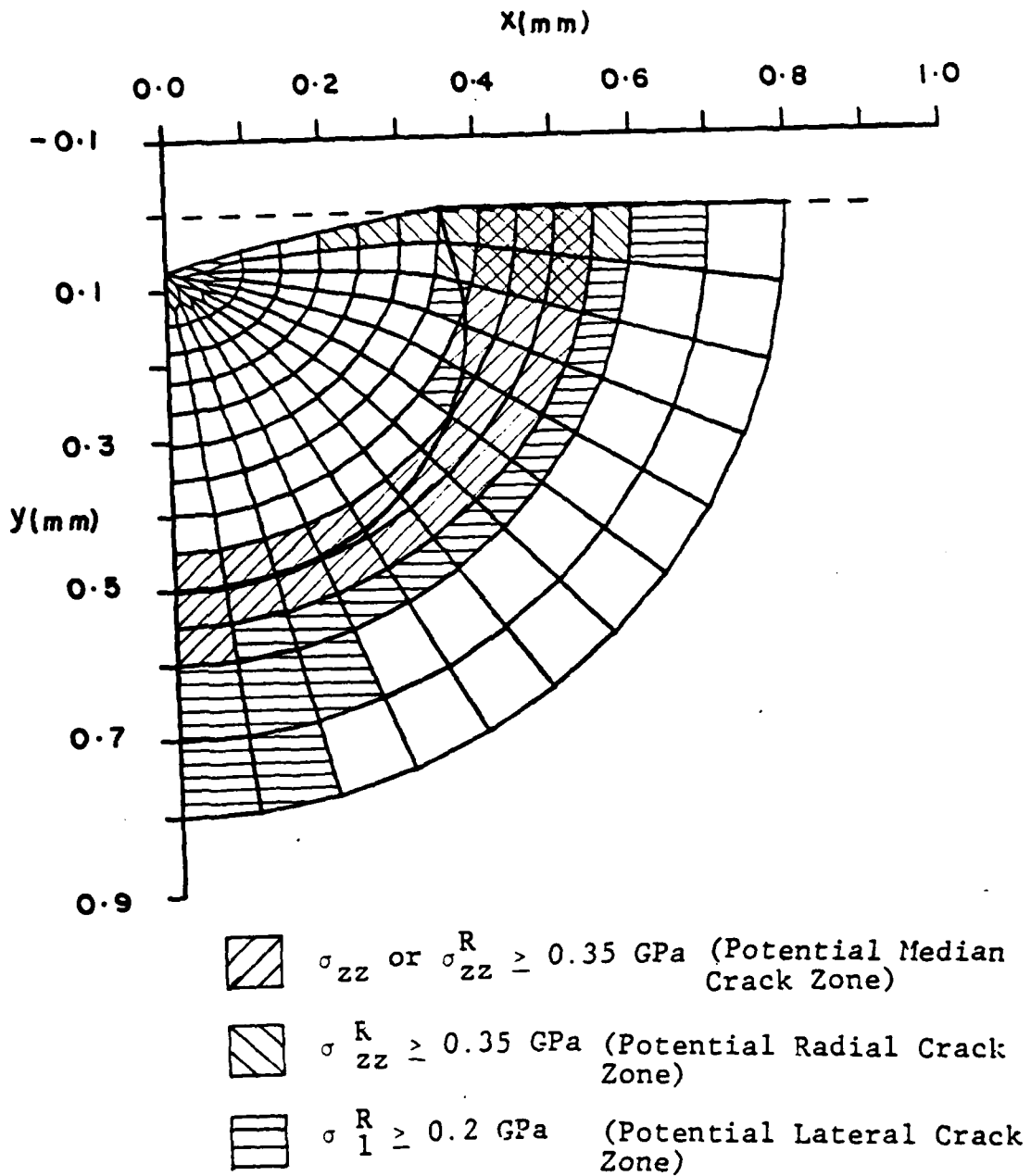


Figure 32. Crack Initiation and Propagation Zones during the Unloading Phase.

CHAPTER VII

CONCLUSIONS AND RECOMMENDATIONS

7.1 Conclusions

The following conclusions were reached in this investigation:

1. The elastic/plastic finite element code used in this investigation was verified by comparing nodal displacements, forces and plastic zone extension obtained for selected plane-stress problems, the plates with a circular penetration, with results numerically obtained by Yamada [Personal Note] and Marcal and King [18] in independent investigations.
2. The solution technique was further verified by comparison of elastic displacements, strains and stresses generated for conical indentation of an elastic half-space to the closed-form results obtained from the Sneddon solution.
3. The elastic/perfectly plastic finite element model developed for conical indentation of a half-space was successfully utilized to determine the size and characteristics of the plastic zone beneath the indenter during a loading-unloading cycle. The size of the plastic zone was shown to agree well with results obtained analytically by Johnson [11]. The shape of the plastic zone was shown to be hemispherical which conformed to results obtained in previous experimental

and analytical investigations. The origin of the hemispherical plastic zone was found to be on the deformed surface directly beneath the indenter, not on the undeformed surface.

4. The displacement, strain and stress fields were successfully generated by the elastic/plastic finite element model for a loading-unloading cycle. Resulting loading and residual stress fields were examined to determine the location and magnitude of tensile peak stresses which would result in the initiation and subsequent propagation of the ring, radial, median and lateral crack systems. Tensile peak stresses were characteristically found on the elastic/plastic boundary near the surface and at subsurface locations directly beneath the indentation. The out-of-plane hoop stress, which controlled both radial and median cracking, was found to change sign near the surface from compression during the loading phase to tension during the unloading phase of the cycle. This indicates that radial crack propagation and the additional median crack propagation takes place during the unloading phase, a fact experimentally verified.
5. By use of the Griffith energy hypothesis with the generated tensile peak stresses, the critical flaw sizes, resulting in initiation of the crack systems, were obtained. The critical flaw sizes obtained in this investigation agreed well with

critical flaw sizes predicted analytically and experimentally by Lawn et al. [36], Hagan [43,44], Swain et al. [35] and Chiang et al. [47] for each crack system.

6. Fracture initiation and propagation zones for the loading phase and unloading phase of the cycle were generated through comparison of the tensile peak stresses obtained in this investigation to critical stresses obtained from the Griffith energy hypothesis and maximum allowable flaw sizes. These fracture initiation and propagation zones agreed well with actual initiation and propagation zones experimentally observed.

7.2 Recommendations

The following subjects are recommended as topics for further research:

1. The elastic/plastic finite element model should be expanded to consider elastic/plastic strain hardening in order to analyze more realistic indentation models.
2. Investigation should be expanded to consider more brittle, lower yield strength/Young's modulus ratio models such as MgO and ZnS in order to determine the effect of these parameters on the extent and character of the plastic zone and resultant crack systems.
3. Shear peaks as well as tensile peaks should be investigated as they affect fracture initiation through dislocation activity and crack propagation by Mode II loading.

4. The elastic/plastic finite element model should be expanded to consider non-axisymmetric indentation such as Vickers pyramidal indentation and obtain characteristics of the singularities created by the edges of the indenter.
5. The elastic/plastic finite element technique should be combined with statistical analysis, such as "The Monte Carlo method", in order to closely model elastic/plastic indentation fracture.

APPENDIX A

THE ELASTIC STRESS FIELDS FOR POINT, SPHERICAL AND CONICAL INDENTATION

1. Point Indentation (Boussinesque and Michell Solution)

The well known non-dimensionalized stress field equations for the point indentation problem [2] are given for the coordinate system shown in Figure 33 as:

$$\left. \begin{aligned} \frac{\sigma_r}{p'} &= \frac{1}{2(\lambda+\mu)} \{- (3\lambda + 4\mu)\cos\theta + \mu\} \\ \frac{\sigma_\theta}{p'} &= \frac{\mu}{4(\lambda+\mu)} \cos^2\theta \sec^2 \frac{\theta}{2}, \\ \frac{\sigma_\phi}{p'} &= \frac{\mu}{4(\lambda+\mu)} (\cos\theta - \sin^2\theta) \sec^2 \frac{\theta}{2}, \\ \frac{\tau_{r\theta}}{p'} &= \frac{\mu}{4(\lambda+\mu)} \sin\theta \cos\theta \sec^2 \frac{\theta}{2}, \end{aligned} \right\} \quad (A-1)$$

$$\tau_{r\phi} = \tau_{\theta\phi} = 0,$$

where

$$\lambda = \frac{E}{(1+\nu)(1-2\nu)},$$

$$\mu = \frac{E}{2(1+\nu)}$$

$$p' = \frac{F}{\pi r^2}$$

$$F = \text{applied load}$$

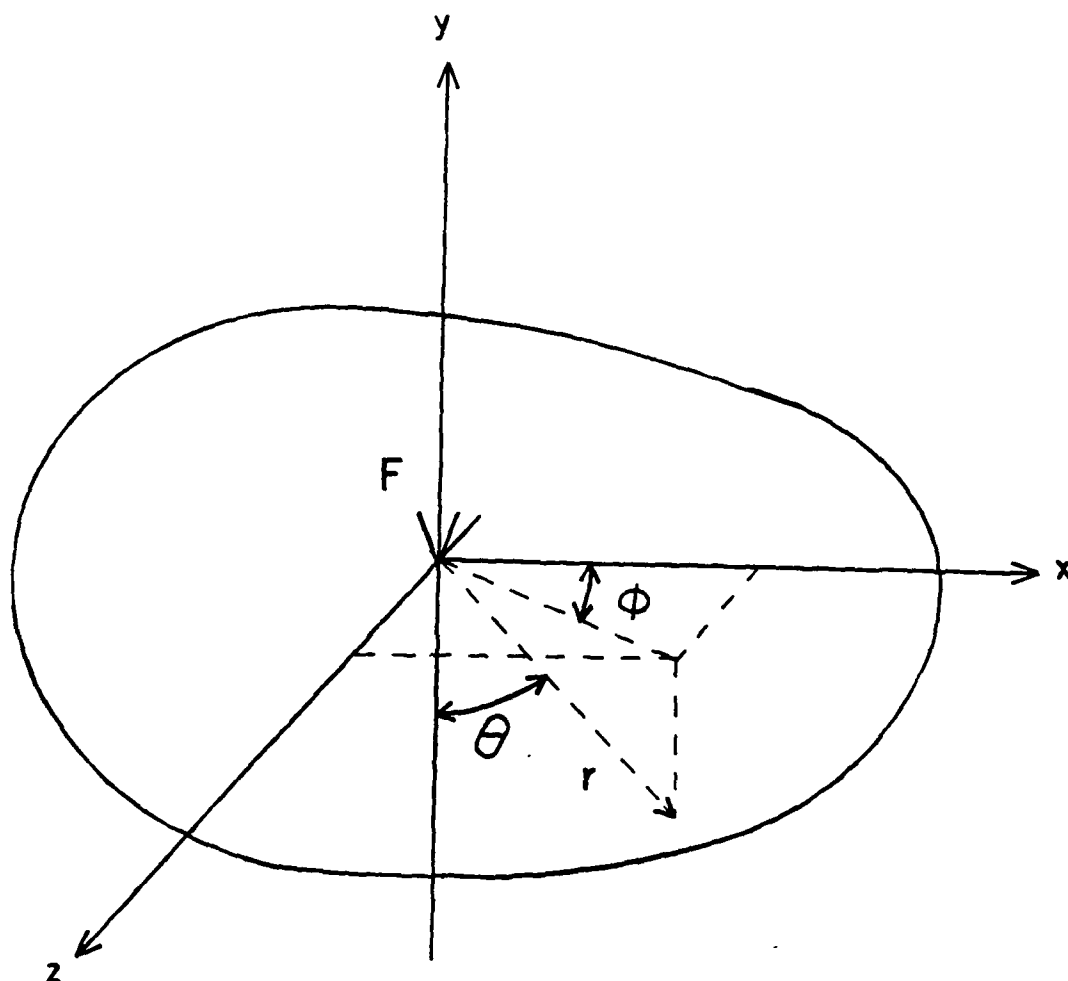


Figure 33. Point Indentation Geometry.

2. Spherical Indentation (Hertz and Huber Solution)

The non-dimensionalized Hertzian stress field which was extended to a general three-dimensional form by Huber [4] is expressed by four sets of equations depending on the coordinates of the point in the half-space, Figure 34.

For points along the y-axis directly beneath the indenter ($R=0(x=0, z=0)$):

$$\left. \begin{aligned} \frac{\sigma_x}{p_0} \Big|_{R=0} &= \frac{\sigma_z}{p_0} \Big|_{R=0} = -1.5(1+\nu) \left[1 - \frac{y}{a} \arctan \frac{a}{y} \right] - \frac{1}{2} \frac{a^2}{a^2+y^2} \Big|_{R=0}, \\ \frac{\sigma_y}{p_0} \Big|_{R=0} &= -1.5 \frac{a^2}{a^2+y^2} \Big|_{R=0}, \\ \tau_{xy} \Big|_{R=0} &= \tau_{yz} \Big|_{R=0} = \tau_{zx} \Big|_{R=0} = 0. \end{aligned} \right\} \quad (A-2)$$

For points on the surface of the half-space beneath the contact surface of the indenter ($y=0, R \leq a$):

$$\left. \begin{aligned} \frac{\sigma_x}{p_0} \Big|_{y=0} &= \frac{1-2\nu}{2} \frac{a^2}{R^2} \left[1 - \left(\frac{1}{a} \sqrt{a^2-R^2} \right)^3 \right] - \frac{1.5}{a} \sqrt{a^2-R^2}, \\ \frac{\sigma_y}{p_0} \Big|_{y=0} &= -1.5 \frac{\sqrt{a^2-R^2}}{a}, \\ \frac{\sigma_z}{p_0} \Big|_{y=0} &= \frac{2\nu-1}{2} \frac{a^2}{R^2} \left[1 - \left(\frac{1}{a} \sqrt{a^2-R^2} \right)^3 \right] - \frac{1.5}{a} \sqrt{a^2-R^2}, \\ \tau_{xy} \Big|_{z=0} &= \tau_{yz} \Big|_{y=0} = \tau_{zx} \Big|_{y=0} = 0. \end{aligned} \right\} \quad (A-3)$$

AD-A127 529

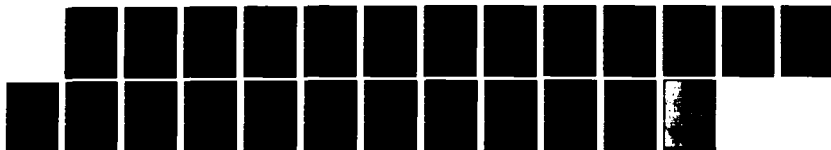
AN ANALYSIS OF CONICAL INDENTATION OF AN
ELASTIC/PERFECTLY PLASTIC HALF-S. (U) PENNSYLVANIA
STATE UNIV UNIVERSITY PARK APPLIED RESEARCH LAB.
T KATO 26 OCT 82 ARL/PSU/TM-82-238

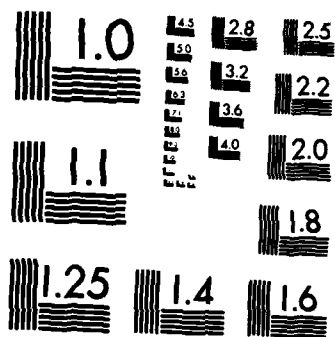
2/2

UNCLASSIFIED

F/G 28/11

NL





MICROCOPY RESOLUTION TEST CHART
NATIONAL BUREAU OF STANDARDS-1963-A

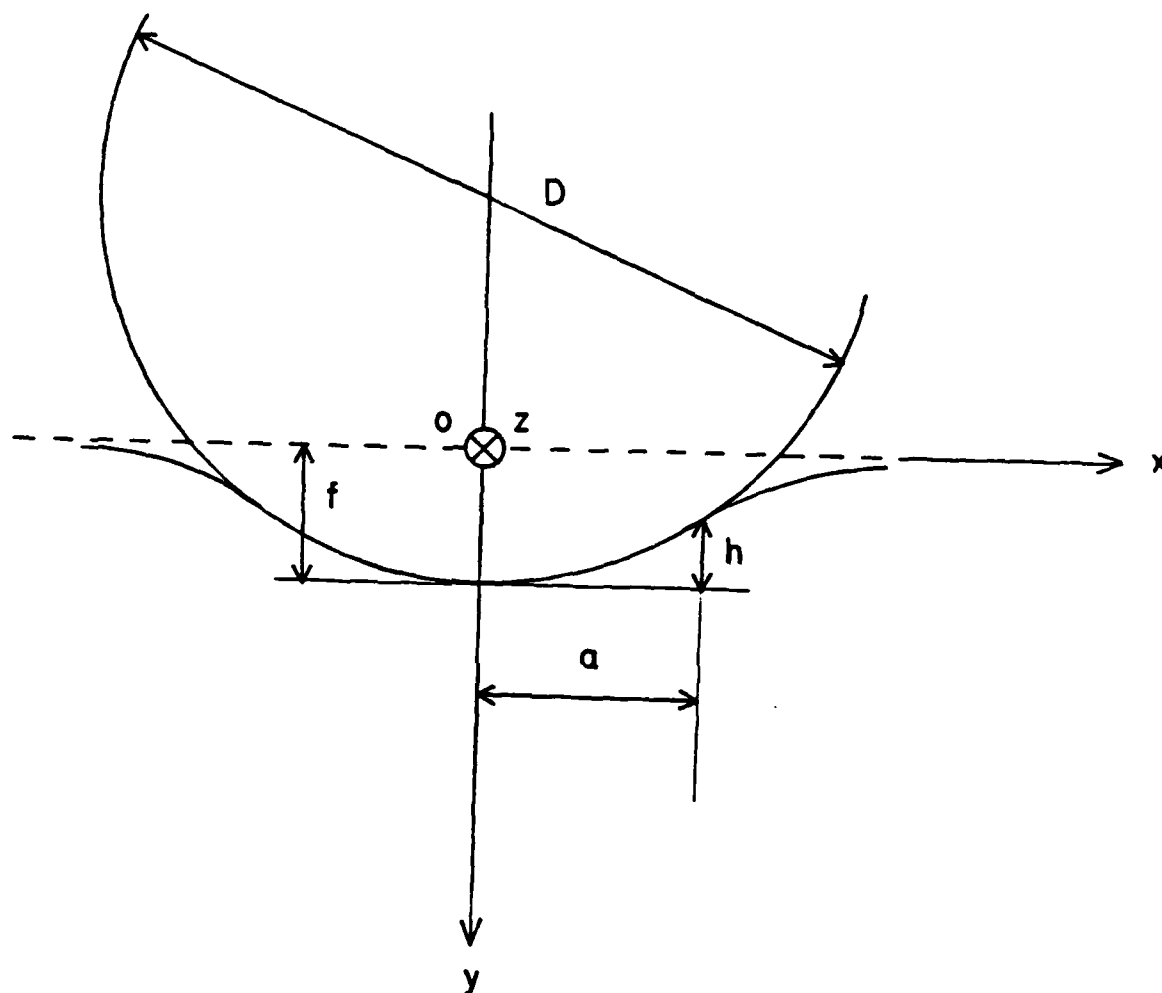


Figure 34. Spherical Indentation Geometry beneath the Indenter.

and

$$F = \frac{8Ea}{3D(1-\nu^2)}$$

$$f = \frac{2a^2}{D} = 2h.$$

3. Conical Indentation (Sneddon Solution)

The coordinate system for Sneddon's analysis is given in Figure 35. Before defining expressions for the stress distributions in the half-space, the displacement functions, mean pressure and pressure distribution at the surface of the half-space will be defined. The vertical displacement at the surface of the half-space is assumed as:

$$[v(\rho)]_{y=0} = d + e(1-\rho),$$

$$\text{where } \rho = x/b,$$

(A-6)

$$d = e(\frac{1}{2}\pi - 1),$$

while the horizontal displacement on the surface is given by:

$$[u(\rho)] = \left\{ \begin{array}{ll} \frac{1-2\nu}{4(1-\nu)} e\rho \left\{ \ln \frac{\rho}{1+\sqrt{1-\rho^2}} - \frac{1-\sqrt{1-\rho^2}}{\rho^2} \right\} & (\rho < 1) \\ -\frac{1-2\nu}{4(1-\nu)} \frac{e}{\rho} & (\rho > 1) \end{array} \right. \quad (A-7)$$

The resultant force F , the mean pressure p_m and the pressure distribution $p(\rho)$ on the surface are expressed as:

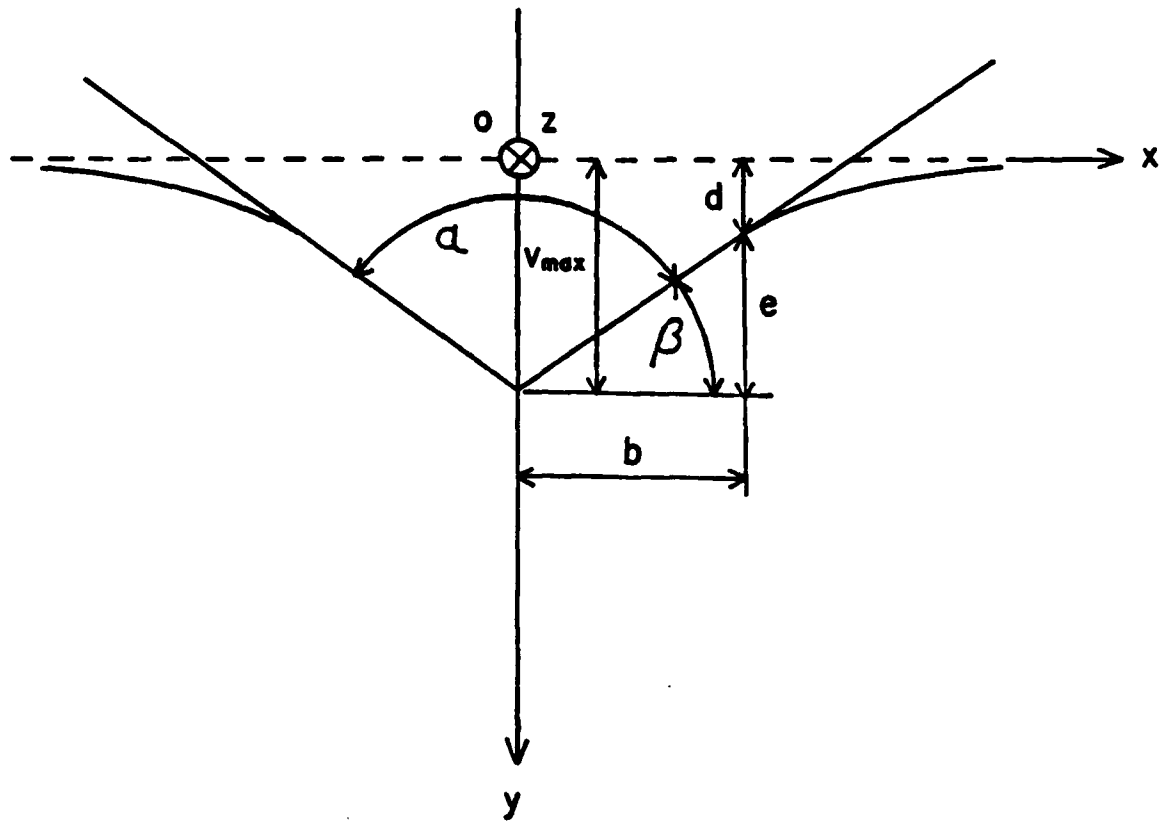


Figure 35. Conical Indentation Geometry beneath the Indenter.

$$F = \frac{\pi b e E}{2(1-\nu^2)} = \frac{E \pi b^2}{2(1-\nu^2)} \tan \delta ,$$

$$p_m = \frac{F}{\pi b^2} = \frac{E \tan \delta}{2(1-\nu^2)} , \quad (A-8)$$

$$p_{(\rho)} = p_m \operatorname{arcosh} \left(\frac{1}{\rho} \right) ,$$

The non-dimensionalized stresses within the half space are given by:

$$\frac{\sigma_x}{p_m} = - \left(K_1^0 - \frac{1-2\nu}{\rho} K_0^1 + \frac{\zeta}{\rho} K_1^1 - K_2^0 \right) ,$$

$$\frac{\sigma_y}{p_m} = - \left(K_1^0 + \zeta K_2^0 \right) ,$$

$$\frac{\sigma_z}{p_m} = - \left(2\nu K_1^0 + \frac{1-2\nu}{\rho} K_0^1 - \frac{\zeta}{\rho} K_1^1 \right) , \quad (A-9)$$

$$\frac{\tau_{xy}}{p_m} = - \zeta K_2^1 ,$$

$$\tau_{yz} = \tau_{zx} = 0 ,$$

but when $x = 0$ ($\rho = 0$):

$$\frac{\sigma_x}{p_m} = \frac{\sigma_z}{p_m} = - (1 + \nu) K_1^0 - \frac{\sigma_y}{2p_m} ,$$

where

$$K_1^0 = \frac{1}{2} \ln \frac{Q^2 + 2Qt \cos(\bar{\psi} - \bar{\phi}) + t^2}{(\zeta + \sqrt{\rho^2 + \zeta^2})^2} ,$$

$$K_2^0 = \frac{1}{\sqrt{\rho^2 + \zeta^2}} - \frac{\cos \bar{\phi}}{Q}$$

$$K_1^1 = \frac{1}{\rho} [\sqrt{\rho^2 + \zeta^2} - Q \cos \bar{\phi}],$$

$$K_2^1 = \frac{1}{\rho} \left[\frac{t}{Q} \cos(\bar{\psi} - \bar{\phi}) - \frac{\zeta}{\sqrt{\rho^2 + \zeta^2}} \right] ,$$

$$K_0^1 = \frac{1}{2} [\rho K_1^0 - \zeta K_1^1 - \frac{1}{\rho} (1 - Q \sin \bar{\phi})] ,$$

and

$$\zeta = \frac{y}{b} , \quad \rho = \frac{x}{b} , \quad e = b \tan \beta ,$$

$$t^2 = H \zeta^2 , \quad Q^4 = (\rho^2 + \zeta^2 - 1)^2 + 4 \zeta^2 ,$$

$$\bar{\psi} = \arctan \left(\frac{1}{\zeta} \right) , \quad \bar{\phi} = \frac{1}{2} \arctan \left\{ \frac{2\zeta}{(\rho^2 + \zeta^2 - 1)} \right\} .$$

4. Comparison of the three elastic indentation stress fields.

To compare the three elastic stress fields which are given in the preceding sections of APPENDIX A for the same condition, Young's modulus E , Poisson's ratio ν , and the resultant force F must be fixed. For the finite element analysis of conical indentation, the following four values were defined:

$$E = 49000 \text{ N/mm}^2$$

$$\nu = 0.22$$

$$\text{Contact radius } b = 0.3 \text{ mm}$$

$$\text{cone angle } \alpha = 136^\circ (\beta = 22^\circ)$$

From these four values the resultant force F can be obtained from equation (A-8):

$$F = \frac{E\pi b^2}{2(1-\nu^2)} \tan\beta = 2941. \text{ (N)} .$$

If we equate the contact radius a for Huber's with b for Sneddon's then the spherical diameter of Huber solution can be defined as:

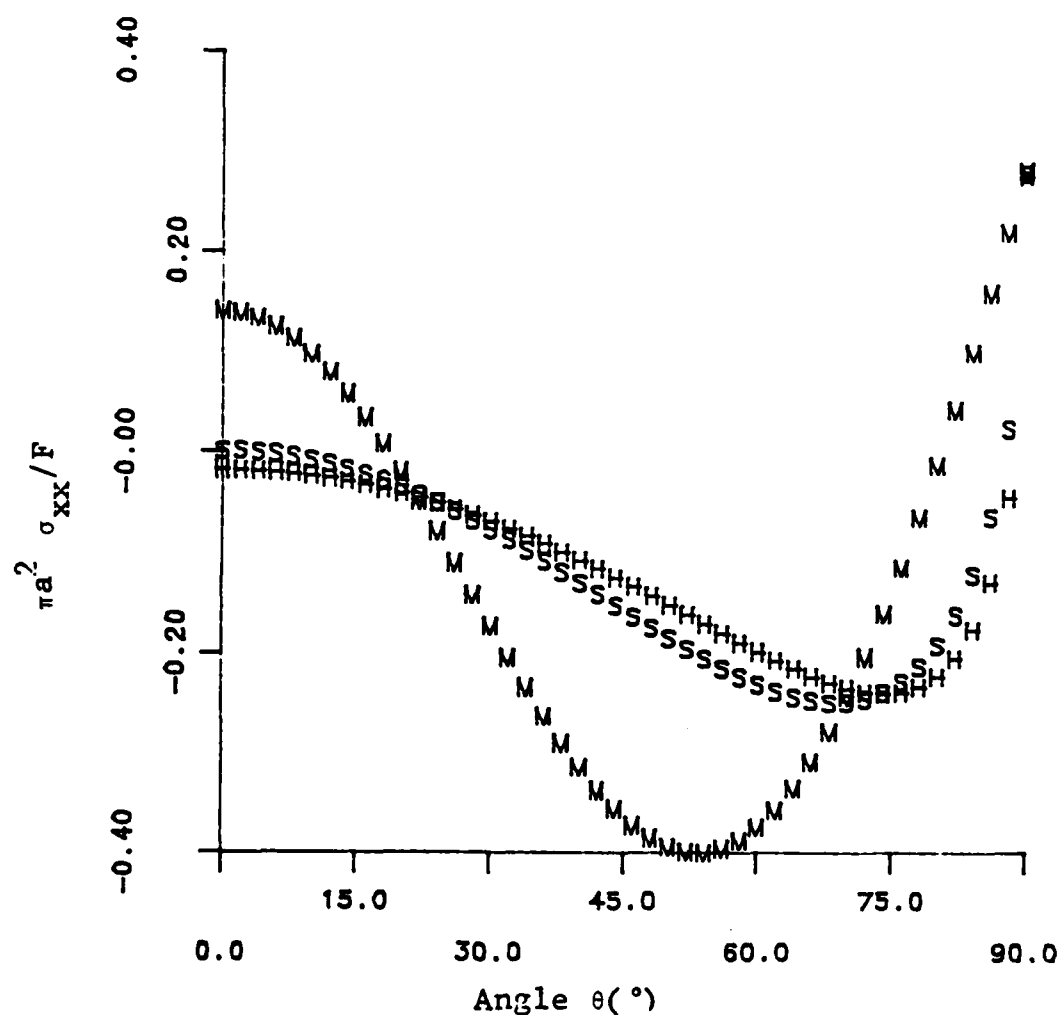
$$D = \frac{8Ea}{3F(1-\nu^2)} = 14.00 \text{ (mm)} .$$

Huber's stress fields and Sneddon's stress fields were non-dimensionalized by the factor $\pi a^2/F = \pi b^2/F$; however, Michell's stress field was non-dimensionalized by the factor $\pi r^2/F$ (r is variable). To compare Michell's stress field with other two stress fields results for the Michell solution (A-1) are multiplied by $p' = F/\pi r^2$ and divided by $p_p = p_m = F/\pi a^2 = F/\pi b^2$. The comparison of the three elastic non-dimensionalized stress fields in terms of the angle θ are plotted in Figures 36 through 39 for the coordinates:

$$x^2 + y^2 = a^2 = r^2 \quad \text{and} \quad z = 0,$$

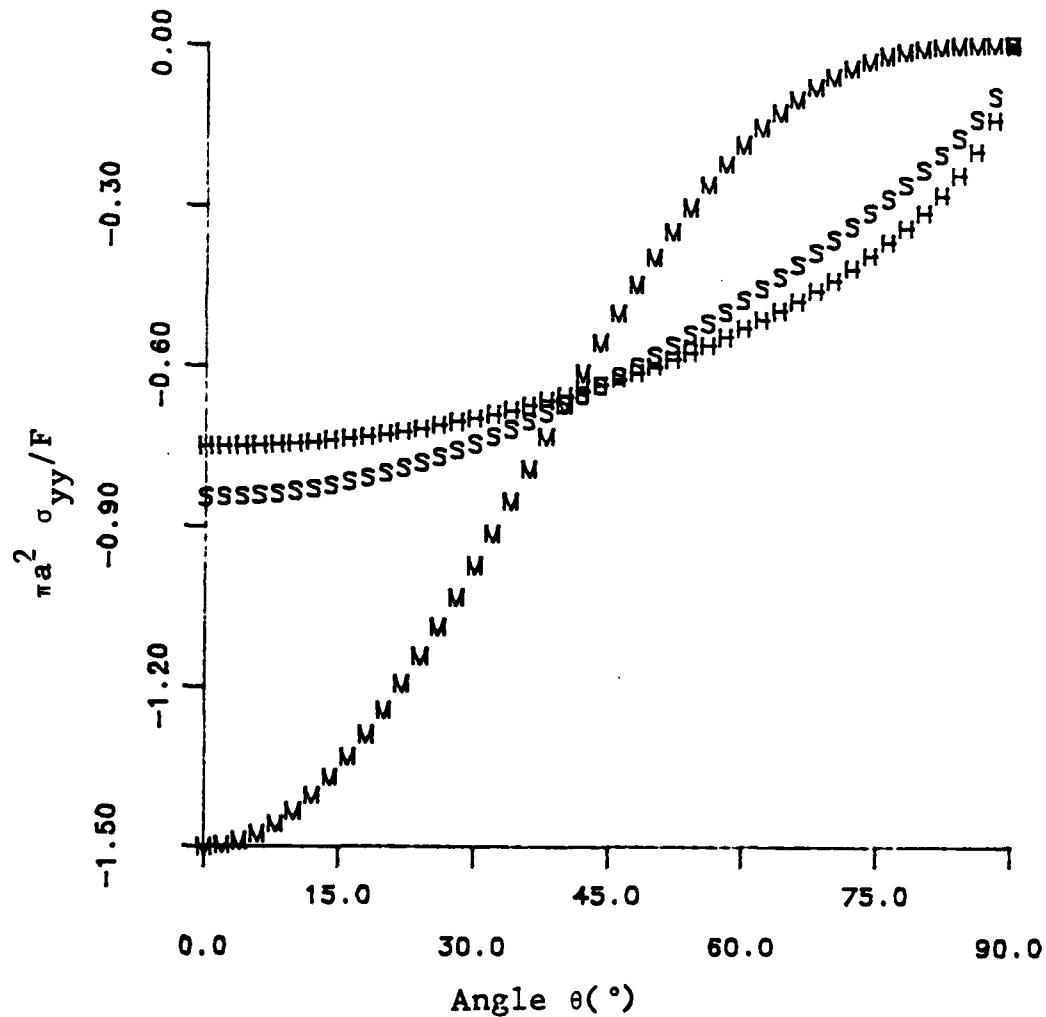
where $x = r\sin\theta$, $y = r\cos\theta$.

To see the effect of the cone angle α in Sneddon solution, the cone angle α and the contact radius b are assumed as variables while E , ν , F , a and D are remained as constants. The relationship between α, β , b are shown in Table 3. With the constant non-dimensionalized factor $1/p_0$, the change of Sneddon's stress field in terms of the angle θ are plotted in Figures 40 through 43 under the condition:



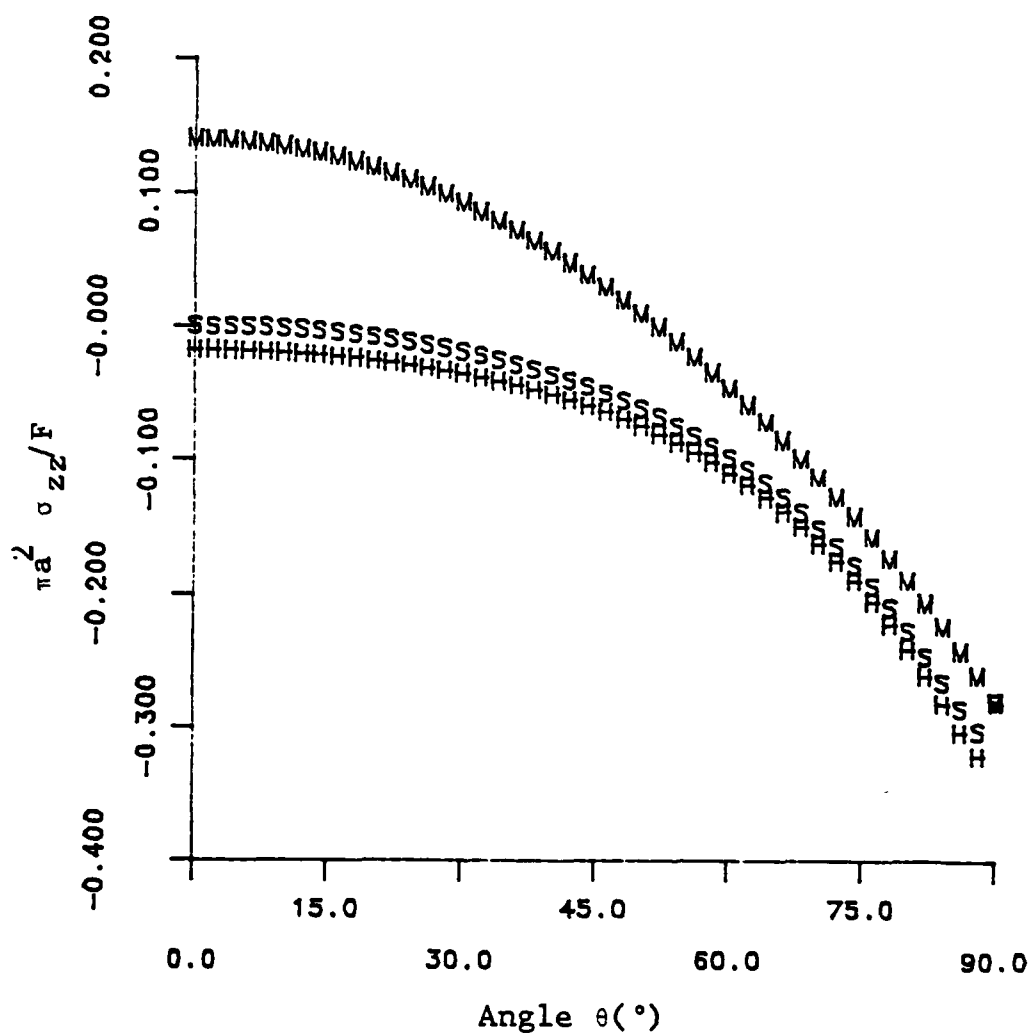
M : Michell Solution (Point Indentation)
H : Huber Solution (Spherical Indentation)
S : Sneddon Solution (Conical Indentation)

Figure 36. Comparison of Elastic Point, Spherical and Conical Indentation Stress Fields (I): Non-dimensionalized Stress, σ_{xx} .



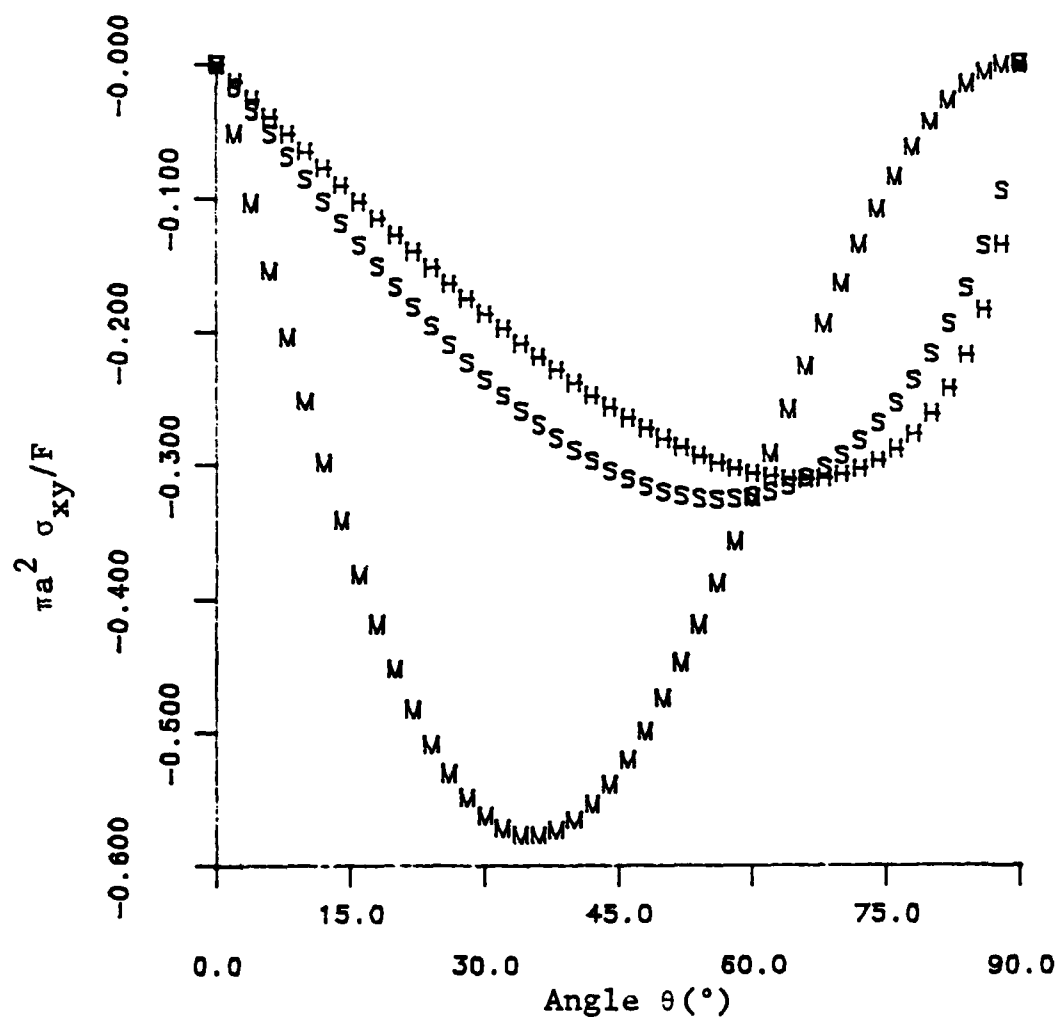
M : Michell Solution (Point Indentation)
 H : Huber Solution (Spherical Indentation)
 S : Sneddon Solution (Conical Indentation)

Figure 37. Comparison of Elastic Point, Spherical
 and Conical Indentation Stress Fields (II):
 Non-dimensionalized Stress, σ_{yy} .



M : Michell Solution (Point Indentation)
H : Huber Solution (Spherical Indentation)
S : Sneddon Solution (Conical Indentation)

Figure 38. Comparison of Elastic Point, Spherical and Conical Indentation Stress Fields (III): Non-dimensionalized Stress, σ_{zz} .

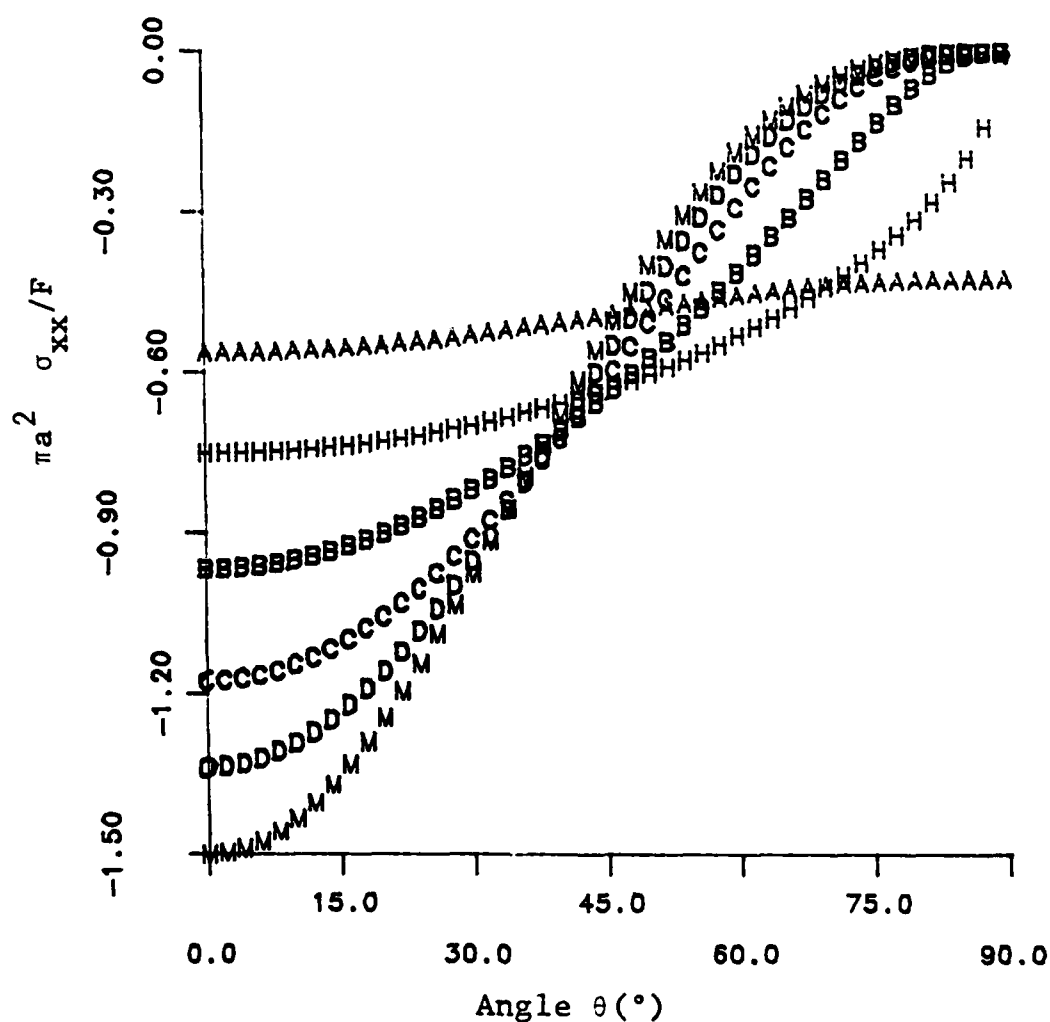


M : Michell Solution (Point Indentation)

H : Huber Solution (Spherical Indentation)

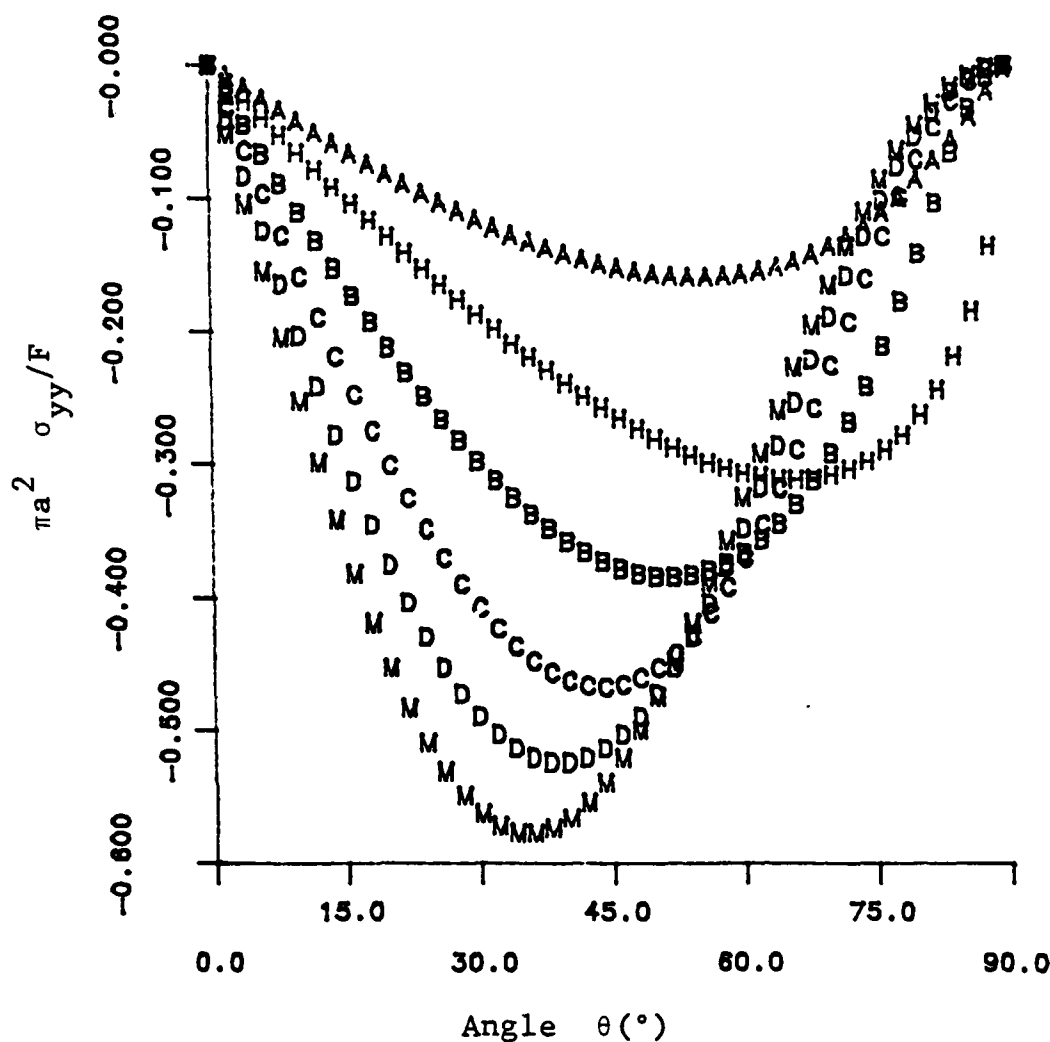
S : Sneddon Solution (Conical Indentation)

Figure 39. Comparison of Elastic Point, Spherical and Conical Indentation Stress Fields (IV): Non-dimensionalized Stress, σ_{xy} .



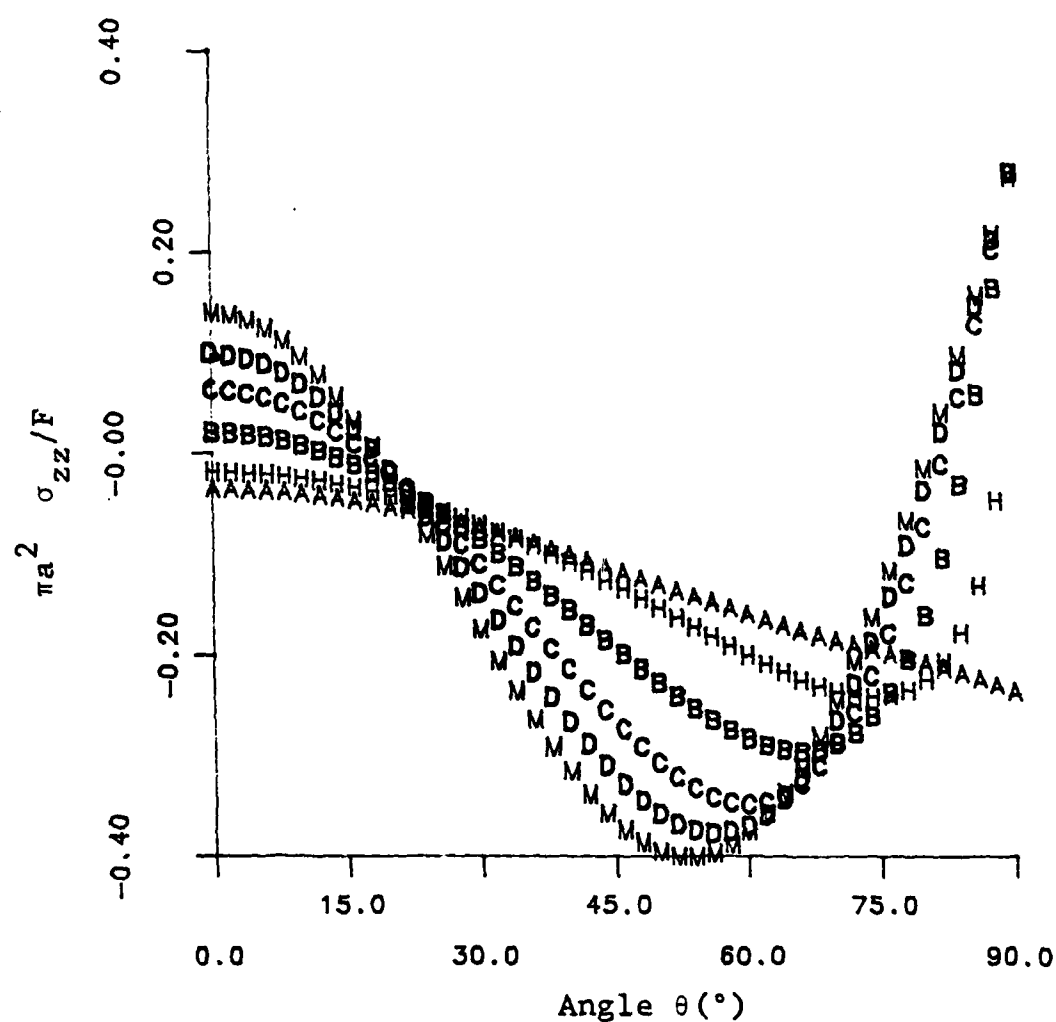
- A: Sneddon Solution (Conical Indentation): $\alpha = 160^\circ$
 B: Sneddon Solution (Conical Indentation): $\alpha = 120^\circ$
 C: Sneddon Solution (Conical Indentation): $\alpha = 80^\circ$
 D: Sneddon Solution (Conical Indentation): $\alpha = 40^\circ$
 H: Huber Solution (Spherical Indentation)
 M: Michell Solution (Point Indentation)

Figure 40. Included Angle Effect of Conical Indentation (I): Non-dimensionalized Stress, σ_{xx} .



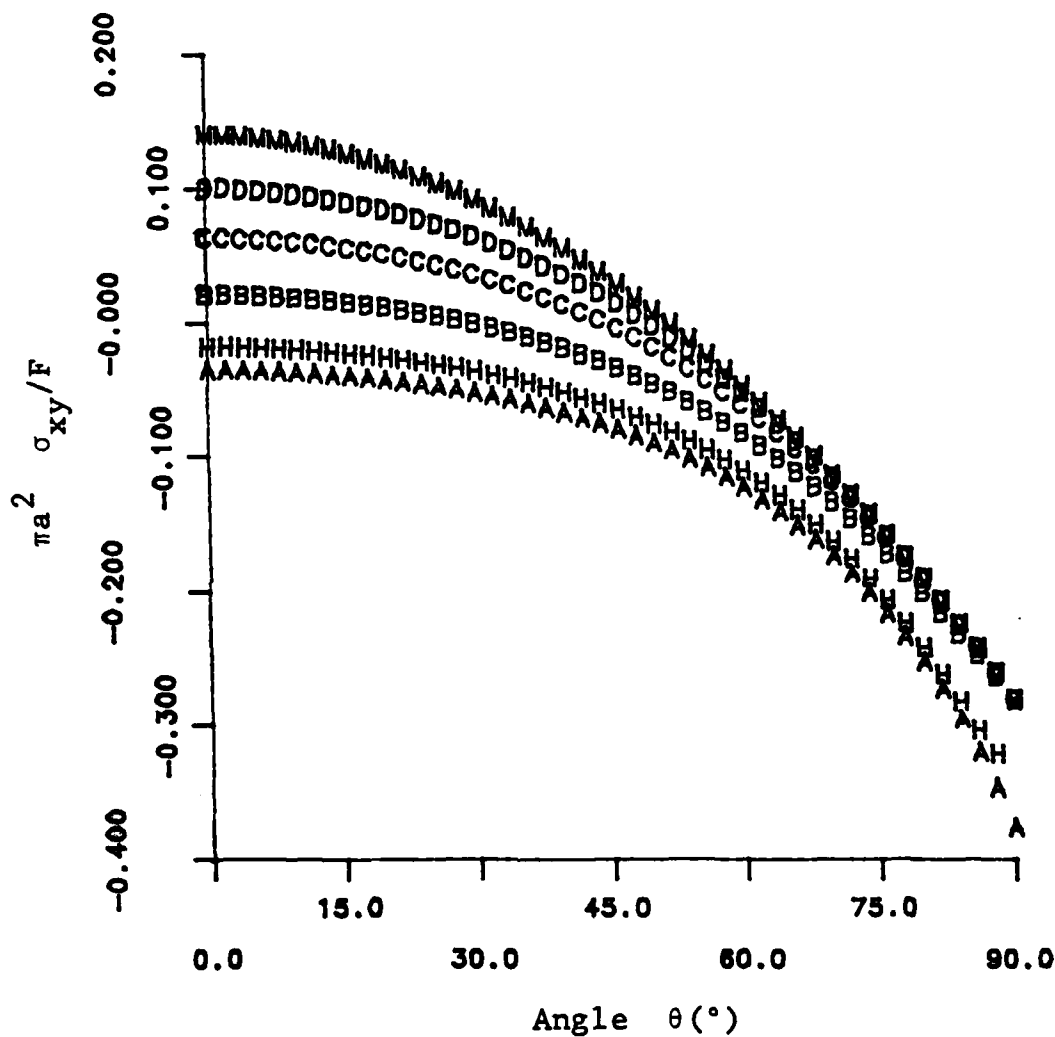
- A: Sneddon Solution (Conical Indentation): $\alpha = 160^\circ$
 B: Sneddon Solution (Conical Indentation): $\alpha = 120^\circ$
 C: Sneddon Solution (Conical Indentation): $\alpha = 80^\circ$
 D: Sneddon Solution (Conical Indentation): $\alpha = 40^\circ$
 H: Huber Solution (Spherical Indentation)
 M: Michell Solution (Point Indentation)

Figure 41. Included Angle Effect of Conical Indentation (II): Non-dimensionalized Stress, σ_{yy} .



- A: Sneddon Solution (Conical Indentation): $\alpha = 160^\circ$
 B: Sneddon Solution (Conical Indentation): $\alpha = 120^\circ$
 C: Sneddon Solution (Conical Indentation): $\alpha = 80^\circ$
 D: Sneddon Solution (Conical Indentation): $\alpha = 40^\circ$
 H: Huber Solution (Spherical Indentation)
 M: Michell Solution (Point Indentation)

Figure 42. Included Angle Effect of Conical Indentation (III): Non-dimensionalized Stress, σ_{zz} .



- A: Sneddon Solution (Conical Indentation): $\alpha = 160^\circ$
 B: Sneddon Solution (Conical Indentation): $\alpha = 120^\circ$
 C: Sneddon Solution (Conical Indentation): $\alpha = 80^\circ$
 D: Sneddon Solution (Conical Indentation): $\alpha = 40^\circ$
 H: Huber Solution (Spherical Indentation)
 M: Michell Solution (Point Indentation):

Figure 43. Included Angle Effect of Conical Indentation (IV): Non-dimensional Stress, σ_{xy} .

Table 3. Relationship between α , β , and b

$\alpha(^{\circ})$	$\beta(^{\circ})$	$b_{(\text{mm})}$	b/a
160	10	0.4541	1.514
136	22	0.3	1.0
120	30	0.2510	0.8365
80	50	0.1747	0.5823
40	70	0.1150	0.3835

$$x^2 + y^2 = a^2 = 0.09$$

By comparing these figures with Figures 36 to 39, it is obvious that Sneddon's stress field behaves like Hertzian stress field under the same contact radius and also Sneddon's stress field behaves like Michell's stress field under the sharp included angle and small contact radius as be expected.

APPENDIX B

THE ANALYTICAL-EXPERIMENTAL EQUATIONS FOR ELASTIC/PLASTIC INDENTATION

Various formulas to define the indentation hardness, H , in terms of Young's modulus, E , Poisson's ratio, ν , and yield strength, Y , have been developed by Johnson [11], Perrott [37,39], and Izumitani [12]. These formulas were derived by utilizing Hill's elastic-plastic solution of the expansion of a spherical or cylindrical cavity [7,8] along with experimental observations.

Johnson's formula for a conical indentation is:

$$\frac{H}{Y} = \frac{2}{3} + 2 \ln \left(\frac{c}{b} \right) , \quad (B-1)$$

with

$$\frac{E}{Y} \tan \beta = 6(1-\nu) \left(\frac{c}{b} \right)^3 - 4(1-2\nu) , \quad (B-2)$$

and for a wedge indentation is:

$$\frac{H}{Y} = \frac{2}{\sqrt{3}} \left[\frac{1}{2} + \ln \left(\frac{c}{b} \right) \right] , \quad (B-3)$$

with

$$\frac{4E}{\pi Y} \tan \beta = (5-4\nu) \left(\frac{c}{b} \right)^2 - 3(1-2\nu) , \quad (B-4)$$

where c is the radius of the plastic zone and the center is the undeformed origin.

Perrott's formula for conical and pyramidal indentation is:

$$\frac{H}{Y} = 0.494 + 0.577 \ln \left(\frac{E \tan \beta}{Y(1-\nu^2)} \right) . \quad (B-5)$$

Izumitani's formula for knoop indentation is:

$$\frac{H}{Y} = \frac{2}{3} + 2 \ln \left(\frac{c}{b} \right), \quad (B-6)$$

with

$$\left(\frac{c}{b} \right)^3 = \frac{E}{3(1-\nu)Y}, \quad (B-7)$$

which are the same as Hill's equations for the expansion of a spherical cavity in an infinite medium.

The relationship between indentation depth v_{\max} and residual crater depth v_{\max}^R in terms of material properties and geometrical properties for the conical indentation problem is expressed by Lawn and Howes [46] as:

$$\left(\frac{v_{\max}^R}{v_{\max}} \right)^2 = 1 - \left[2(1-\nu^2) \left(\frac{\gamma_E}{\gamma_H} \right)^2 \cot \beta \right] \frac{H}{E}, \quad (B-8)$$

where H is the indentation hardness, and J_E is the elastic geometrical parameter which is expressed as:

$$\gamma_E = \frac{v_{\max}}{b \tan \beta} \left(= \frac{1}{2} \pi \text{ for Sneddon's solution} \right), \quad (B-9)$$

and J_H is actually an unknown geometrical parameter of plastic hysteresis; however, it is usually defined as $\gamma_H \approx \gamma_E$.

BIBLIOGRAPHY

1. Boussinesq, J., "Application des Potentials a l'Etude de l'Equilibre et du Mouvement des Solides Elastiques," Gauthier-Villars, Paris, (1885).
2. Michell, J.H., "Elementary Distributions of Plane Stress," Proceedings of the London Mathematical Society, Vol. 32, (1900), pp. 35-61.
3. Hertz, H., Hertz's Miscellaneous Papers, translated by D.E. Jones and G.A. Schott, Macmillan, New York, (1896), pp. 146-162, 163-183.
4. Huber, M.T., "Zur Theorie der Beriihrun fester elastischer Körper," Annalen Der Physik, Ser 4, 14, (1904), pp. 153-163.
5. Sneddon, I.N., "Boussinesq Problem for a Rigid Cone," Cambridge Philosophical Society, proceeding, Vol. 44, (1948), pp. 492-507.
6. Sneddon, I.N., Fourier Transforms, McGraw-Hill, (1951), pp. 462-468.
7. Hill, R., The Mathematical Theory of Plasticity, Clarendon Press, Oxford, (1950), Chapter 5.
8. Hill, R., "General Feature of Plastic-Elastic Problems as Exemplified by Some Particular Solutions," Journal of Applied Mechanics, Vol. 16, (1949), pp. 295-300.
9. Hamilton, G.M. and Goodman, L.E., "The Stress Field Created by a Circular Sliding Contact," Journal of Applied Mechanics, Vol. 33, (1966), pp. 371-376.
10. Johnson, K.L., "An Experimental Determination of the Contact Stresses between Plastically Deformed Cylinders and Spheres," Engineering Plasticity, University Press, Cambridge, (1968), pp. 341-361.
11. Johnson, K.L., "The Correlation of Indentation Experiments," Journal of the Mechanics and Physics of Solids, Vol. 18, (1970), pp. 115-126.
12. Izumitani, T. and Suzuki, I., "Indentation Hardness and Lapping Hardness of Optical Glass," Glass Technology, Vol. 14, No. 2, (April 1973), pp. 35-41.
13. Parrons, B. and Wilson, E.A., "A Method of Determining the Surface Contact Stress Resulting from Interference Fits," Journal of Engineering for Industry, Transaction, ASME, (February 1970), pp. 208-218.

14. Hardy, C., Baronet, C.N. and Tordion, G.W., "The Elastic-Plastic Indentation of a Half-Space by a Rigid Sphere," International Journal for Numerical Method in Engineering, Vol. 3 (1977), pp. 451-462.
15. Imaoka, M. and Yasui, I., "Finite Element Analysis of Indentation on Glass," Journal of Non-Crystalline Solids, Vol. 22, (1976), pp. 315-329.
16. Mises, R. Von, "Mechanik der festen Körper im plastischen deformablem Zustand," Goettinger Nachrichten. Mathematische-Physikalisch Klasse, (1913), pp. 582-592.
17. Johnson W. and Mellor, P.B., "Engineering Plasticity," Van Nostrand Reinhold, (1978).
18. Marcal, P.V. and King, I.P., "Elastic-Plastic Analysis of Two-dimensional Stress System by the Finite Element Method," International Journal of Mechanical Science, Vol. 9, (1967), pp. 143-155.
19. Yamada, Y., Yoshimura, N. and Sakurai, T., "Plastic Stress-Strain Matrix and Its Application for the Solution of Elastic-Plastic Problems by the Finite Element Method," Report of the Institute of Industrial Science, Aug. 1967, University of Tokyo, Tokyo, Japan.
20. Yamada, Y., Kawai, T., Yoshimura, N. and Sakurai, T., "Analysis of the Elastic-Plastic Problems by the Matrix Displacement Method," Proceeding of 2nd Conference on Matrix Methods of Structural Mechanics, Wright-Patterson Air Force Base, Ohio, (1968), pp. 1271-1299.
21. Zienkiewicz, O.C., The Finite Element Method, Third Edition McGraw-Hill, (1977).
22. Desai, C.S. and Abel, J.F., Introduction to the Finite Element Method. A Numerical Method for Engineering Analysis, Van Nostrand Reinhold Company, (1972).
23. Vos, R.G., "Note on Residual Force Method," Comment on a paper by G.C. Nayak and O.C. Zienkiewicz, International Journal for Numerical Methods in Engineering, Vol. 6, No. 3.
24. Vos, R.G., "Finite Element Solution of Nonlinear Structure by Perturbation Technique," First International Conference on Numerical Methods in Nonlinear Mechanics, University of Texas at Austin, Texas, September 1974.

25. Prayer, W., "The Theory of Plasticity: A Survey of Recent Achievements," Proceeding of the Institution for Mechanical Engineering, Vol. 169, (1955), pp. 41-57.
26. Hodge, P.G., "Piecewise Linear Plasticity," Proceeding of the 9th International Congress of Applied Mechanics, Vol. 8, University de Bruxelles, (1956), pp. 65-72.
27. Vos, R.G. and Armstrong, W.H., "Improved Hardening Theory for Cyclic Plasticity," Technical Note in AIAA Journal, March 1973.
28. Vos, R.G., "Development of Solution Technique for Nonlinear Structural Analysis," Boeing Report to NASA MSFC, Contract NAS 8-29625, Document D 180-18325, September 1974.
29. Knott, J.F., Fundamentals of Fracture Mechanics, Butterworth and Co., London, (1977).
30. Lawn, B.R. and Wilshaw, T.R., Fracture of Brittle Solids, Cambridge University Press, (1975).
31. Lawn, B.R., Wilshaw, T.R. and Hatley, N.E.W., "A Computer Simulation Study of Hertzian Cone Crack Growth," International Journal of Fracture, Vol. 10, No. 1, (1974), pp. 1-16.
32. Lawn, B.R. and Swain, M.V., "Microfracture Beneath Point Indentations in Brittle Solids," Journal of Material Science, Vol. 10, (1975), pp. 113-122.
33. Lawn, B.R. and Wilshaw, T.R., "Review Indentation Fracture: Principles and Applications," Journal of Material Science, Vol. 10, (1975), pp. 1049-1081.
34. Lawn, B.R. and Fuller, E.R., "Equilibrium Penny-like Cracks in Indentation Fracture," Journal of Material Science, Vol. 10, (1975), pp. 2016-2024.
35. Swain, M.V. and Hagan, J.T., "Indentation Plasticity and the Ensuing Fracture of Glass," Journal of Physics D. Applied Physics, Vol. 9, (1976), pp. 2201-2214.
36. Lawn, B.R. and Evans, A.G., "A Model of Crack Initiation in Elastic/Plastic Indentation Fields," Journal of Material Science, Vol. 12 (1977), pp. 2195-2199.
37. Perrott, C.M., "Elastic-Plastic Indentation: Hardness and Fracture," Wear, Vol. 45, (1977), pp. 293-309.

38. Hagan, J.T. and Swain, M.V., "The Origin of Median and Lateral Cracks around Plastic Indents in Brittle Materials," Journal of Physics D. Applied Physics, Vol. 11, (1978), pp. 2091-2102.
39. Perrott, C.M., "On the Indentation Fracture of Cemented Carbide II - The Nature of Surface Fracture Toughness," Wear, Vol. 47, (1978), pp. 81-91.
40. Conrad, H., Keshavan, M.K. and Sargent, G.A., "Hertzian Fracture of Pyrex Glass under Quasi-Static Loading Conditions," Journal of Material Science, Vol. 14, (1979), pp. 1473-1494.
41. Marshall, D.B. and Lawn, B.R., "Residual Stress Effects in Sharp Contact Cracking, Part 1 Indentation Fracture Mechanics," Journal of Material Science, Vol. 14, (1979), pp. 2001-2012.
42. Marshall, D.B., Lawn, B.R. and Chantikul, P., "Residual Stress Effects in Sharp Contact Cracking, Part 2 Strength Degradation," Journal of Material Science, Vol. 14, (1979), pp. 2225-2235.
43. Hagan, J.T., "Micromechanics of Crack Nucleation during Indentations," Journal of Material Science, Vol. 14, (1979), pp. 2975-2980.
44. Hagan, J.T., "Shear Deformation under Pyramidal Indentation in Soda-Lime Glass," Journal of Material Science, Vol. 15, (1980), pp. 1417-1424.
45. Conway, J.C. and Kirchner, H.P., "The Mechanics of Crack Initiation and Propagation beneath a Moving Sharp Indenter," Journal of Material Science, Vol. 15, (1980), pp. 2879-2883.
46. Lawn, B.R. and Howes, V.R., "Elastic Recovery at Hardness Indentations," Journal of Material Science, Vol. 16 (1981), pp. 2745-2752.
47. Chiang, S.S., Marshall, D.B. and Evans, A.G., "The Response of Solids to Elastic/Plastic Indentation. I. Stresses and Residual Stresses, II. Fracture Initiation," Journal of Applied Physics, 53 (1), January 1982, pp. 298-317.

DISTRIBUTION LIST FOR TM 82-230

Commander (NSEA 0342)
Naval Sea Systems Command
Department of the Navy
Washington, DC 20362

Copies 1 and 2

Commander (NSEA 9961)
Naval Sea Systems Command
Department of the Navy
Washington, DC 20362

Copies 3 and 4

Defense Technical Information Center
5010 Duke Street
Cameron Station
Alexandria, VA 22314

Copies 5 through 10

END

FILMED

6-83

DTIC